NUCLEAR REACTION AND STRUCTURE EFFECTS NEAR AND BEYOND THE β-STABILITY LINE

Submitted to the

FACULTY OF SCIENCE

THAPAR UNIVERSITY, PATIALA

for the degree of

DOCTOR OF PHILOSOPHY

by

MAHESH KUMAR

SCHOOL OF PHYSICS AND MATERIALS SCIENCE

THAPAR UNIVERSITY

PATIALA-147004, INDIA

JANUARY, 2016

Dedicated to

My Mother

who had been my strongest support and there blessing are always with me

CERTIFICATE

This is to certify that the thesis entitled "**NUCLEAR REACTION AND STRUCTURE EFFECTS NEAR AND BEYOND THE β-STABILITY LINE**" being submitted by **Mr. Mahesh Kumar** for the fulfillment of the requirements for the award of Degree of Doctor of Philosophy in the School of Physics and Materials Science, Thapar University, Patiala, is a record of the candidate's own work carried out by him under my supervision. The matter presented in this thesis has not been submitted in part or full for the award of any degree in any university or institute.

Supervisor

MSharma.

Dr. Manoj K. Sharma

Professor and Head

School of Physics and Materials Science

Thapar University, Patiala- 147004

Punjab (India)

Thapar University, Patiala

CANDIDATE'S DECLARATION

I hereby certify that the thesis entitled "**NUCLEAR REACTION AND STRUCTURE EFFECTS NEAR AND BEYOND THE β-STABILITY LINE**" being submitted for the partial fulfillment of the requirements for the award of Degree of Doctor of Philosophy in the School of Physics and Materials Science, Thapar University, Patiala, is a record of my own work carried out under the supervision of **Dr. Manoj K. Sharma**. The matter presented in this thesis has not been submitted in part or full for the award of any degree in any university or institute.

This is to certify that the above statement made by the candidate is correct to the best of our knowledge.

Supervisor
(Dr. Manoj K. Sharma)

Head of Department
(Dr. Manoj K. Sharma)

Dean R and SP
(Dr. O. P. Pandey)

External Examiner
(Dr. P. K. Raina)

DATED: 20/5/16

Acknowledgements

I acknowledge with a sense of deep and sincere gratitude, the meticulous guidance, ingenious discussions and steady encouragement rendered by **Dr. Manoj K. Sharma**, Professor and Head, School of Physics and Materials Science, Thapar University, Patiala and **Dr. S. K. Patra**, Professor, Institute of Physics, Bhubneswar. I owe the greatest debt of gratitude to them for suggesting the research problem followed by ever willing help and the freedom extended to me throughout the period of my research. I greatly appreciate their support and guidance not only in research but also in my day to day life. A special and sincere thank to **Dr. S. K. Patra** for the almighty for giving me the courage and strength for completing this task successfully. I greatly appreciate his knowledge and willingness to assist me during my research work without any personal credit. Working under his guidance, I have earned a great deal of scientific knowledge which has shaped my research skills and encouraged me to pursue in research field. This document would not exist without his guidance and patience.

I take this opportunity to thank **Prof. Prakash Gopalan** , Director Thapar University, Patiala for providing me university's resources and facilities necessary to carry out this research work.

I am deeply thankful to **Dr. O. P Pandey**, Dean, Research and Sponsored Projects and **Dr. S. S Bhatia**, Dean Academic Affairs, Thapar University, Patiala, for their support and needful help during the various stages of my research work. I also take this opportunity to express my sincere thanks to all the faculty members specially the faculty members of my doctoral committee (**Dr. Manoj K. Sharma, Dr. S. S. Bhatia, Dr. Suneel Kumar and Dr. S. Jana**) for their valuable suggestions in regards to complete this task and the staff of School of Physics and Materials Science, Thapar University, Patiala for providing me constant encouragement.

I am also grateful to my friends Dr. R. N. Panda, Dr. Raj Kumar, Dr. Bidhubhushan Sahu, Dr. Shailesh K. Singh, Dr. M. Bhuyan, Dr. Gudveen, Dr. Kiran Sandhu, Dr. Deepika Jain, Ms. Rajni and Mr. Subrat Biswal for providing me the constant help, moral support and encouraging environment to take the challenges.

I concedes my heartiest admiration and gratitude for my parents (Mr. Ramesh Sharma and Late Mrs. Kanta Sharma) for the moral support and countless blessings. I am thankful to my brothers Mr. Dinesh Sharma and Mr. Jogesh Sharma for their best wishes, support and love. Gratitude and regard is also recorded for the support offered by Sister-in law, 'Mrs. Deepika Sharma'.

Lastly the most important, my strongest support, I feel immense obligation, admiration and gratitude for my wife, Mrs. Ankusha Sharma and my loving son, Ranish Sharma, who always stood by me during the critical phases of life and encouraged me to reach this destination of knowledge. Both of them are most indispensable source of strength for me. Thank for everything.

Patiala

December, 2015.

(Mahesh Kumar)

List of Publications

I. International Journals:

1. **Mahesh K. Sharma**, R. N. Panda, Manoj K. Shrama and S. K. Patra, "Search of ^{37}Mg halo structure using Glauber model and microscopic relativistic mean field densities", Phys. Rev. C **93**, 014322 (2016).

2. **Mahesh K. Sharma**, R. N. Panda, Manoj K. Shrama and S. K. Patra, "Reaction dynamics of $^{34-38}$Mg projectile with carbon target using Glauber model", AIP Conf. Proc. **1675**, 030093-1030093-4 (2015).

3. **Mahesh K. Sharma**, R. N. Panda, Manoj K. Shrama and S. K. Patra, "Nuclear structure study of some bubble nuclei in light mass region using mean field formalism", Chinese Physics C **39**, 064102 (2015).

4. **Mahesh K. Sharma**, R. N. Panda, Manoj K. Shrama and S. K. Patra, "Study of reaction of light mass nuclei using Glauber formalisms", Brazilian journal of physics **45**, 138-146 (2015).

5. R. N. Panda, **Mahesh K. Sharma** and S. K. Patra, "Nuclear structure and reaction properties of Ne, Mg and Si isotopes with RMF densities", Mod. Phys. Lett. A **29**, 1450013 (2014).

6. **Mahesh K. Sharma**, Manoj K. Sharma and S. K. Patra, "Reaction dynamics of halo nuclei using Glauber model", AIP Conf. Proc. **1524**, 186-189 (2013).

7. **Mahesh K. Sharma** and S. K. Patra, "Nuclear reaction cross sections from a simple effective density using a Glauber model", Phys. Rev. C **87** 044606 (2013).

8. **Mahesh K. Sharma**, M. S. Mehta, and S. K. Patra, "Nuclear reaction cross section for drip line nuclei in the framework of Glauber model using relativistic and non-relativistic densities", Int. J. Mod. Phys. E **22**, 1350005 (2013).

9. Manpreet Kaur, **Mahesh K. Sharma** and Manoj. K. Sharma, "Analysis of fragment distribution and associated effects in ^{12,13}C induced reactions" , Int. J. Mod. Phys. E **23**, 1450030 (2014). (Not a part of thesis)

II. In Conferences, Symposiums and Workshops:

1. **Mahesh K. Sharma**, R. N. Panda, Manoj K. Sharma and S. K. Patra "Reaction dynamics of $^{34-38}$Mg projectile with carbon target using Glauber model" , National Conference AMRP-2015, Sant Longowal Institute of Engineering and technology, Longowal.

2. **Mahesh K. Sharma**, R. N. Panda, Manoj K. Sharma and S. K. Patra "Reaction dynamics of $^{90-136}$Zr projectile with carbon target using Glauber model" , National Symposium Snp-2014, Banaras Hindu Universiy, Varanasi.

3. **Mahesh K. Sharma**, R. N. Panda, Manoj K. Sharma and S. K. Patra "Nuclear structure of some bubble nuclei using relativistic and non-relativistic mean field formalism" , National Conference EHST-2014, Shri Guru Granth Sahib World University, Fatehgarh Sahib.

4. **Mahesh K. Sharma**, R. N. Panda, Manoj K. Sharma and S. K. Patra "Structural properties and reaction dynamics of some of the light highly neutron-rich Si, S and Ar isotopes" , International Symposium Snp-2013, BARC, Mumbai.

5. **Mahesh K. Sharma**, Manoj K. Sharma and S. K. Patra "Reaction dynamics for some halo nuclear systems using Glauber model with relativistic mean field densities" , International Symposium Snp-2013, BARC, Mumbai.

6. **Mahesh K. Sharma**, R. N. Panda and S. K. Patra "Reaction dynamics of light mass nuclei in the frame work of Glauber model using relativistic mean field densities" , National conference NCNP-2013, School of Physics, Sambalpur University, Odisa.

7. **Mahesh K. Sharma**, Manoj K. Sharma and S. K. Patra "Reaction dynamics of halo nuclei using Glauber model" , International conference ICRTNP-2012, Chitkara

University, Madopur, distt. Solan.

8. **Mahesh K. Sharma** and S. K. Patra "Nuclear reaction cross section for drip-line nuclei in Glauber formalism using relativistic mean field densities" , National symposium Snp-2012, Dehli University, New Dehli.

9. **Mahesh K. Sharma** and S. K. Patra "Quest of halo in ^{31}Ne using Glauber model formalism with deformed relativistic mean field density" , National symposium Snp-2012, Dehli University, New Dehli.

10. **Mahesh K. Sharma**, M. S. mehta and S. K. Patra "Nuclear reaction cross section of ^{22}C using Glauber Model and Relativistic mean field formalism" , National symposium Snp-2011, Andhara University, Vishakhapatnam.

11. **Mahesh K. Sharma**, M. S. Mehta and Manoj K. Sharma "The halo Structure of ^{11}Be halo nucleus using Glauber model and Relativistic Mean Field formalism" , AMRP-2011, Sant Longowal Institute of Engineering and Technology, Sangrur, Punjab.

Contents

List of Figures

List of Tables

Chapter 1

Introduction and Literature Review

1.1 Introduction

The idea of nucleus was briefed in 1911 by Ernest Rutherford after performing the famous experiment also known as Geiger-Marsden gold experiment. This was the revolutionary idea for the interpretation of the atomic structure. Since, more than a century have passed in pursuit to understand the behavior of nucleus and related nuclear structure phenomena. The nucleus is a many body complex dynamical system, consisting of various nuclear properties and associated aspects. Large number of experimental observations and theoretical analysis have been performed to predict vast variety of nuclear isotopes. As per the description of nuclear isotopes, the nuclear landscape is broadly divided into four parts. The first part includes stable nuclei (i.e $\beta-$stability line) and the rest three comprise of neutron rich, proton rich and super-heavy regions. All these except the stable nuclei fall in the category of unstable nuclei, because of their very short life time. Most of stable nuclei and their structural properties have been extensively studied and relatively better understood. Therefore this region of nuclear chart is of least interest for nuclear physicist. On the other hand neutron rich, proton rich and super-heavy regions have not been fully

explored, and hence are of current interest. So many experiments were performed in this area since the mid of 19^{th} century, and some very interesting observations have been explored in these regions. The proton rich nuclei are very few in number, whereas their counterpart i.e neutron rich side is enriched with vast variety and number. The brief description of different regions of nuclear chart is described below.

1.1.1 β-Stability Line

The existence of naturally occurring elements and relative stability of these elements is one of the major question for the scientific community since more than one century. It has been observed that, stable elements exist very few in number from hydrogen to lead element [1]. One of the important component of an atom is the nucleus, which occupies the entire mass of the element. The nucleus is composed of nucleons and the interplay of nuclear forces, which exist between them makes it even more interesting. The main challenge for nuclear physics community is that how many neutrons and protons form a stable nucleus. It has been found that about 300 nuclide are naturally occurring and having half life more than 80 million years or greater than the life of earth. These nuclei are categorized as stable isotopes and are also known as $\beta-$ stable particles. The Fig. 1.1 represents the nuclear land scape in which, black boxes represent the stable nuclear isotopes. The straight line shows the N=Z symmetry line. One may clearly see from the figure that, these stable isotopes are tilted towards the neutron number as one move towards higher mass number. Here, another interesting aspect is the existence of other isotopes or identification of some new isotopes for these elements. The various experimentalists and theoreticians are working on these aspects of nuclear physics. After mid 1980, the development of radioactive ion beam (RIB) in various laboratories around the world opened up a new approach to study the isotopes away from the $\beta-$ stability

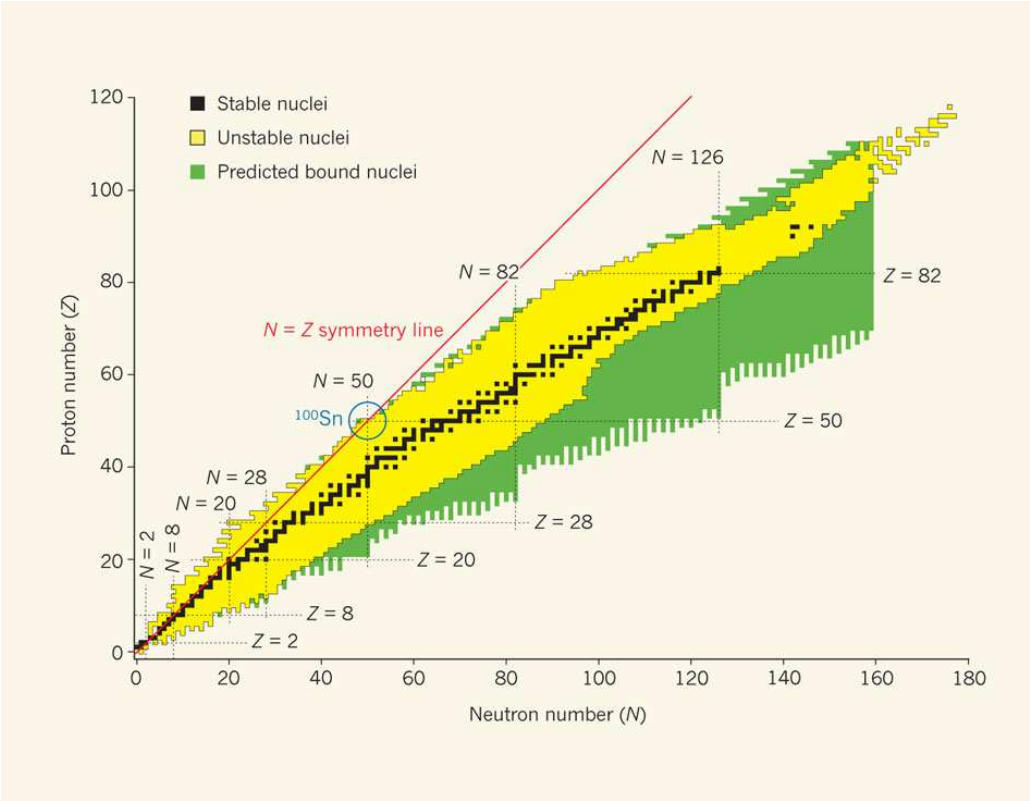

Figure 1.1 Nuclear landscape of stable, unstable and theoretically predicted nuclei

line. The experimental groups from DUBNA [2,3], RIKEN [4] and GANIL [5] are pioneer in this field, and many theoretical studies [6–16] have also been carried in the related areas of research. Approximately 2000 isotopes have already been synthesized artificially through various experimental laboratories. These isotopes are unstable in nature and are represented by yellow boxes in the nuclear land scape. The possibility of sustaining these isotopes for longer life time is another field of investigation. Relevant theoretical formalisms seem to suggest that more than 5000 isotopes are yet in the pipeline to be explored in near future.

1.1.2 Proton rich nuclei

There are very few nuclei which exhibit proton rich characteristics, as depicted in the nuclear land scape. The reason of non-feasibility of these nuclei is due to repulsive in-

teraction between the protons in proton rich elements. Burbidge *et al.*, [17] and A. G. W. Cameron [18] suggests that most of the naturally occurring nucleides beyond the iron nucleus can be made via two kinds of neutron capture processes, known as s-process and r-process. Broadly speaking, the formation of proton rich nuclei may be possible either by (p,γ) process or (γ, n) process. In the first process, successive addition of protons takes place for the formations of proton rich nuclei. But in the lateral process, neutrons of the nucleus are removed in the sequence of photodisintegrations to enrich the nucleus by proton.

1.1.3 Neutron rich nuclei

The neutron rich nuclei are synthesized primarily via s-process or r-process. The r-process is responsible for the creation of approximately half of the neutron-rich atomic nuclei heavier than iron element. The slow-neutron-capture-process (s-process) is a nucleosynthesis process which occurs at relatively low neutron density and intermediate temperature. Under these conditions, the heavier nuclei are created via neutron capture by increasing the atomic weight of the nucleus by one unit. During this process, the neutron changes to proton by decay of β^--particle, for creating a daughter nucleus of higher atomic number, where the rate of neutron capture by atomic nuclei is relatively slow as compared to the rate of radioactive β^--decay. In other words, in s-process the β decay can occur just before every successive neutron capture process. Therefore s-process produces stable isotopes by moving along the valley of β-decay stable isobars in the nuclear chart, where as the r-process (rapid-neutron capture process) differs from the s-process by its faster rate of neutron capture than the β^--decay. Consequently more than one neutron gets captured before β-decay in the r-process. The r-process is entitled by their name because of the succession of rapid neutron captures. The r-process occurs to a slight extent in

thermonuclear weapon explosions, and was responsible for the historical discovery of the elements Einsteinium (Z=99) and Fermium (Z=100) *etc.*

1.1.4 Super-heavy Nuclei

The extreme right part of the landscape is super-heavy region. The elements heavier than Uranium (Z=92) are not usually found in the nature, but they can be synthesized in the laboratories and exhibit a very short life time. In such heavier atomic nuclei, relatively larger number of protons repel one another due to their positive charges, making them less stable, or more radioactive. Although the definition of the super-heavy elements (SHE) is debatable, but we generally refer to elements with Z$\geq$100 as super-heavy elements. Most of these elements have life time ranging from a few milliseconds to few minutes. Newly investigated element Z=117 [19–23] has a life lime of about few thousandths of a second. It is relevant to mention here that the stability of these elements at island of inversion may be due to possible occurrence of magicity in the super heavy region, which is of current interest in concern of possible stable island beyond Z=100. The scientists working in this area are doing extensive effort to explore super-heavy magicity so as to synthesize stable nuclear systems in this extreme mass region of periodic table.

1.1.5 Drip line

The general statement regarding the drip-line is conceptualized as the boundary of the nuclear particle-stability line. If we add or remove successive neutron or proton in the stable nuclear isotopes, a point is reached for a given Z, where if one extra neutron is pulled out, the proton becomes unbound with in the isotope. Similarly if one more neutron is added to that isotope then neutron also doesn't stay in bound state with in that nucleus. These limits define, respectively, the proton and neutron drip-lines. Equivalently, one can

say that the point at which the separation energy of nucleus becomes zero is known as drip-line. The proton drip-line region is relatively better explored in the nuclear landscape, where as its neutron counter part is being extensively explored. Although the drip-line is well established up to oxygen, ground state of ^{23}O and ^{24}O are unbound. Also conventionally expected double closed shell nucleus ^{28}O as well as ^{26}O which have even-even stability are found to be in their unbound states. There are some other nuclei well beyond the drip-line, such as ^{15}Be, ^{20}B, ^{21}C, ^{23}C and ^{24}N *etc.*, which are of recent interest. Such nuclei undergo single neutron emission and their structural effects are still not fully known. The experiments at RIKEN [4] and GANIL [5] observed the existence of ^{34}Ne and ^{37}Na which were earlier predicted to be unstable nuclei. The recent discovery of ^{40}Mg and ^{42}Al [24] which are well beyond the drip-line by various mass formula, challenge the predictive power of theoretical models for a definite neutron drip-line. In addition to this, the change of shell structure, one/two neutron halo, skin effect and bubble shape in density profiles are some of the interesting phenomenon identified beyond the valley of stability. The brief idea of these issues are given in subsequent subsection of exotic nuclei.

1.1.6 Exotic Nuclei

Some of the nuclear systems show the unusual behavior as compared to their neighboring isotopes. The nuclear systems are said to be exotic, if they exhibit unusual decay modes, which are not seen at near stability region such as proton radioactivity and β-delayed particle emission *etc.* In β-delayed emission, after β decay the nucleus gets highly excited and can emit one/more particles (such as one/two protons or neutrons or an alpha particle). Hence nuclear structure studies of such exotic systems are different than those away from the $\beta-$stability line, the neutron rich side carries special attention in recent times. These nuclei are highly unstable and lie far from the valley of β-stability line. Such

nuclei exhibit unusual phenomena and provide an extreme test for existing models. The properties of these nuclei are strongly relevant to explosive astrophysical events such as supernova *etc.*. The studies of nuclear matter under such extreme conditions, in which the nuclei behave quite different as compared to stable nuclear systems, are of prime importance and are being studied extensively. These extreme conditions include nuclear behavior at high temperature, high density *etc.* beside forming extreme combinations of N/Z ratios. The N/Z ratio depends on the nature of the attractive nuclear force that binds the protons and neutrons in the nucleus and complex interplay with the disruptive Coulomb or electrical force that pushes the positively charged protons apart. It is relevant to mention that, the nuclear shape and deformation effect also play very significant role in exhibiting the behavior of the exotic nuclear systems. A brief account of deformed shell closure effects is described below

1.1.6.1 Shell closure effect for deformed systems

The spherical shell model was developed to explain the extra stability of some nuclei with their proton number Z= 2, 8, 20, 50, 82 and neutron numbers N= 2, 8, 28, 50, 82 and 126 called as magic numbers. These magic shell nuclei form spherical shape and very stable nuclear configuration. Whereas with the advancement in experimental laboratories and measurements of mass/Coulomb excitation using radioactive ion beam (RIB) for neutron rich 'Na' and 'Mg' isotopes suggests the breaking of nuclear shell closure *i.e.* N=20 [16]. The investigation by neutron separation energy (S_n) and interaction cross section measurements for $p-sp$ and sd shell region along with some other observations suggests the new magic number N=16 near the drip-line [25, 26], which is also supported by Hoffman *et al.* [27]. A recent ion beam measurement at RIKEN [28] suggests some new magic numbers at N=6, 16, 32, 34 and so on, with increasing proton neutron imbalance,

which breaks down the conventional order of nuclear magicity. This phenomenon of vanishing the known shell gaps and the development of new stability zones, causes a mixing of normal and intruder configurations, which in turn significantly influence the properties of such nuclei [29, 30]. These approaches include the concept of nuclear shape coexistence. The struggle of bands (levels) occur in the nucleus, which overlap in their energy but having different from their decays modes. These facts are due to the reason of their different coexisting nuclear shapes. Hence the shapes or the structure of such nuclei are very much important throughout the nuclear systems away from the stability line. Hence significant advancements have been made in Shell model after the discovery of new magic numbers. These new numbers may be called as the deformed magic numbers because they stabilize a nucleus in a deformed shape, just as the earlier known magic numbers exhibit stability aspect of a spherical shape nuclei. The deformed magic numbers identified so far include Z of 38 and N of 6, 16, 32, 34, 38, 60 and 62 [25–28, 31, 32]. It is relevant to mention here that the magicity in the super heavy region is of current interest in concern of possible stable island beyond Z=100. Although there is a general consensus about the next neutron magic at 184. The next proton magic after Z=82 is still not fully explored and there seems a competition among Z=114, 120 and 126 for the same. The deformed shapes of target-projectile combination of heavy ions employed for synthesis of SHE, may impart a significant insight to explore this issue. On the other extreme of periodic table (lower mass region) deformation effects provide another interesting area of halo shapes, which is briefly described below.

1.1.6.2 Neutron/Proton halo shapes

Another interest in the studies of these exotic nuclei is to investigate the effect of one or two neutron/protons halos and neutron skin [33–35]. Such effects are caused by the extremely

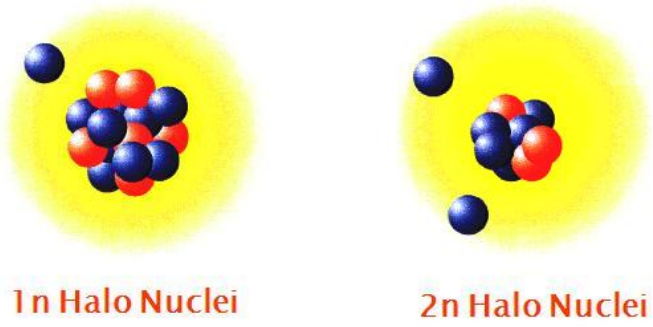

Figure 1.2 Structure of one and two neutron Halo [7].

weak bound neutrons/protons that decouple from the nuclear core. The nucleon in the halo nuclei at a large distance from the core gives rise to a wave function having a long tail. Fig 1.2 shows the structures of one and two neutron halo nuclei. The central part of these figures consists of a core of nucleus surrounded by loosely bounded one or two neutrons/protons. The two neutron halo's are also known as Borromean nuclei [36, 37]. It is of large interest to study the existence of bound states of two nucleons (neutrons or protons) with core in the Borromean structure. The reaction cross sections with halo projectiles such as ^{6,8}He, ^{11}Li and ^{11,14}Be [38] have been found anomalously larger. The root mean square (rms) matter radius of such nuclei is found to be much larger than that of the neighboring ones. The measurement of longitudinal momentum distribution for $^{16-18}$C isotopes after one-neutron breakup from $^{17-19}$C isotopes using the fragment separator observed narrow value of full width half maximum (FWHM) for ^{18}C ($\sim 44.3\pm5.9$ MeV/c), which indicates that ^{19}C is a one-neutron halo [39]. The measurement of nuclear reaction cross section for ^{19,20,22}C [40] shows that the drip-line nucleus ^{22}C has halo structure. The halos in deformed nuclei have been investigated in several mean field calculations [41, 42]. However the three body model calculations [43] suggest that it is unlikely to find halos in deformed drip-line nuclei because the correlations between the nucleons due to static or dynamic deformations of the core suppress the formation of halo. The isotope ^{31}Ne having

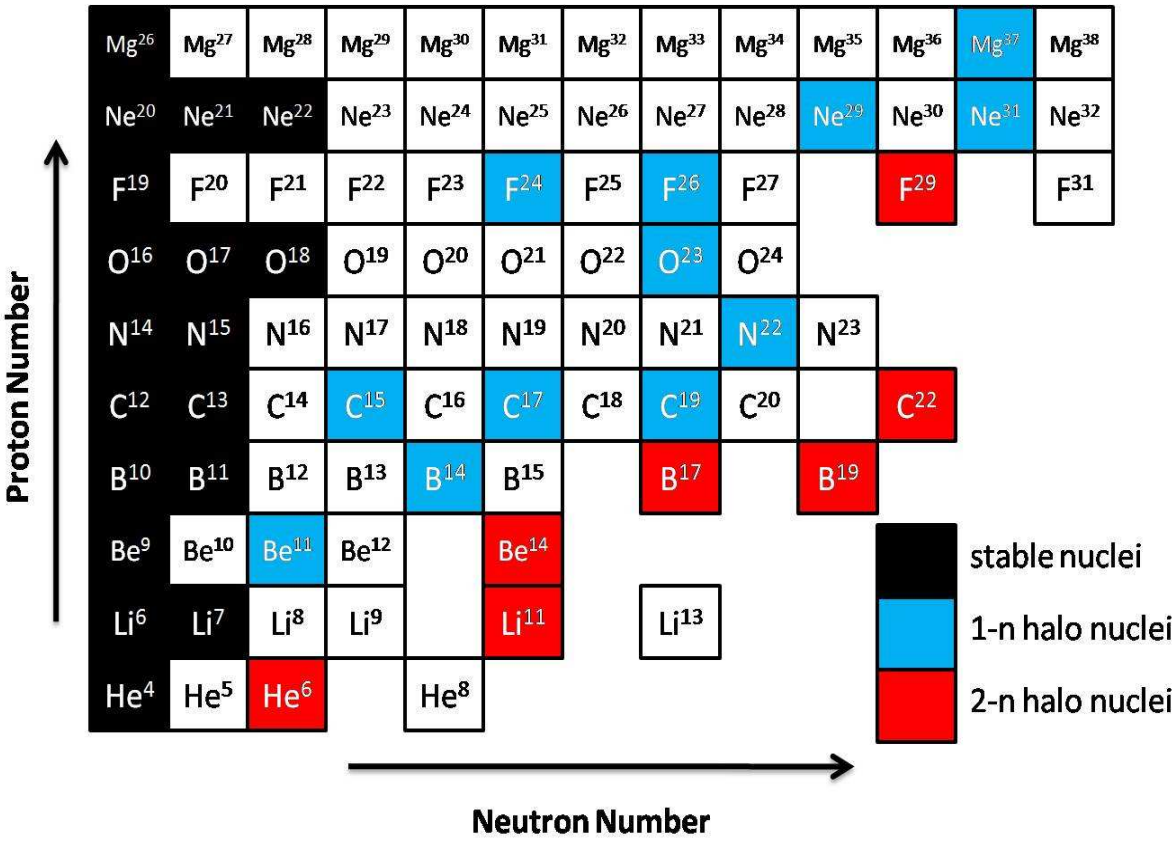

Figure 1.3 Nuclear landscape for He-Mg isotopes with probable one and two neutron halo candidates.

neutron number N=21, seem to break the shell closure structure. As a consequence, a large deformation associated with the strong intruder configuration puts it at "island of inversion". Hence the structure of these exotic nuclei in the extremes of isospins is characterized by several interesting features. The nuclei toward the drip lines have extremely small separation energy for the outermost nucleons, as a result the Fermi level of such systems lies close to the particle continuum state. The density distribution shows an extended tail with a diffused neutron skin and neutron halo [34]. The definition of a halo nucleus is still being debated, but at least three basic conditions are required for the nuclei to be halo: (i) low separation energy of the valance particle (or particle clusters), (ii) a wave function that is in a low relative angular momentum state (preferably an s-wave or p-wave), (iii) decoupling from the core. Figure 1.3 shows the nuclear land scape

of He-Mg isotopes with probable cases of one or two neutron halo candidates [7, 44–50].

Bubble effect in the densities

Recently, one more phenomenon known as bubble effect in the densities has drown the attention of nuclear physists. The density distribution reveals the shape and the stability of the nuclear systems. In some of the nuclear systems, an extension in the tail part corresponds to their halo behavior as discussed above. However in certain cases another interesting fact is observed in context of the density profile. The densities of such cases is depleted from the center. The idea of the bubble effect has been given by Wilson [51]. This phenomenon gathered greater interest because it changes the shape of the density distribution from its normal form due to different mean field potential. Hence the conventional behavior of densities have been changed for such cases of nuclear systems. The bubble effect is found in some of nuclear systems like ^{22}O, ^{23}F, ^{34}Si, ^{36}S, ^{36}Ar, ^{46}Ar, ^{84}Se, ^{134}Ce, ^{174}Yb, ^{200}Hg *etc.* [52–54]. The possibility of the formation of the bubble nuclei from the lighter to super-heavy mass region is an open area of investigation. The major interest in this area is to investigate the structural changes of these nuclei, and subsequently to see the role of this effect on reaction dynamics. In the following sections, an effort has been made to give a brief description of nuclear structure and nuclear reaction mechanisms undertaken in this thesis.

1.2 Nuclear Structure

The atomic nucleus is a strongly-interacting, many-body quantum mechanical system which exhibits various shapes and excitation modes. These shapes are comprised of vast range covering from spherical to super deformed mode. Another interesting feature is the excitation of a single proton or neutron to collective vibrations and rotations of the nu-

cleons in the nucleus. The main interest of nuclear physicists is to explore these complex patterns of nuclear behavior by single mechanism. In this regard, nuclear structure and related features are studied by bulk properties of the nucleus like binding energy, rms radius, charge radius, deformation parameter, nucleon density distribution, single particle energy *etc.* For investigation of these properties, various phenomenological and microscopic theoretical models have been developed like Finite Range Droplet Model (FRDM) [55], Skyrme Hartree-Fock [56, 57], Relativistic Mean Field [58, 59] and Hartree Fock Bogulibov model (HFBB) [60, 61]. The recent theoretical formalism addressing many body nuclear systems generally follow up three different approaches: (i) ab-initio method, (ii) Self consistent mean-field method and (iii) Macroscopic-microscopic model with shell corrections. The ab-initio method has been developed with an aim to explain the nuclear scattering data by using the nucleon-nucleon potential. In this approach the nuclear matter behaves like a correlated quantum liquid due to strongly repulsive potential of the nuclear core. Hence to interpret such complex system, one needs highly sensitive many body theories [62, 63], which may provide the direct connection between the two nucleon problem and nuclear matter properties. The intermediate level between ab-initio and macroscopic-microscopic approach is the microscopic mean field theory, which is based on effective interactions briefly discussed below subsection.

1.2.1 Mean field theories

It is relevant to mention that both fully ab-initio method and shell model calculations are incapable to produce many properties of finite nuclei. Therefore effective mean field interaction gathered much attention in this regard. The mean field theories are based on effective interactions and concentrate on self consistent determination of the nuclear mean field interaction. The force parameters of mean field theory are few in numbers, which

have been adjusted by fitting the nuclear structure data. Hence the mean field potential of nucleons are estimated from nucleonic wave functions in Hartree-Fock theory. These theories are further generalized with mean field concept in the Hartree-Fock-Bogoliubov (HFB) equations [64] and widely used BCS approximation for the time-reversal-invariant systems. Hence these two different formalisms are used to a great degree for the calculation of pairing energy in the mean field theory to take care of nuclear pairing correlation in finite nuclear matter. The success of the Hartree-Fock approach strongly depends on the effective interactions. Presently, the standard models used in the mean field theory are non-relativistic mean field with (i) zero range Skyrme interaction [65], (ii) finite range Gogny interaction [66] and (iii) relativistic mean field theory [67]. The descriptions of non-relativistic and relativistic mean field theories are given below.

1.2.2 Non-relativistic mean field theory

The Hartree-Fock approach is based on the non-relativistic mean field theory with basic assumption that nuclear forces are effective just between pair of nucleons. Using this assumption, we can estimate the properties of many body nuclear systems, which consists of several hundred interacting particles under some effective interaction. The local approximation in Skyrme energy functional has several advantages. The direct and exchange terms of Skyrme-Hartree-Fock have the same structure, which significantly reduces the number of integrations required for the solution of field equations. Although non-relativistic mean field model with self consistent approach successfully describes many nuclear properties like binding energy, charge radius, matter radius, densities distributions, single particle energy states *etc.*. But this approach fails to predict accurate values of the binding energy and the saturation density, which is a well known 'coester band' problem [68, 69]. Hence the large number of parameter sets are available to study the

structure of many nuclear systems.

1.2.3 Relativistic mean field theory

In 1970's. another significant effort in the mean field theory has been done by Walecka [62] and Brochman [70, 71] by introducing relativistic approach. These models are based on the relativistic mean field approximation, which provide microscopic consistent and simple treatment of many body problems via adjustment of the model parameters, coupling constants and effective masses to the global properties of nuclei. The properties of whole periodic table can be described by this formalism. These models do not require any further fitting of parameters for the nuclei away from the stability line. Hence relativistic mean field theory is able to solve the problems of the saturation density and the binding energies for the finite nuclei and also gives spin-orbit interaction automatically. Although the bulk properties of nuclei with non-relativistic density dependant Hartree-Fock (DDHF) calculations using Skyrme forces are comparable to relativistic mean field formalism. But the RMF have some advantages over DDHF [72] as (i) the proper relativistic propagation of nucleons and retarded interaction are included automatically, (ii) the meson degrees of freedom are incorporated explicitly through self-consistency, (iii) spin-orbit interaction, which is a relativistic correction comes out automatically, (iv) Coester band Problem is solved in relativistic mean field. The further detail of non-relativistic Skyrme-Hartree-Fock and relativistic mean field formalisms are discussed in Chapter 2.

1.3 Nuclear Scattering and Nuclear Reaction

Another method to investigate the nuclear structure is through nuclear reaction. The resultant of interaction between the two nuclear systems (projectile and target) can be

understood either by nuclear reaction or by nuclear scattering. If the two interacting bodies exchange masses (nucleon) then interaction is called nuclear reaction otherwise the process is termed as nuclear scattering. The nuclear scattering is also a fundamental nuclear reaction in which a projectile and target interact with each other. During this interaction they do not exchange any particle with each other. So the total energy and momentum are always conserved. If they exchange some energy *i.e.* the target particle reaches to its excited state then the scattering is called 'inelastic scattering' else is known as 'elastic scattering'. The scattering is a peripheral phenomenon whereas the nuclear reactions cover the central and near central interactions. The nuclear interaction is a complex phenomenon which has been discussed below. Since elastic scattering is a peripheral process, it can be the most prominent tool to probe the tail of the wave function and hence the properties of the halo nuclei. As mentioned earlier the nuclear reaction and nuclear scattering results are used to measure the properties of nuclei. Those reactions which exchange energy or nucleons can be used to measure the binding energy, quantum numbers of energy levels and transition rates between levels *etc.*

In nuclear reaction, the nucleons of the projectile must interact with the nucleons of the target where energy plays a prominent role. The energy must be high enough to overcome the natural electromagnetic repulsion between the protons. This energy barrier is called as Coulomb barrier. If energy is below this barrier, the nuclei will bounce off each other. When a collision occurs between the projectile and a target nucleus, either the beam particle scatters elastically leaving the target nucleus in its ground state or the target nucleus is internally excited and subsequently decays by emitting radiation or nucleons. Some specific reactions are studied by measuring the angles and kinetic energies of the reaction products. The most important quantity of interest for kinematic variables is the interaction or reaction cross sections. There are two kinds of reaction

formalism, which are distinguished on the basis of energy. One is the low energy theory such as the Bass model [73], which is based on the one dimensional interaction potential between the two spherical nuclei and the second kind is based on high energy microscopic interactions like Glauber model [74] which is based on nucleon-nucleon collisions. The reaction cross sections give the measurement of the probability for a particular reaction to occur, which enhances our knowledge to interpret the size and the distribution of the nuclei. The decomposition of angular distributions for elastic scattering is a powerful tool for understanding the characteristics like nearside-farside (Fraunhofer) interference oscillations at forward angles, which provide the information about the potential in peripheral collisions. If the absorption is weak enough, then the trajectories of colliding systems contribute towards the farside scattering, which exhibit the rainbow type features, namely Airy maxima and minima. It is relevant to mention here that the heavy ion beams are of extreme relevance and have drawn much interest to explore nuclear reaction dynamics. Heavy ions are the nuclei with Z$\geq$2 and A$\geq$4. *ie* the nuclei heavier than the α-particle are called heavy ions. The heavy ion elastic scattering data is the main source of information on the above discussed subjects. Along with it, a large percentage of our knowledge on the properties of nuclei is derived from nuclear reactions. The study of nuclear reactions is important because of its impact and relevance on the related fields of investigation. Measurement and calculation of nuclear reaction cross section observable is of great importance for overall understanding of the reaction mechanism and associated dynamical behavior. The nuclear reaction phenomena are broadly classified on the basis of projectile energy range as low, intermediate and high energy reaction dynamics. A brief discussion of low and intermediate energy and associated nuclear phenomena is given below:

1.3.1 Low energy nuclear reactions

For nuclear reaction at low incident energy range ($E \leq 30$ MeV/nucleon), the mean field effect dominates, and a microscopic description of the process is so difficult to observe that the strong absorption effects dominate the interactions and allow one to probe only the external part of the nuclear surface for which angular distributions gives the typical diffraction pattern. The less availability of data in refractive effect leads to large ambiguities in the determination of the real part of the optical potential. The nuclear reaction requires an energetic nuclear probe (projectile beam) coming from an accelerator or radioactive substance to be incident on the target. Depending upon the reaction conditions, different types of reactions may occur. However a broad classification may divide the nuclear reactions into two categories;
(1) Compound nucleus reaction and (2) Non-Compound nucleus reaction.

Compound nucleus reaction

In this reaction the projectile hits the target and forms a compound nucleus for a relatively long time period (10^{-15} -10^{-17} sec). During this time period, both the nuclei are in the single excited state known as the compound nucleus (CN) state. The decay from this state (excited state) takes place by an evaporation of nucleons from the CN by γ-decay, α-decay, evaporation residue and fission. Fission fragments may also have a significant contribution from the intermediate mass fragments (IMFs) and heavy mass fragments (HMFs) [75]. It may be noted that the fusion-fission is one of the most important phenomena studied at low energy region. In the fusion reaction, two light mass nuclei are combined to form a big massive nucleus by releasing a huge amount of energy. For example, the two isotopes of hydrogen combine to form helium by releasing 17.6 MeV energy in the form of kinetic energy. On the other hand an unstable nucleus may break up into two or more small

nuclei by the release of large amount of energy. This process is called fission. The nuclear fission and possibly nuclear fusion reactions will be one of the major energy source of the future power generation. The process of nuclear fission may be caused by the interplay between the nuclear forces of attraction and the Coulombic repulsion. If the repulsive force increases by bombarding the neutron to the nucleus and crosses the barrier height, then the nucleus breaks into small fragments. Along with the product nuclei, it also releases some neutron which further continues the process of fission called as chain reaction. The isotopes that can sustain a fission chain reaction are called nuclear fuels and are said to be fissile materials [76]. The most common fissile fuels are ^{235}U and ^{239}Pu. Mostly the nuclear fuels undergo a spontaneous fission at a very slow rate and decay by emitting α, β particles *etc.*. The fusion generally occurs for lighter elements and likewise the fission normally occurs for heavier nuclei. But there are extreme astrophysical events that can lead to short period fusion with heavier nuclei. This is the process that gives rise to nucleosynthesis, the creation of the heavy elements during events such as supernovas.

Non-Compound nucleus reaction

On the other hand for non-compound nuclear reaction, the life time of interaction is very small of the order of 10^{-22} sec as compared to the life time of formation of compound nucleus. In addition to the compound nucleus, some non-compound nucleus decays like direct reaction, pre-equilibrium fission [77], quasi-fission or Deep inelastic collision (DIC) *etc.* may also take place. The direct reaction includes various nuclear processes like elastic and inelastic nuclear reactions, Pickup or stripping reactions *etc.* A brief account of stripping, pick up and deep in elastic interactions are given below as illustrative examples. The **stripping reaction** is a nuclear reaction in which some part of the projectile nucleus interacts with the target nucleus, and the remaining part proceeds with almost similar

momentum on the same direction. This reaction was first described by S. T. Butler [78]. The deuteron stripping reactions have been used to study the nuclear reactions and structure of O^{16}(d,p)O^{17}.

On the other hand the **pick-up** reaction is complimentary to the stripping reaction. In which one or more nucleons are taken away from the target nucleus by the projectile nuclei without changing the structure of rest of the nucleons. An example of the pick-up reaction is Ca^{40}(p,d)Ca^{39}.

The last case of nuclear reaction, in which two nuclei interact strongly, dissipating sizable amount of energy and exchange energy and nucleon, while their surfaces overlap for a brief period corresponding to the rotation of intermediate di-nuclear complex is known as **deep inelastic collision** (DIC). The DIC may take place if the energy of the projectile is 2-3 MeV/nucleon above the Coulomb barrier.

1.3.2 Intermediate energy nuclear reactions

The intermediate energy range of nuclear systems has been generally classified from few decades of MeV/nucleon to few GeV/nucleon. At this energy range the nucleus-nucleus interaction is dominated by free nucleon-nucleon collision, which suggests that the surface transparency effect increases with increase of the energy over this region. This effect of increase of energy also appears in the measurements of reaction cross section, which exhibits the similar type of energy dependence as the one seen in elementary nucleon-nucleon cross sections. If the energy of the projectile goes above 30 MeV/nucleon, the system is said to be an in extreme excited state and the temperature of such state is very high. Further by increase of the projectile energy up to 200 MeV/nucleon, the multi-fragmentation process starts taking place during collision, which makes the nuclear system in boiling state. The multi-fragmentation is the process of breaking of colliding nuclei

into several light, medium and intermediate mass fragments with huge number of free particles. If the energy of an incident projectile is within the range of 100 MeV/nucleon to few GeV/nucleon, the system is in the highly excited state and emits various particles through multi-fragmentation phenomenon.

The elastic scattering cross sections of protons and neutrons give the essential data and eventually help to reconstruct the nucleus-nucleus interaction. It is relevant to mention that, a complete theory of nuclear structure and dynamics must start with this elemental interaction. The measurements of elastic and inelastic scattering of electrons, protons, and neutrons from nuclei provide the tools for the investigation of nuclear size, shape, binding energy, and other nuclear properties with the help of nuclear models.

In present work, we have used the Glauber model approach [74, 79], which is being used quite extensively to investigate the nuclear reaction dynamics. The nuclear reaction cross sections, one or more nucleon removal cross sections, angular elastic differential cross sections and longitudinal momentum distribution observable can be estimated using this method. The importance of this model is that, all the above mentioned quantities can be obtained from the nuclear densities or wave functions. We plan to use the densities from well known relativistic mean field (RMF) model and non-relativistic Skyrme Hartree-Fock (SHF) model for the comparison of results with each other. The basic ingredient of SHF model is its Hamiltonian density functional and RMF model is its relativistic Lagrangian density functional for nucleon-meson many body system. These models are well known and well described as SHF [56, 57, 80] and RMF [68, 81–83] with self consistent mean field approach [84]. The older versions of these models have some limitations but the recent formalisms are quite efficient to predict the bulk properties of nuclei not only at the $\beta-$stability line, but also for the nuclei lying away from the $\beta-$stability line. The microscopic approach of these models provide us the accurate densities and wave functions

which are the main ingredient of the Glauber formalism. The main significance of this systematic approach rely on a very small number of fitting parameters, which enable a rather strong reproducing power of the reaction dynamics of stable as well as drip line region. The details of formalism used are discussed in Chapter 2.

1.4 Summary of the Thesis

A brief description of methodology, calculations, observations, results and conclusion *etc.* is presented in the following Chapters.

Chapter 2

A brief description of formalism used for the investigation of the nuclear reaction dynamics and associated nuclear structure have been explained in this chapter. The details of both relativistic mean field and non-relativistic mean field formalisms have been given along with the used parameters sets. The details of reaction model (Glauber model) and its description along with the process of using the densities from these mean field formalisms has also been described in brief.

Chapter 3

In this chapter, the bulk properties like binding energy (B.E.), root mean square radius (r_m), root mean charge radius (r_c), quadrupole deformation parameter (β_2), nucleonic density distributions *etc.* have been studied for low to medium mass nuclear systems using both relativistic mean field and non-relativistic mean field formalisms. The comparison of bulk properties using parameters NL3*(NL3) and NL-SH for some test cases in relativistic mean field and SkI4 and SLy4 in non-relativistic mean field has been discussed for the

appropriate choice of parameters. The comparison of bulk properties is studied using both spherical and deformed model approaches. The results are also compared with the experimental data or Finite Range Droplet Model (FRDM), wherever available. The subsequent study of the role of bosonic and fermionic model space is also done before doing calculation using RMF formalism for these massive ranges. The role of BCS-pairing is also analysed for better understanding of its effect on bulk properties for isotopes of Ne, Mg and Si with in the RMF formalism.

Chapter 4

In this chapter, probable bubble nuclei of light mass region have been investigated through density profile using both RMF and non-RMF formalisms. Further bulk properties like binding energy and charge radius are also compared with the relativistic mean field formalism (for both deformed and spherical approach) along with the non-relativistic mean field formalism. The systematic study of the density profile and the depletion factors *etc.* have been exercised to analyze the probable cases of bubble nuclei.

Chapter 5

Chapter 5 contains the systematic study of the reaction dynamics within light to medium mass region using Glauber model. The various inputs of the Glauber model like energy and isospin dependant parameters, densities in Gaussian form *etc.* are described in brief. The microscopic mean field densities are used after conversion in terms of Gaussian coefficients and accuracy of the Glauber model is exercised on the basis of density profile. First of all, the sensitivity of converted densities are tested for some projectile/target nuclei. After that the role of fitting of densities in 2-Gaussian and 4-Gaussian form are studied on reaction cross sections of various reaction systems. The role of deformed densities is

also investigated on reaction cross sections studies using spherical and deformed RMF approaches. The comparative study of the reaction cross sections are also done by using the non-relativistic Hartree-Fock and relativistic mean field densities.

Chapter 6

Chapter 6 contains the recent interest of halo nuclear systems. The bulk structural properties mentioned in Chapter 3 are also studied along with, one and two neutron separation energy and single particle energy of some halo nuclear systems using RMF and non-RMF formalism. The reaction cross sections of these nuclear systems have been studied with Glauber two body model by using densities of mean field formalisms. The detailed study of reaction dynamics of some newly identified halo nuclear systems (^{31}Ne and ^{37}Mg) have been carried out in this chapter. The reaction cross section, angular differential elastic cross section, one nucleon removal cross section and longitudinal momentum distribution parameters are used to interpreted the halo structure of these nuclear systems.

Chapter 7

The summary of thesis work and scope of further extension have been given in this Chapter.

Bibliography

[1] Sonzogni, Alejandro "Intractive Chart of Nuclides" National Nuclear Data Center, 'Brookhaven National Laboratory' Retrieved 2008-06-06.

[2] Yu. Ts. Orgenessian *et al.*, Phys. Rev. C **70**, 064609 (2004).

[3] Yu. Ts. Orgenessian *et al.*, Phys. Rev. C **71**, 029902 (2005).

[4] M. Notani *et al.*, Phys. Lett. B **542**, 49 (2002).

[5] S. M. Lukyanov *et al.*, J. Phys. G **28**, L41 (2002).

[6] B. Abu-Ibrahim and Y. Suzuki, Phys. Rev. C **61**, 051601 (2000).

[7] B. Abu-Ibrahim and Y. Suzuki, Phys. Rev. C **62**, 034608 (2000).

[8] W. Horiuchi, Y. Suzuki, B. Abu-Ibrahim and A. Kohama, Phys. Rev. C **75**, 044607 (2007).

[9] W. Horiuchi, Y. Suzuki, P. Capel and D. Baye, Phys. Rev. C **81**, 024606 (2010).

[10] S. K. Charagi and S. K. Gupta, Phys. Rev. C **41**, 4 (1990).

[11] A. Bhagwat and Y. K. Gambhir, Phys. Rev. C **73**, 024604 (2006).

[12] A. Bhagwat and Y. K. Gambhir, Phys. Rev. C **73**, 054601 (2006).

[13] P. Shukla, arXiv: nucl-th/0112039v1.

[14] A. Shukla, B. K. Sharma, R. Chandra, P. Armugam and S. K. Patra, Phys. Rev. C **76**, 034601 (2007).

[15] S. K. Patra, R. N. Panda, P. Armugam and Raj K. Gupta, Phys. Rev. C **2**, 064602 (2009).

[16] A. Ozawa *et al.*, Phys. Rev. Lett. **84**, 5493 (2000).

[17] E. M. Burbidge, G. R. Burbidge, W. A. Fowler and Fred Hoyle, Mod. Phys. **29**, 547 (1957).

[18] A. G. W. Cameron, Publications of the Astronomical Society of the Pacific **69**, 201 (1957).

[19] Yu. Ts. Oganessian *et al.*, Phys. Rev. Lett. **104**, 142502 (2010).

[20] Yu. Ts. Oganessian *et al.*, Phys. Rev. C **83**, 054315 (2011).

[21] Yu. Ts. Oganessian *et al.*, Phys. Rev. Lett. **109**, 162501 (2012).

[22] Yu. Ts. Oganessian *et al.*, Phys. Rev. C **87**, 054621 (2013).

[23] J. Khuyagbaatar *et al.*, Phys. Rev. Lett. **112**, 172501 (2014).

[24] T. Baumman *et al.*, Nature **449**, 1022 (2007).

[25] C Thibault *et al.*, Phys. Rev. C **12**, 644 (1995).

[26] C. Detraz *et al.*, Phys. Rev. C **19**, 164 (1979).

[27] C. R. Hoffman *et al.*, Phys. Rev. Lett. **100**, 152502 (2008).

[28] T. Otsuka *et al.*, Phys. Rev. Lett. **87**, 082502 (2001).

[29] S. K. Patra, R. K. Gupta and W. Greiner, Mod. Phys. Lett. A **12**, 1727 (1997).

[30] P. Doornebal *et al.*, Phys. Rev. Lett. **103**, 032501 (2009).

[31] H. Nakada and K. Sugiura, Prog. Theor. Exp. Phys. **033**, D02 (2014).

[32] E. Sahin *et al.*, Phys. Rev. C **91**, 034302 (2015).

[33] I. Tanihata *et al.*, Phys. Rev. Lett. **55**, 2676 (1985).

[34] I. Tanihata *et al.*, J. Phys. G: Nucl. Part. Phys. **22**, 157 (1996).

[35] W. Mitting *et al.*, Phys. Rev. Lett. **59**, 1889 (1987).

[36] M. A. Cobis, D. V. Fedorov and A. S. Jenson, arXiv:1970.8034v1 [Nucl-th] (1997).

[37] M. T. Yamashita *et al.*, Phys. Lett. B **697**, 90 (2011).

[38] I. Tanihata *et al.*, Phys. Lett. B **287**, 307 (1992).

[39] D. Bazin *et al.*, Phys. Rev. Lett. **74**, 18 (1995).

[40] K. Tanaka *et al.*, Phys. Rev. Lett. **104**, 062701 (2010).

[41] J. Pei, F. Xu and P. D. Stevenson, Nucl. Phys. A **765**, 29 (2006).

[42] H. Nakada, Nucl. Phys. A **808**, 47 (2008).

[43] F. M. Nunes, Nucl. Phys. A **757**, 349 (2005).

[44] I. Hamamoto, Phys. Rev. C **81**, 021304(R) (2010).

[45] Y. Urata, K. Hagino and H. Sagawa, Phys. Rev. C **83**, 04130 (2011).

[46] K. Minomo, T. Sumi, M. Kimura, K. Ogata, Y. R. Shimizu and M. Yahiro, Phys. Rev. C **84**, 034602 (2011).

[47] M. Takechi *et al.*, Phys. Lett. B **707**, 357-361 (2012).

[48] M. Takechi *et al.*, Phys. Rev. C **90**, 061305 (2014).

[49] S. Watanabe *et al.*, EPJ Web of conference **66**, 03095 (2014).

[50] N. Kobayashi *et al.*, Phys. Rev. Lett. **112**, 242501 (2014).

[51] H. A. Wilson, Phys. Rev. **69**, 538 (1946).

[52] K. T. R. Davies, C. Y. Wong and S. J. Kreiger, Phys. Lett. B **41**, 455 (1972).

[53] M. Grasso *et al.*, Int. J. Mod. Phys. E **18**, 2099 (2009).

[54] M. Grasso *et al.*, Phys. Rev. C **79**, 034318 (2009).

[55] P. Moller, W. D. Myers, W. J. Swiatecki and J. Treiner, Preceeding of 7^th International conference on atomic masses and fundamenetal constants. Nuclear Science Division, Lowrence Berkeley Laboratory, University of California, Berkeley Division.

[56] E. Chabanat, P. Bonche, P. Hansel, J. Meyer and R. Schaeffer, Nucl. Phys. A **627**, 710 (1997).

[57] J. R. Stone *et al.*, Phys. Rev. C **68**, 034324 (2003).

[58] Y. K. Gambhir, P. Ring and A. Thimet, Ann. Phys. (N. Y.) **198**, 132 (1990).

[59] M. D. Estal, M. Centelles, X. Vinas and S. K. Patra, Phys. Rev. C **63**, 024314 (2001).

[60] M. Bender and P. H. Heenen, Phys. Rev. C **78**, 024309 (2008).

[61] J. P. Ebran, E. Khan, D. Pena Arteaga and D. Vretenar, Phys. Rev. C **83**, 064323 (2011).

[62] B. serot and J. D. Walecka, Adv. Nucl. Phys. **16**, 1 (1986).

[63] R. Brockmann and R. Machleidt, Phys. Rev. C **42**, 42 (1990).

[64] H. J. Mang, Phys. Rep. **18**, 325 (1975).

[65] D. Vautherin and M. Veneroni, Phys. Lett. B **29**, 203 (1969).

[66] J. Decharge and D. Gogny, Phys. Rev. C **21**, 1568 (1980).

[67] J. D. Walecka, Ann. Phys. (N. Y) **83**, 491 (1974).

[68] R. Machliedt, Advances in Nuclear Physics, edited by J. W. Negelea and E. Vogt (Plenum Press, New York) **19**, 189 (1989).

[69] F. Coester, S. Cohen, B. D. Day and C. M. Vincent, Phys. Rev. C **1**, 769 (1970).

[70] R. Brockmann, Phys. Rev. C **18**, 1510 (1978).

[71] R. Brockmann and W. Weise, Nucl. Phys. A **335**, 365 (1981).

[72] C. J. Horowitz and B. D. Serot, Nucl. Phys. A **368**, 503 (1981).

[73] R. Bass, Nuclear Reaction with Heavy Ion: Texts and Monographs in Physics (Springer-Verlag), Berlin (1980).

[74] R. J. Glauber. In "Lectures in Theoretical Physics". Eds. W. E. Brittin *et al.*, New York **1**, 315 (1959).

[75] M. Balasubramaniam, Rajesh Kumar, Raj K. Gupta, C. Beck and Werner Scheid, J. Phys. G: Nucl. Part. Phys. **29**, 2703 (2003).

[76] L. Satpathy, S. K. Patra and R. K. Chaudhury, Pramana J. Phys. **70**, 87 (2008).

[77] Manoj Kumar sharma *et al.*, Phys. Rev. C **91**, 014603 (2015).

[78] S. T. Butler, Phys. Rev. **80**, 6 (1950).

[79] P. J. Karol, Phys. Rev. C **11**, 1203 (1975).

[80] J. R. Stone and P. G. Reinhard, Prog. Part. Nucl. Phys. **37**, 193 (1996).

[81] S. K. Patra and C. R. Prahraj, Phys. Rev. C **44**, 2552 (1991).

[82] M. Del Estal, M. Centelles, X. Vinas and S. K. Patra, Phys. Rev. C **63**, 024314 (2001).

[83] P. Ring, Prog. Part. Nucl. Phys. **37**, 193 (1996).

[84] M. Bender, P. H. Heenen, P. G. Reinhard, Rev. Mod. Phys. **75** (2003).

Chapter 2

Methodology

The area of nuclear research has progressed intensively due to availability of large experimental data during the last few decades. This effort has produced many exotic phenomena and a significant advancement in this area in turn provides a large body of new materials and related insights. Many theoretical formalisms are available to explore the structure of nuclear systems, which get consistently modified as per advancement in the related field. One of the most successful approach for the interpretation of the exotic nuclear systems is the self consistent mean field theory. The Hartree-Fock mean field [1, 2] is one of the approximation based on the non-relativistic approach and is extensively used to investigate the bulk properties of nuclei. The most important aspect of this formalism is the choice of an appropriate effective interaction potential. Presently, two different mean field effective interactions are being used in this concern. One of them is a finite range Gogny and other is zero range Skyrme interaction. Both of them are very successful interactions to investigate the bulk properties within the frame work of the Hartree-Fock approach. Another type of the mean field formalism is based on the relativistic theory and is of extensive interest because, it does not require spin orbital interaction terms unlike non-relativistic approaches. As nucleon-nucleon interaction is very important for

the interpretation of nuclear shapes and structure, one of the method to describe such interaction is to employ the optical model using a multi-parameter potential. For the estimation of these parameters of potential, one needs a large data of reaction observables (i.e total interaction cross sections, reaction cross sections, differential elastic scattering cross sections and momentum distributions, polarizations *etc.*). Another method to describe such interaction is via semi-classical approximation. These approximations relate the reaction cross sections with the transparency of the nucleus [3]. For the success of above mentioned models, one needs precise data on reaction dynamics for addressal of nuclear behavior over wide range of incident energies. In other words, matter distribution in a nucleus is a basic quantity for nuclear reaction models and one needs to handle it with utmost care.

The reaction cross sections at intermediate energies reflect the geometrical size of the nucleus. The enhancement in the values of reaction cross section for nuclei near the drip line [4] has revived much interest in reference to the exploration of nuclear matter size. The extraction of matter size or nucleonic distribution is difficult to determine precisely through electron scattering, because such reactions involve strong interactions whose behavior is still not fully established. The optical limit approximation (OLA) in the Glauber theory [5] is one of the convenient tool for an estimation of the size of unstable nuclei [6]. The another treatment beyond the OLA is necessary for a qualitative analysis of the reaction cross sections [7–9] as well as the elastic scattering cross sections [10, 11], for loosely coupled nuclear systems such as halo nuclei, because breakup effects are not properly accounted with OLA. Although the calculation of physical observable in the Glauber theory by using microscopic wave function gives an estimation of above observable within OLA. The Galuber many body system formalism is capable of explaining the loosely bound systems. The detail description of the relativistic mean field theory along with the Glauber

formalisms and associated Skyrme based interactions is given below.

2.1 Skyrme-Hartree-Fock formalism

Skyrme Interactions

The Skyrme force is a zero-range, density and momentum dependent effective interaction, which requires a few parameters for the description of bulk as well as single-particle properties of nuclear systems from light to super-heavy region. Although the quantities like binding energies, matter radii, electromagnetic form factors, giant resonance excitations, fission and fusion barriers *etc.* have been well described by this interaction, but there are still some limitations of Skyrme forces such as spin properties. The spin-orbit force, which is necessary in case of proper magic nuclei, requires an extra parameter which needs to be introduced externally for the better description. In other words spin couplings are largely undetermined because the Skyrme force is a non-relativistic model, and spin properties enter via relativistic effects. The basic idea of the Skyrme interaction for nuclear structure calculations is to develop an energy functional, which could be expressed in terms of zero-range expansion, leading to a simple derivation of Hartree-Fock equations. The energy functional contains two parts named as the direct and exchange terms having similar mathematical structure. The Skyrme effective interaction that leads to a two-body density-dependent interaction models the strong force in the Particle-hole channel and contains central, spin-orbit and tensor contributions in coordinate space known in standard analytical form as [1, 2, 12]:

$$\begin{aligned} V(r_1, r_2) &= t_0(1 + x_0 P_\sigma)\delta(\overrightarrow{r}) \\ &\quad + \frac{1}{2} t_1(1 + x_1 P_\sigma)[\overrightarrow{P'}^2 \delta(\overrightarrow{r}) + \delta(\overrightarrow{r})\overrightarrow{P}^2] \\ &\quad + t_2(1 + x_2 P_\sigma)\overrightarrow{P'}.\delta(\overrightarrow{r})\overrightarrow{P} \\ &\quad + \frac{1}{6} t_3(1 + x_3 P_\sigma)[\rho(\overrightarrow{R})]^\sigma \delta(\overrightarrow{r}) \\ &\quad + \iota W_0 \sigma.[\overrightarrow{P'} \times \delta(\overrightarrow{r})\overrightarrow{P}]. \end{aligned} \tag{2.1}$$

where $\overrightarrow{r}=\overrightarrow{r}_1-\overrightarrow{r}_2$ and $\overrightarrow{R}=\frac{1}{2}(\overrightarrow{r}_1+\overrightarrow{r}_2)$, are the center of mass and relative coordinate respectively. Here the operator $\overrightarrow{P}$ may be defined as $\overrightarrow{P}=\frac{1}{2\iota}(\overrightarrow{\nabla}_1-\overrightarrow{\nabla}_2)$, and σ spin operator is expressed as $\sigma=\sigma_1+\sigma_2$ and $P_\sigma=(1+\sigma_1.\sigma_2)/2$

Hamiltonian density functional

The general form of the Skyrme effective interaction used in the mean-field model can be expressed as a density functional $\mathcal{H}$ [1,2], which is a function of some empirical parameters, such as

$$\mathcal{H}=\mathcal{K}+\mathcal{H}_0+\mathcal{H}_3+\mathcal{H}_{eff}+.....,\tag{2.2}$$

where $\mathcal{K}=\frac{\hbar^2}{2m}\tau$, $\mathcal{H}_0$, $\mathcal{H}_3$ and $\mathcal{H}_{eff}$ are the kinetic energy, zero range, density dependent and the effective mass dependent terms, respectively.

$$\mathcal{H}_0=\frac{1}{4}t_0[(2+x_0)\rho^2-(2x_0+1)(\rho_p^2+\rho_n^2)],\tag{2.3}$$

$$\mathcal{H}_3=\frac{1}{24}t_3\rho^\eta[(2+x_3)\rho^2-(2x_3+1)(\rho_p^2+\rho_n^2)]and\tag{2.4}$$

$$\begin{aligned}\mathcal{H}_{eff} &= \frac{1}{8}[t_1(2+x_1)+t_2(2+x_2)]\tau\rho+\frac{1}{8}[t_2(2x_2+1)\\ &\quad -t_1(2x_1+1)](\tau_p\rho_p+\tau_n\rho_n).\end{aligned}\tag{2.5}$$

The kinetic energy term $\mathcal{K}$ is used in the fermi gas model for non-interacting fermions. The other terms representing the surface contributions of finite nucleus with b_4 and $\acute{b}_4$ as additional parameters are

$$\begin{aligned}\mathcal{H}_{s\rho} &= \frac{1}{16}[3t_1(1+\frac{1}{2}x_1)-t_2(1+\frac{1}{2}x_2)](\overrightarrow{\nabla}\rho)^2\\ &\quad -\frac{1}{16}[3t_1(x_1+\frac{1}{2})+t_2(x_2+\frac{1}{2})]\\ &\quad \times[(\overrightarrow{\nabla}\rho_n)^2+(\overrightarrow{\nabla}\rho_p)^2],\end{aligned}\tag{2.6}$$

and

$$\mathcal{H}_{s\overrightarrow{J}} = -\frac{1}{2}[b_4\rho\overrightarrow{\nabla}.\overrightarrow{J} + \acute{b}_4(\rho_n\overrightarrow{\nabla}.\overrightarrow{J_n} + \rho_p\overrightarrow{\nabla}.\overrightarrow{J_p})], \tag{2.7}$$

where $\rho = \rho_n + \rho_p$ is the total nucleon density, the kinetic energy density $\tau = \tau_n + \tau_p$ and the spin-orbit density $\overrightarrow{J} = \overrightarrow{J}_n + \overrightarrow{J}_p$. Here n and p are the subscripts representing the neutron and proton, and m be the mass of nucleon. $\overrightarrow{J}_q = 0$, $q = n$ or p for spin saturated nuclei, i.e, for nuclei with major oscillator shells completely field. These terms are dependent on different parameters termed as x_0, x_1, x_2, x_3, t_0, t_1 ,t_2, t_3 and η.

Total binding energy and densities expressions

The total binding energy (B.E.) of the nucleus is obtained by integrating the density functional $\mathcal{H}$ as in the form:

$$\langle\Psi|H|\Psi\rangle = \int \mathcal{H}(r)d^3r, \tag{2.8}$$

where the expression of total density "ρ_q(r)", kinetic density "τ_q(r)" and spin density "J_q(r)" of nucleus are expressed as:

$$\rho_q(r) = \sum_{i,s} |\phi_i^q(r,s)|^2 n_i^q, \tag{2.9}$$

$$\tau_q(r) = \sum_{i,s} |\nabla\phi_i^q(r,s)|^2 n_i^q, \tag{2.10}$$

$$J_q(r) = \sum_{i,s,s'} \phi_i^q(r,s')\nabla\phi_i^q(r,s) \times \langle s'|\sigma|s\rangle n_i^q, \tag{2.11}$$

here $\phi_i^q(r,s)$ is the single-particle wave function with orbital, spin and isospin quantum numbers , i, s and q respectively, and n_i^q is the occupation number of corresponding state i, s, q. ϕ_i is the single-particle wave function with orbital, spin and isospin quantum number.

Table 2.1 The sets of Skyrme parameters used in the non-relativistic mean field formalism

Parameters	t_0	t_1	t_2	t_3	x_0	x_1	x_2	x_3	α
SkI4	-1855.8	473.8	1006.9	9703	0.41	-2.89	-1.33	1.15	0.25
SLy4	-2488.9	486.8	-546.4	13777	0.83	-0.34	-1.00	1.35	0.17
Nuclear	Matter	Properties							
	$M*_s$	a_{sym}	K(MeV)	$\rho_o(fm^{-3})$	BE/A				
SkI4	0.65	29.54	248.4	0.160	15.94				
SLy4	0.69	32.04	230.04	0.160	15.97				

Parameters of Skyrme interaction

Numerous parameters are used to exhibit the role of Skyrme interactions [13], which are generally designed via consideration of experimental data for both finite nuclei and saturation properties of infinite nuclear matter [2, 14–17]. The choice of force parameter is most important for the accuracy of results. We have used the Skyrme SkI4 parameter set with $b_4 \neq b'_4$ [17] in our calculations. This parameter gathers special interest because of addressal of reasonable spin-orbit interaction in finite nuclei, that relates isotope shifts in Pb region. The force parameters of SkI4 along with SLy4 forces are presented in the Table 2.1.

Simple effective interaction

As both zero range Skyrme and finite range Gogny interactions are well exercised to estimate the bulk properties of nuclei, these interactions are very different as per their basic assumptions and still reasonably successful in the Hartree-Fock formalism. Another kind of interaction, simple effective interaction (SEI) which is hybrid of Gogny and Skyrme interactions, is also used to exhibit nuclear dynamical behavior. This interaction was recently used to study the bulk properties of finite nuclei within the frame work of Hartree-Fock (HF) formalism. The description of such interaction (SEI) is given in Ref's [18, 19]. The testing of estimated densities using Hartree-Fock with this simple effective interaction

in reaction dynamics is of huge interest and is being exercised in recent times. Although the non-relativistic theory is a standard tool for the investigation of the bulk properties of the finite as well as the infinite nuclear matter but the relativistic mean field has several advantages over the non-relativistic mean field theory. The relevant details of the relativistic mean field theory are discussed in the subsequent section.

2.2 Relativistic mean field formalism

One of the advantages of the relativistic mean field theory is that the nuclear saturation, which is achieved without any extra density dependence and spin-orbit interaction appears in the formalism without any extra adjustment of parameters. Beside this, a reasonable agreement in the nuclear shapes has been obtained for ^{16}O to ^{208}Pb isotopes, by including Coulomb force and iso-vector meson field. The remarkable agreement has been achieved for binding energies and nuclear compressibility by including nonlinear self-couplings of the scalar field [20–22]. The studies on nucleon-nucleus scattering by a relativistic optical potential at a mean-field level [23] also support the inclusion of spin and polarization properties naturally. This relativistic treatment is also used beyond the mean field in a Brueckner-Hartree-Fock model. The binding energy and the saturation density of nuclear matter are quite accurately approximated by relativistic many body analysis [24, 25].
The microscopic description of ground state properties of finite nuclei has been attempted by using nuclear many-body field theory. Relativistic mean field theory starts from an effective Lagrangian containing the nucleonic and the mesonic degree of freedom. This is a phenomenological theory of the nuclear many-body problem, which is based on four basic assumptions: (i) the nucleons are treated as point-like particles, (ii) these particles obey strictly the rules of relativity and causality, (iii) the theory is fully Lorentz invariant and

(iv) the particles move independently in the mean fields which originate from nucleon-nucleon interactions. These conditions impose that the interaction is mediated via an exchange of point-like effective mesons, which couple to the nucleons at local vertices. Under these assumptions, the nucleons are treated as Dirac particles and are described by Dirac spinor ψ. The point like particles are called mesons ϕ_j, where j stands for σ, ω, ρ and photon fields. They are characterized by their quantum numbers, masses (m_j) and coupling constants (g's). The number of mesons, their masses, coupling constants and quantum numbers such as spin (J), parity (P) and isospin (I) are determined in such a way so as the experimental data be reasonably reproduced. The mesons are treated as the classical fields. Their dynamics is determined through a Lagrangian density $\mathcal{L}(\phi,\partial_\mu\phi,t)$ and the variational principle;

$$\delta \int dtL = \delta \int d^4x \mathcal{L}(\phi, \partial_\mu \phi, t) = 0, \tag{2.12}$$

which on the classical level gives the Euler-Lagrange equation of motion:

$$\partial_\mu (\frac{\partial \mathcal{L}}{\partial(\partial_\mu \phi_j)}) - \frac{\mathcal{L}}{\partial \phi_j} = 0. \tag{2.13}$$

The energy momentum tensor [26] is given by

$$T^{\mu\nu} = -g^{\mu\nu}\mathcal{L} + \frac{\partial \mathcal{L}}{\partial(\partial_\mu \phi_j)} \partial^\nu \phi_j. \tag{2.14}$$

The Euler-Lagrange equation ensures that this quantity is conserved. The continuity equation is

$$\partial_\mu T^{\mu\nu} = 0. \tag{2.15}$$

If $\mathcal{L}$ has no explicit space dependance then the four-momentum, defined by

$$P^{\nu} = \int d^3 r T^{0\nu}, \tag{2.16}$$

is conserved. The energy is the zeroth component of the four-momentum

$$P^0 = E = \int d^3 r \mathcal{H}(r). \tag{2.17}$$

The Hamiltonian density is:

$$\mathcal{H}(r) = T^{00} = \frac{\partial \mathcal{L}}{\partial q_j}\phi_j - \mathcal{L}. \tag{2.18}$$

Thus, the total binding energy 'E' of the nucleus is given by

$$E = \int d^3 r \mathcal{H}(r) = \int T^{00} d^3 r. \tag{2.19}$$

In principle, there are many possible mesons which are characterized by the quantum numbers J, P and I. The well known $\pi-$meson carries the quantum numbers J=0, I=1 and P=-1. Since the $\pi-$meson carries the negative parity, the corresponding mean field breaks on Hartree level and its contribution is zero. This is certainly not the case in real nuclei, where the mean field follows the parity conversion to a very high degree of accuracy *i.e.* assumed to be of well defined parity. Therefore the effect of $\pi-$mesons averages essentially to zero in the description of bulk properties of nuclei [26, 27]. Also, the ground state has well defined charge, and thus the expectation values for charged $\rho-$field operators gets vanished. To include the $\pi-$meason, we have to go beyond the mean field. Two or any even number of pions, however contribute to the positive parity fields; therefore one may include the phenomenological $\sigma-$meson. The charge independent and spin dependent character of nuclear forces is described by the different mesons. The exchange of $\sigma-$meson which is a resonance state of 2π (s-wave) leads to an attractive nuclear force among the nucleons, and the corresponding field works as scalar field σ(r).

Table 2.2 The degree of freedom, quantum numbers and the nature of interactions of different mesons.

Deg. of freedom	Mass(MeV)	Spin J^P	Isospin (I, I_z)	Charge	Type of force
n(nucleon)	939.0	1/2	1/2;-1/2	0	free
p(nucleon)	939.0	1/2	1/2;-1/2	1	free
σ(scalar)	520	0^+	0,0	0	attractive and spin-orbit
ω(vector)	783.0	1^-	0,0	0	repulsive, tensor and spin-orbit
ρ(vector)	770.0	1^-	1	0	tensor
γ(photon)	0	1	0,0	0	Coulomb repulsive and tensor
π	139.0	0^-	1;$\pm$1,0	$\pm$1,0	not included

The repulsive nuclear force comes into play due to the exchange of vector meson ($3\pi-$ resonance state) which generates ω^μ(r) field, whose time like component is responsible for a repulsive force. The isospin dependence of the nuclear force is taken care by the exchange of $\rho-$mesons. In fact, pion would carry the isospin, but as contribution of the pion on Hartree level is zero, therefore, the $\rho-$field (2π-resonance, p-state) takes care of this aspect phenomenologically. The electromagnetic field of photon is described by the vector potential A^μ(r) and its time-like component represents Coulomb repulsion. A more detailed specification about the degree of freedom is shown in the table 2.2. The $\rho-$mesons have the same quark composition as that of π, but the mass is about $5\frac{1}{2}$ times the $\pi-$mesons; therefore, $\rho-$mesons are considered to be the excited state of $\pi-$meson.

Lagrangian density functional

The relativistic mean field approach is well documented in Refs. [22, 27–30]. The basic ingredient of the RMF model is the relativistic Lagrangian density functional for a nucleon-meson many body system which is defined as [29]

$$\begin{aligned}\mathcal{L} &= \overline{\psi}_i(i\gamma^\mu\partial_\mu - M)\psi_i + \frac{1}{2}\partial^\mu\sigma\partial_\mu\sigma - \frac{1}{2}m_\sigma^2\sigma^2 - \frac{1}{3}g_2\sigma^3 - \frac{1}{4}g_3\sigma^4 - g_s\overline{\psi}_i\psi_i\sigma \\ &\quad -\frac{1}{4}\Omega^{\mu\nu}\Omega_{\mu\nu} + \frac{1}{2}m_w^2V^\mu V_\mu - g_\omega\overline{\psi}_i\gamma^\mu\psi_iV_\mu - \frac{1}{4}\vec{B}^{\mu\nu}.\vec{B}_{\mu\nu} + \frac{1}{2}m_\rho^2\vec{R}^\mu.\vec{R}_\mu \\ &\quad -g_\rho\overline{\psi}_i\gamma^\mu\overrightarrow{\tau}\psi_i.\overrightarrow{R^\mu} - \frac{1}{4}F^{\mu\nu}F_{\mu\nu} - e\overline{\psi}_i\gamma^\mu\frac{(1-\tau_{3i})}{2}\psi_iA_\mu. \qquad (2.20)\end{aligned}$$

Here σ, V_μ and $\overrightarrow{R}_\mu$ are the fields for σ-, ω- and ρ-mesons respectively. A^μ is the electromagnetic field. The ψ_i are the Dirac spinors for the nucleons whose third component of isospin is denoted by τ_{3i}. g_s, g_ω, g_ρ and $\frac{e^2}{4\pi}=\frac{1}{137}$ are the coupling constants for the linear term of σ-, ω- and ρ-mesons and photons respectively. g_2 and g_3 are the parameters for the non-linear terms of the σ-meson. M, m_σ, m_ω and m_ρ are the masses of the nucleons, σ-, ω- and ρ-mesons, respectively. $\Omega^{\mu\nu}$, $\overrightarrow{B}^{\mu\nu}$ and $F^{\mu\nu}$ are the field tensors for the V^μ, $\overrightarrow{R}^\mu$ and the photon fields, respectively. The quadrupole moment deformation parameter β_2, root mean square radii and binding energy are evaluated using the standard relations [28]. By using the nonlinear σ potential the bulk modulus was found close to its empirical value. The tensor field of vector mesons and electromagnetic field are defined as

$$\overrightarrow{B}^{\mu\nu} = \partial^\mu \overrightarrow{\rho}^\nu - \partial^\nu \overrightarrow{\rho}^\mu - g_\rho(\overrightarrow{R}^\mu \times \overrightarrow{R}^\nu), \tag{2.21}$$

$$\Omega^{\mu\nu} = \partial^\mu V^\nu - \partial^\nu V^\mu, \tag{2.22}$$

$$F^{\mu\nu} = \partial^\mu A^\nu - \partial^\nu A^\mu. \tag{2.23}$$

The ground state properties are estimated using the static solution of the above Lagrangian. Here meson and electromagnetic fields are time independent, whereas the nucleon wave functions oscillate with single-particle energy 'E_i'. Due to time-reversal symmetry the vector potential 'V', density 'ρ' and electromagnetic potential 'A' gets vanished. The charge conservation implies that only the third component of isovector vector field ρ_0 contributes towards the nucleonic interaction. The Dirac Hamiltonian for the finite nuclei can be written as [31, 32]

$$\begin{aligned}\mathcal{H}(\mathbf{r}) = -i\boldsymbol{\alpha}\cdot\boldsymbol{\nabla} + W(r) + \frac{1}{2}\tau_3 R + \beta(M - \Phi(r)) \\ + \frac{1+\tau_3}{2}A(r) - \frac{i}{2M}\beta\boldsymbol{\alpha}\cdot\left(f_v\boldsymbol{\nabla}W + \frac{1}{2}f_\rho\tau_3\boldsymbol{\nabla}R + \right) \\ + \frac{1}{2M^2}\left(\beta_s + \beta_v\tau_3\right)\Delta A - \frac{i}{2M}\lambda\beta\boldsymbol{\alpha}\cdot\nabla A,\end{aligned} \tag{2.24}$$

where $W(r) \equiv g_v V_0(\mathbf{r})$, $\Phi(r) \equiv g_s \phi_0(\mathbf{r})$, $R \equiv g_\rho b_0(\mathbf{r})$ and $A \equiv eA_0(\mathbf{r})$ are the scalar mean fields with couplings [33]. $\beta = \gamma_0$ and $\alpha = \gamma_0\ \gamma$ are the Dirac matrices. The terms with g_γ, λ, β_s and β_v take care of the effects related with the electromagnetic structure of the pion and the nucleon (see Ref. [31]). Specifically, the constant g_γ concerns the coupling of the photon to the pions and the nucleons, through the exchange of neutral vector mesons. The experimental value is $g_\gamma^2/4\pi = 2.0$. The constant λ is required to reproduce the magnetic moments of the nucleons, defined by

$$\lambda = \frac{1}{2}\lambda_p(1+\tau_3) + \frac{1}{2}\lambda_n(1-\tau_3), \tag{2.25}$$

with $\lambda_p = 1.793$ and $\lambda_n = -1.913$, the anomalous magnetic moments of the proton and the neutron, respectively. The terms with β_s and β_v contribute to the charge radii of the nucleon [31]. The Dirac equation with single particle Hamiltonian h_α, the eigenvalues E_α and eigen functions $\psi_\alpha(r)$ is [26, 34]

$$h_\alpha \psi_\alpha(r) = E_\alpha \psi_\alpha(r), \tag{2.26}$$

with the normalization condition,

$$\int d^3 r \psi_\alpha^\dagger(r)\psi_\alpha(r) = 1. \tag{2.27}$$

The eigen functions for the spherically symmetric nuclei is given by

$$\psi_\alpha(r) = \psi_{nkmt} = \begin{pmatrix} \frac{i}{r}G_a(r)\phi_{km} \\ -\frac{1}{r}F_a(r)\phi_{-km} \end{pmatrix}, \tag{2.28}$$

where G and F are the upper and the lower component of the wave function $\psi_\alpha(r)$ respectively. Moreover, ϕ_{km} is a spin harmonic term, t = 1/2 for protons and t = -1/2 for

neutrons. The radial equations for G and F become,

$$(\frac{d}{dr}+\frac{k}{r})G_a(r)-[E_a-U_1(r)+U_2(r)]F_a(r)-U_3G_(r)=0, \tag{2.29}$$

$$(\frac{d}{dr}-\frac{k}{r})F_a(r)+[E_a-U_1(r)-U_2(r)]G_a(r)+U_3F_a(r)=0, \tag{2.30}$$

where $U_1(r)$, $U_2(r)$, $U_3(r)$, are the single particle potentials and they are defined as

$$U_1(r)=W(r)+t_aR(r)+(t_a+\frac{1}{2})A(r)+\frac{1}{2M^2}(\beta_s+2t_a\beta_v)\nabla^2A(r), \tag{2.31}$$

$$U_2(r)=M-\phi(r), \tag{2.32}$$

$$U_3(r)=\frac{1}{2M}\left\{f_vW'(r)+t_af_\rho R'(r)+A'(r)[(\lambda_p+\lambda_n)/2+t_a(\lambda_p-\lambda_n)]\right\}, \tag{2.33}$$

here the prime denotes a radial derivative. The mean field equations for ϕ, W, R and A are given by

$$\begin{aligned}-\nabla^2\phi+m_s^2\phi=g_s^2\rho_s(r)-\left(\frac{\kappa_3}{2}+\frac{\kappa_4}{3!}\frac{\Phi}{M}\right)\frac{m_s^2\Phi^2}{M}+\frac{\eta_\rho}{2M}\frac{g_s^2}{g_\rho^2}m_\rho^2R^2+\frac{\alpha_2}{2M}\frac{g_s^2}{g_v^2}(\nabla W)^2\\+\frac{g_s^2}{2M}\left(\eta_1+\eta_2\frac{\phi}{M}\right)\frac{m_v^2}{g_v^2}W^2+\frac{\alpha_1}{2M}[(\nabla\phi)^2+2\phi\nabla^2\phi],\end{aligned} \tag{2.34}$$

$$\begin{aligned}-\nabla^2W+m_v^2W=g_v^2\left(\rho_s(r)+\frac{f_v}{2}\rho_T(r)\right)-\frac{\phi}{M}m_v^2W\left(\eta_1+\frac{\eta_2}{2}\frac{\phi}{M}\right)\\-\frac{1}{3!}\zeta_0W^3+\frac{\alpha_2}{M}\left(\nabla\phi\cdot\nabla W+\phi\nabla^2W\right),\end{aligned} \tag{2.35}$$

$$-\nabla^2 R + m_\rho^2 R = \frac{1}{2} g_\rho^2 \left(\rho_3(r) + \frac{f_\rho}{2} \rho_{T,3}(r) \right) - \eta_\rho \frac{\phi}{M} m_\rho^2 R, \tag{2.36}$$

$$-\nabla^2 A = e^2 \rho_p(r). \tag{2.37}$$

Numerical Method

To find solutions of the RMF equations, we use the finite basis expansion method [35] in which an axially deformed harmonic oscillator basis is used. The upper and the lower components of the Dirac spinor and boson fields are expanded separately in this appropriate basis with an initial deformation. Here we truncate the basis after a finite value of oscillator quantum number N_{max} (N_F and N_B, 'F' stands for fermion and 'B' stands for boson), which is the quantum number of the major oscillator shell. In axial symmetry, the densities are invariant with respect to a rotation around the symmetry axis (z-axis) but the rotational symmetry is broken; therefore, j is no longer a good quantum number. It is thus useful to use cylindrical co-ordinates:

$$x = r_{xy} cos\phi, \quad y = r_{xy} sin\phi \quad and \quad z. \tag{2.38}$$

The spinor ψ_i is characterized by the quantum numbers: Ω_i, P_i, t_i. Where $\Omega_i = m_{t_i} + m_{si}$ is the eigen value of symmetry operator J_P, P_i is parity and t_i is isospin. The spinor can be written in the form given by

$$\psi_i(r,t) = \begin{pmatrix} f_i(r) \\ i g_i(r) \end{pmatrix} = \frac{1}{\sqrt{2\pi}} \begin{pmatrix} f_i^+(z,r) \exp i(\Omega_i - 1/2)\phi(r) \\ f_i^-(z,r) \exp i(\Omega_i + 1/2)\phi(r) \\ i g_i^+(z,r) \exp i(\Omega_i - 1/2)\phi(r) \\ i g_i^-(z,r) \exp i(\Omega_i + 1/2)\phi(r) \end{pmatrix}. \tag{2.39}$$

We expand spinors $\mathrm{f}_i^{\pm}$ and $\mathrm{g}_i^{\pm}$ in the above equation in terms of the eigen functions of a deformed axially symmetric oscillator potential:

$$V_{osc}(z, r_\perp) = \frac{1}{2}M\omega_z^2 z^2 + \frac{1}{2}M\omega_\perp^2 r_\perp^2. \tag{2.40}$$

Taking the volume conservation into account, the two oscillator frequencies $\hbar\omega_\perp$ and $\hbar\omega_z$ can be expressed in terms of a deformation parameter β_0:

$$\hbar\omega_z = \hbar\omega_0 \exp(-\sqrt{\frac{5}{4\pi}}\beta_0) \tag{2.41}$$

$$\hbar\omega_\perp = \hbar\omega_0 \exp(+\frac{1}{2}\sqrt{\frac{5}{4\pi}}\beta_0). \tag{2.42}$$

The corresponding oscillator length parameters are:

$$b_z = \sqrt{\frac{\hbar}{M\omega_z}} \quad and \quad b_\perp = \sqrt{\frac{\hbar}{M\omega_\perp}}. \tag{2.43}$$

For the volume conservation, we have $b_\perp^2 b_z = b_0^3$. The four components $f^{\pm}(r,z)$ and $g^{\pm}(r,z)$ obey Dirac equation:

$$(M^* + V)f_i^+ + \partial_i g_z^+ + \left(\partial_r + \frac{\Omega+\frac{1}{2}}{r} \right) g_i^- = \epsilon f_i^+ \tag{2.44}$$

$$(M^* + V)f_i^- - \partial_i g_z^+ + \left(\partial_r - \frac{\Omega+\frac{1}{2}}{r} \right) g_i^- = \epsilon f_i^- \tag{2.45}$$

$$(M^* + V)g_i^+ + \partial_i g_z^+ + \left(\partial_r + \frac{\Omega-\frac{1}{2}}{r} \right) g_i^- = -\epsilon f_i^+ \tag{2.46}$$

$$(M^* + V)g_i^- + \partial_i g_z^+ + \left(\partial_r - \frac{\Omega+\frac{1}{2}}{r} \right) g_i^- = -\epsilon g_i^-. \tag{2.47}$$

The densities now become:

$$\rho_{s,v} = 2\sum_{i>0} v_i^2\{(|f_i^+|^2 + |f_i^-|^2) \mp (|g_i^+|^2 + |g_i^-|^2)\} \tag{2.48}$$

$$\rho_{3,c} = 2\sum_{i>0} v_i^2\{(|f_i^+|^2 + |f_i^-|^2) + (|g_i^+|^2 + |g_i^-|^2)\}. \tag{2.49}$$

These densities serve as sources for the fields ϕ=σ, ω, ρ and photon, which are determined by meson equations in the cylindrical co-ordinates:

$$(-\frac{1}{r_\perp}\partial r_\perp r_\perp \partial r_\perp - \partial_z^2 + m_\phi^2)\phi(z, r_\perp) = s_\phi(z, r_\perp), \tag{2.50}$$

with the inhomogeneous part s_ϕ

$$s_\phi = \begin{cases} -g_\sigma \rho_s(z, r_\perp) - g_2\sigma^2(z, r_\perp) - g_3\sigma^3(z, r_\perp) \\ g_\omega \rho_v(z, r_\perp) - C_3 V^3(z, r_\perp) \\ g_\rho \rho_3(z, r_\perp) \\ e\rho_p(z, r_\perp) \end{cases} \tag{2.51}$$

The iteration procedure to solve RMF equations is as follows: (i) in the beginning we assume the values of meson fields V and S, (ii) using these fields we solve the Dirac equation for spinors ψ_i, then various densities (2.49) and (2.50) are calculated using the spinors (2.40) which in turn give the source terms (2.52) in the meson equations, (iii) the solution of meson equations are used to calculate the potentials and effective mass M*. These new potentials and M* are further used in the Dirac equation for the next iteration. This process continues till the convergence is achieved to the desired accuracy. Thus, the self-consistent solution of RMF equations yields the nucleon spinors (ψ_i), meson and electromagnetic fields (σ, ω, ρ, A), total binding energy (E), single-particle energies, point-

neutron and proton densities *etc.* Finally, the total binding energy (E_{total}) is calculated by summing the contribution of energy, mesons and photon energies,

$$E_{tot} = E_{part} + E_{\sigma} + E_{\omega} + E_{\rho} + E_{pair} + E_{C.M} + E_c \tag{2.52}$$

whereas the different energy expressions of equation (2.53) are given below:

$$\begin{aligned}
E_{part} &= \sum_{i=1}^{A} v_i^2 \int d^3r \psi_i^{\dagger}\{-i\vec{\alpha}.\vec{\nabla} + \beta M^* + V\}\psi_i \\
&= \sum_{i}^{A} v_i^2 \epsilon_i \\
E_{\sigma} &= \int d^3r \{\frac{1}{2}(\nabla\sigma)^2 + U\sigma\} \\
E_{\omega} &= -\int d^3r \frac{1}{2}\{(\nabla V_0)^2 + m_{\omega}^2 V_0^2\} \\
E_{\rho} &= -\int d^3r \frac{1}{2}\{(\nabla \rho_0)^2 + m_{\rho}^2 \rho_0^2\} \\
E_c &= -\int d^3r \frac{1}{2}(\nabla A_0)^2 \\
E_{CM} &= -\frac{3}{4}\hbar\omega_0 = -\frac{3}{4}41A^{-\frac{1}{3}} \\
E_{pair} &= -G(\sum_{i=1}^{A} u_i v_i)^2.
\end{aligned} \tag{2.53}$$

From these quantities one can calculate point-neutron/proton radii ($r_{n/p}$), charge radii r_c, charge densities ρ_c, nucleon separation energies, quadrupole moments and deformation parameter (β_2) *etc.*. The radii $r_{n/p}$ are calculated using the expression:

$$\langle r_{n/p}^2 \rangle = \sum_{i=1}^{N(Z)} n_i \overline{\psi}_i(r) r^2 \psi_i(r). \tag{2.54}$$

The root mean square radius is given by

$$r_{rms} = \left(\frac{N r_n^2 + Z r_p^2}{N+Z}\right). \tag{2.55}$$

The charge radius is given by

$$r_c = \sqrt{r_p^2 + 0.64}, \tag{2.56}$$

where the size of proton is taken to be 0.8 fm. The charge densities are obtained by folding the calculated point proton densities with proton charge distribution. The proton charge distribution is taken to be a Gaussian. The folded densities are:

$$\rho_c(r) = \int d^3r\prime \frac{1}{\sqrt{(2\pi\sigma)^3}} exp(-\frac{(r-r\prime)^2}{2\sigma^2})\rho_p(r\prime). \tag{2.57}$$

The quadrupole moments $Q_{n/p}$ for neutrons/protons are calculated by using the following operator expressions:

$$Q_{n/p} = \langle 2r^2 P_2(cos\theta)\rangle = \langle 2z^2 - x^2 - y^2\rangle_{n/p}. \tag{2.58}$$

The deformation parameter β_2 is calculated from the quadrupole moment for neutron/proton using the relation:

$$Q = Q_n + Q_p = \sqrt{\frac{16\pi}{5}} \frac{3}{4\pi} A R_0^2 \beta_2. \tag{2.59}$$

The neutron (S_n, S_{2n}) and proton (S_p, S_{2p}) separation energies are calculated by using the expression:

$$S_n = B.E.(N,Z) - B.E.(N-1,Z) \qquad S_p = B.E.(N,Z) - B.E.(N,Z-1) \tag{2.60}$$

$$S_{2n} = B.E.(N,Z) - B.E.(N-2,Z) \qquad S_{2p} = B.E.(N,Z) - B.E.(N,Z-2) \tag{2.61}$$

The set of used parameters of NL3, NL-SH [36] and NL3* [37] forces in RMF formalism

Table 2.3 The sets of different parameters used in relativistic mean field formalism. The nuclear properties and empirical (Emp.) values are also given.

Parameters	NL-SH	NL3	NL3*	Emp. Value
M(MeV)	939.000	939.000	939.000	938.00
m_σ	526.059	508.194	502.574	
m_ω	783.000	782.501	782.600	738±5
m_ρ	763.000	763.000	763.000	773±77
g_σ	10.444	10.217	10.094	
g_ω	12.945	12.868	12.807	
g_{rho}	4.383	4.575	4.575	
g_2	-6.910	-10.431	-10.809	
g_3	-15.834	-28.885	-30.149	
Nuclear	Matter	Properties		
$M*_s$/M	0.600	0.600	0.594	0.65
a_{sym}(MeV)	36.1	37.4	38.6	36.1
K(MeV)	355.36	271.76	258.28	210±30
$\rho_o(fm^{-3})$	0.146	0.148	0.150	0.17
BE/A(MeV)	16.35	16.30	16.31	15.68

are given in Table 2.3 along with their nuclear matter properties.

2.2.1 BCS Pairing Correlation

Certainly, pairing plays a crucial role for the open shell nuclei in determining the nuclear properties. The constant gap, BCS-approach is reasonably valid for the nuclei in the valley of β-stability line. The well known pairing energy expression is written as

$$E_{pair} = -G\left[\sum_{i>0} u_i v_i\right]^2, \tag{2.62}$$

with G=pairing force constant, v_i^2 and $u_i^2 = 1 - v_i^2$ are the occupation probabilities [38–40]. The variational approach with respect to v_i^2 gives the BCS equation

$$2\epsilon_i u_i v_i - \triangle(u_i^2 - v_i^2) = 0, \tag{2.63}$$

using $\triangle = G\sum_{i>0} u_i v_i$. The occupation number is defined as

$$n_i = v_i^2 = \frac{1}{2}\left[1 - \frac{\epsilon_i - \lambda}{\sqrt{(\epsilon_i - \lambda)^2 + \triangle^2}}\right]. \tag{2.64}$$

The constant gaps for proton and neutron read as [41, 42]:

$$\triangle_p = RB_s e^{sI-tI^2}/Z^{1/3} \tag{2.65}$$

and

$$\triangle_n = RB_s e^{-sI-tI^2}/A^{1/3}, \tag{2.66}$$

with $R = 5.72$, $s = 0.118$, $t = 8.12$, B_s=1, and $I = (N - Z)/(N + Z)$. This is to be noted that the gaps obtained by these expressions are valid for nuclei both on or away from the stability line. Using these gap parameters, we calculate directly the occupation probability. The chemical potentials λ_n and λ_p are determined by the particle numbers for the protons and the neutrons. The pairing energy is computed as $E_{pair} = -\triangle \sum_{i>0} u_i v_i$. For a particular value of $\triangle$ and G, the pairing energy E_{pair} diverges if it is extended to an infinite configuration space. In fact, in all the realistic calculations with finite range forces, $\triangle$ decreases with state for large momenta near the Fermi surface. In the present case, we assume equal pairing gap for all the states $\mid \alpha >= \mid nljm >$ near the Fermi surface. We use a pairing window, where the equations are extended up to the level $\epsilon_i - \lambda \leq 2(41A^{1/3})$. The factor 2 is used so as to reproduce the pairing correlation energy for neutrons in ^{118}Sn using Gogny force [28, 39]. Within this pairing approach, it is shown that the results for binding energies and quadrupole deformations are almost identical with the predictions of relativistic Hartree-Bogoliubov (RHB) approach.

2.3 Density conversion

The SHF and RMF equations of a motion obtained from equation's (2.2) and (2.20) are solved self-consistently in an axially deformed coordinate. The obtained densities are in

ω and z directions. We arrange the density as a function of ω and ρ for a constant value of z, which is the distribution of the nucleons perpendicular to the symmetry axis. Again, for a particular ω, we re-arrange the density along the parallel direction of symmetry axis as a function of z. From simple geometric consideration, we have used the relation $r = \sqrt{x^2 + y^2 + z^2}$, with $\omega = \sqrt{x^2 + y^2}$ to get the spherical equivalent density as a function of r only. It is important to note that the obtained density does not change within this process, but the ω and z values combine together for a particular density to produce an average r. This spherical equivalent $\rho(r)$ can be used like a one dimensional density in our subsequent calculations. But we can not use the densities of the relativistic and the non-relativistic mean field directly in the Glauber model. Since we need to convert these densities in terms of Gaussian form, the spherical equivalent densities obtained from the axially deformed RMF and SHF formalisms are fitted with the Gaussian function to find out the coefficients c_i and a_i defined as:

$$\rho(r) = \sum_{i=1}^{n} c_i exp[-a_i r^2], \tag{2.67}$$

These coefficients are important for the evaluation of total nuclear reaction cross-sections and the other reaction observable.

2.4 Glauber Model

The heavy ion collision is one of the interesting area, because the nucleus-nucleus collision may produce thousands of particles during head-on collision, which inturn exhibit very complex behavior as compared to a nucleon-nucleon interaction. It is also relevant to see dependence on nuclear shapes, impact parameter (b), number of participating nucleons, or binary nucleon-nucleon collisions during the reactions. The theoretical techniques have

been developed to estimate various reaction cross section parameters using experimental observables based on a multiple scattering of the nucleon-nucleon interaction, and one such method is termed as Glauber model [5, 6, 43, 44]. Glauber pioneered the quantum-mechanical scattering theory for composite nuclear systems, which describes nontrivial properties of the proton-nucleus and the nucleus-nucleus collisions by employing various cross section parameters. This model also provides a quantitative addressal of the geometrical configuration of colliding nuclear systems. The basic assumption of this theory is based on minimal mean free path. Due to this assumption, during nucleon-nucleon collision the reaction cross-section remains constant and follows a straight line trajectory. Therefore Glauber model has been designed to simulate the heavy ion collision, which helps to an estimation of a number of participating nucleons in the particle production process and the number of binary collisions among the nucleons for the projectile and the target nuclei. The Glauber model can be studied with two successful approaches "Optical limit" [44]and "Monte Carlo eikonal" [45, 46] approximation.

In the optical limit approximation, overall phase shift function of the incoming wave is evaluated via sum of all possible phase shifts functions of the projectile and the target nuclei and the imaginary part this phase shift function is related to the nucleon-nucleon scattering cross-section through the optical theorem which is based on following assumptions: i) at high energies, nucleons carries sufficiently high momentum so as to pass undetected through each other. ii) the nucleons move in the nucleus independently. iii) the size of the nucleus is much larger than the extent of the nucleon-nucleon force. These hypotheses of linear independent trajectories of constituent nucleons make it possible to develop an analytic relationship between the number of interacting nucleons and the number of nucleon-nucleon collisions in terms of a basic nucleon-nucleon cross-section and the impact parameter of the nucleus-nucleus collision.

Another approach is based on Monte Carlo eikonal approximation in which the nucleus-nucleus collision has been considered as a sequence of an independent nucleon-nucleon collision. The Monte Carlo approach is used here for the determination of the geometric quantities in the heavy ion collisions such as impact parameter, number of participating nucleons and number of binary collisions in the initial state *etc.*. This technique is a closer simulation to the experimental conditions because of the following merits: i) the two colliding nuclei are assembled by positioning the nucleons randomly in a three dimensional coordinate system, event by event, in accordance to the given nuclear density distribution. ii) two nucleons are considered to collide if their distance "d" in the plane orthogonal to the beam direction satisfies equation $\pi d^2 = \sigma_{inel}^{NN}$, where σ_{inel}^{NN} is the total inelastic nucleon-nucleon cross-section. iii) the number of participating nucleons and the number of binary collisions in a nuclear collision can be simply counted and averaged over multiple events. The above theories of Glauber assumptions are based on standard models [5, 43, 47–49], which estimate nucleus-nucleus interaction in terms of nucleon-nucleon interaction for a given density distribution of projectile and target nuclear systems. One can find the description of the eikonal approximation in Ref's [48, 49]. Whereas in optical limit approximation the main geometrical parameters are nucleonic densities of projectile and target nuclei, along with some inelastic nucleon-nucleon cross section. The single particle wave function has been used in the OLA. The phase shift function has been estimated by the sum of wave functions of all the possible nucleon-nucleon wave functions. The detail description of Glauber models are given in the subsections discussed below.

2.4.1 Total reaction cross section

The theoretical formalism to study the reaction cross sections using the Glauber approach was given by R. J. Glauber [43]. This formalism is wildly used for reaction dynamics and

improved for exotic nuclear systems [45, 46, 50]. The standard Glauber form for total reaction cross sections is expressed as stated in [6, 43, 45, 46]

$$\sigma_R = 2\pi \int_0^\infty \overrightarrow{b}[1 - T(\overrightarrow{b})]d\overrightarrow{b}, \tag{2.68}$$

where 'T($\overrightarrow{b}$)' is the Transparency function with impact parameter '$\overrightarrow{b}$'. The function T($\overrightarrow{b}$) is calculated by

$$T(\overrightarrow{b}) = exp[-\sum_{i,j} \sigma_{NN} \int \overline{\rho}_{Pi}(\overrightarrow{s})\overline{\rho}_{Tj}(|\overrightarrow{b} - \overrightarrow{s}|)d\overrightarrow{s}]. \tag{2.69}$$

Here, the summation runs over nucleons i, j, where i belongs to the projectile and j belongs to the target nuclei. The subscript 'P' and 'T' refers to projectile and target respectively. σ_{NN} is the experimental nucleon-nucleon reaction cross-section which depends on the energy.

This Glauber approach agrees well with the experimental data at high energies and fails to describe the collisions induced at relatively low energies. This disagreement is due to the Coulomb repulsive potential which plays a significant role, whose effects are obvious in the low-energy range. Such a Coulomb effect breaks the characteristic Glauber assumption that the projectile travels along straight-line trajectories. Several attempts have been made to include the Coulomb effect into the Glauber formalism [51–56]. The most successful approach, based on the WKB approximation for the phase shifts, replaces the impact parameter $\overrightarrow{b}$ in the transparency function T($\overrightarrow{b}$) by the distance $\overrightarrow{b_c}$ of the closest approach of the deviated projectile trajectory due to the Coulomb effect. Therefore, by substituting the transparency function T($\overrightarrow{b}'$) for T($\overrightarrow{b}$) in equation 2.21 with $\overrightarrow{b}'(\overrightarrow{b})$, being the classical distance of the closest approach, the reaction cross-section can be expressed [55, 57]. The parameter $\acute{b}$ corresponds to the distance of closest approach along

the Coulomb trajectory, and is related to the impact parameter b according to [52, 53]

$$\acute{b} = b_c = \frac{1}{k}(\eta + \sqrt{\eta^2 + k^2 b^2}) \tag{2.70}$$

and

$$\eta = \frac{Z_P Z_T e^2}{\hbar v}. \tag{2.71}$$

Here 'k' is a projectile wave number and 'η' is a Sommerfeld parameter, whereas the relative velocity between the two nuclei is 'v'. Initially the Glauber model was designed for the high energy approximation. However it was found to work reasonably well for both the nucleus-nucleus reaction and the differential elastic cross-sections over a broad energy range [44, 58]. The modified transparency function T($\overrightarrow{b}$) is given by

$$T(\overrightarrow{b}) = exp[-\int_p \int_t \sum_{i,j} [\Gamma_{NN}(b)] \overline{\rho}_{Pi}(\overrightarrow{t}) \overline{\rho}_{Tj}(\overrightarrow{s}) d\overrightarrow{s} d\overrightarrow{t}], \tag{2.72}$$

$$\Gamma_{NN}(b) = \frac{1 - \iota\alpha_{NN}}{2\pi\beta_{NN}^2} \bar{\sigma}_{NN} exp(-\frac{b^2}{2\beta_{NN}^2}), \tag{2.73}$$

Here $\bar{\sigma}_{NN}$ is the total reaction cross section of nucleon-nucleon collision, α_{NN} is the ratio of the real to the imaginary part of the forward nucleon-nucleon scattering amplitude and β_{NN} is the slope parameter. The slope parameter determines the fall of the angular distribution of the nucleon-nucleon elastic scattering. The value of nucleon-nucleon cross section ($\bar{\sigma}_{NN}$) is estimated by the expression [54, 57]

$$\bar{\sigma}_{NN} = \frac{N_p N_t \sigma_{nn} + Z_p Z_t \sigma_{pp} + N_p Z_t \sigma_{np} + N_t Z_p \sigma_{np}}{A_p A_t} \tag{2.74}$$

where A_p, A_n, Z_p, Z_n, N_p and N_n are the mass number, charge number and neutron number of the projectile and the target nuclei. The value of range parameter β_{NN} as a function of projectile energy 'E' can be estimated from [59, 60] as

$$\beta_{NN} = 0.99exp[\frac{-E}{106.679}] + 0.089. \tag{2.75}$$

2.4.2 Two body Glauber model

As discussed earlier the Glauber model is a microscopic model of high-energy collision based on either OLA or eikonal approximation and on the bare nucleonnucleon interaction. This is a standard tool for the estimation of various cross sections, because it can account for significant part of breakup effects, which play an important role in the reaction of weakly bound nucleus [7, 10]. However, these calculations require a very complicated multi-dimensional integration for the matrix element of multiple scattering operators. These integrations are usually reduced to a much simpler form by introducing the optical-limit approximation (OLA) [5, 6, 61]. This approximation, however, washes out nuclear correlations which are present in the wave function. Therefor, more elaborated treatment beyond the OLA is needed for the valence-nucleon part. The Monte Carlo quadrature with the Metropolis algorithm [62] has been employed for the solution of such calculations. This is a suitable tool for the reactions involving low density distribution or halo nucleus. A powerful application of the Monte Carlo integration to the Glauber analysis has very recently been demonstrated in Ref. [63]. The expression of the reaction cross section has been reduced to

$$\sigma_R = \int_0^\infty [1 - T(\overrightarrow{b})] d\overrightarrow{b}, \tag{2.76}$$

where $T(\overrightarrow{b})$ is the transparency function with an impact parameter $\overrightarrow{b}$. The function $T(\overrightarrow{b})$ can be expressed in term of a phase shift function by

$$T(\overrightarrow{b}) = |e^{\iota\chi_{PT}(\overrightarrow{b})}|^2. \tag{2.77}$$

Here, χ_{PT} is the projectile-target phase shift function. The phase shift function of the projectile-target nucleus requires the multidimensional integrations. The Monte Carlo technique has been used for the evaluation of a realistic wave function which contains nuclear correlation. The optical limit approximation (OLA) is used for the integration involving coordinates ($\overrightarrow{s}$, $\overrightarrow{t}$) of the projectile and the target nuclei. The phase shift function has been expressed for two body (core+neutron) projectile system as

$$\iota\chi_{PT}(\overrightarrow{b}) = \iota\chi_{CT}(\overrightarrow{b}) + \iota\chi_{NT}(\overrightarrow{b}), \tag{2.78}$$

where
$$\iota\chi_{CT}(\overrightarrow{b}) = -\int_p\int_t [\Gamma_{NN}(b_{eff})\overline{\rho}_P(\overrightarrow{t})\overline{\rho}_T(\overrightarrow{s})d\overrightarrow{s}\,d\overrightarrow{t}, \tag{2.79}$$

and

$$\iota\chi_{NT}(\overrightarrow{b}) = -\int_T [\Gamma_{NN}(|\overrightarrow{b} - \overrightarrow{s}|)\overline{\rho}_P(\overrightarrow{s})d\overrightarrow{s}, \tag{2.80}$$

Where $b_{eff} = |\overrightarrow{b} - \overrightarrow{s} + \overrightarrow{t}|$ is the impact parameter, however $\overrightarrow{s}$ and $\overrightarrow{t}$ are the dummy variables for integration over the z-integrated target and projectile densities. The profile function Γ_{NN} is defined for finite range as

$$\Gamma_{NN} = \Gamma_{ij}(b_{eff}) = \frac{1 - \iota\alpha_{NN}}{2\pi\beta_{NN}^2}\sigma_{NN}exp(-\frac{b_{eff}^2}{2\beta_{NN}^2}), \tag{2.81}$$

and, for zero range

$$\Gamma_{NN} = \Gamma_{ij}(b_{eff}) = \frac{1 - \iota\alpha_{NN}}{2}\sigma_{NN}\delta(b), \tag{2.82}$$

Here $\delta(b)$ is dirac delta function and parameters σ_{NN}, α_{NN} and β_{NN} usually depends upon the proton-proton, neutron-neutron and proton-neutron interactions as already discussed earlier. Where $\overline{\rho}_P$ and $\overline{\rho}_T$ are the densities of the projectile and the target nuclei. These

z-integrated densities are defined as

$$\overline{\rho}(\overrightarrow{\omega}) = \int_{-\infty}^{\infty} \rho(\sqrt{w^2 + z^2}) d\overrightarrow{z}, \tag{2.83}$$

with $\omega^2 = x^2 + y^2$. It is to be noted that these parameters are entirely independent which are used exclusively in the Glauber model and the input densities obtained from completely two different formalisms.

2.4.3 Angular elastic differential cross section

The nucleus-nucleus elastic scattering amplitude is written as [45, 46, 64]

$$F(\overrightarrow{q}) = \frac{\iota K}{2\pi} \int dbe^{\iota \overrightarrow{q}.\overrightarrow{b}} (1 - e^{\iota \chi_{PT}(\overrightarrow{b})}). \tag{2.84}$$

At low energy, this model is modified in order to address the finite range effects in the profile function and the Coulomb modified trajectories. The elastic scattering amplitude including the Coulomb interaction is expressed as

$$F(\overrightarrow{q}) = e^{\iota \chi_s} \{F_{coul}(\overrightarrow{q}) + \frac{\iota K}{2\pi} \int dbe^{\iota \overrightarrow{q}.\overrightarrow{b} + 2\iota\eta \ln(Kb)} (1 - e^{\iota \chi_{PT}(\overrightarrow{b})})\}, \tag{2.85}$$

with the Coulomb elastic scattering amplitude

$$F_{coul}(\overrightarrow{q}) = \frac{-2\eta K}{q^2} exp\{-2\iota\eta \ln(\frac{q}{2K}) + 2\iota arg\Gamma(1 + \iota\eta)\}, \tag{2.86}$$

where K is the momentum of a projectile and q is the momentum transferred from the projectile to the target. Here 'η' is the Sommerfeld parameter (See eq. 2.72), 'v' is the incident velocity of the projectile and $\chi_s = -2\eta \ln(2Ka)$, with 'a' being a screening

radius [5]. The elastic differential cross section is given by

$$\frac{d\sigma}{d\Omega} = |F(\overrightarrow{q})|^2, \tag{2.87}$$

and the ratio of the angular elastic to the Rutherford elastic differential cross section is expressed as

$$\frac{d\sigma}{d\sigma_R} = \frac{\frac{d\sigma}{d\Omega}}{\frac{d\sigma_R}{d\Omega}} = \frac{|F(\overrightarrow{q})|^2}{|F_{coul}(\overrightarrow{q})|^2}. \tag{2.88}$$

2.4.4 One nucleon removal cross section

The one nucleon removal cross section, σ_{-N}, may be defined as [45, 46, 65]

$$\sigma_{-N} = \Sigma_c \int d\overrightarrow{k}\, \sigma_{a=(\overrightarrow{k},g=0),c} \tag{2.89}$$

After interaction, the projectile nucleus breaks into the core with an internal wave function ϕ_g and one nucleon in a continuum state (c) with asymptotic momentum $\hbar\overrightarrow{k}$, relative to the core. With this assumption, the core always remains in its ground state (g=0) after interaction, the elastic and the inelastic components of one nucleon removal cross section are estimated by c=0 and c$\neq$0 respectively. Hence, one nucleon removal cross section consists of both the elastic and the inelastic parts which can be calculated by following expressions

$$\sigma_{-N} = \sigma_{-N}^{el} + \sigma_{-N}^{inel}. \tag{2.90}$$

The expression of the elastic cross section due to the elastic breakup process is given by

$$\begin{aligned} \sigma_{-N}^{el} &= \int d\overrightarrow{b}\, \{\langle\phi_0|e^{-2Im\chi_{CT}(\overrightarrow{b}_c)-2Im\chi_{NT}(\overrightarrow{b}_c+\overrightarrow{s})}|\phi_0\rangle \\ &\quad -|\langle\phi_0|e^{\iota\chi_{CT}(\overrightarrow{b}_c)+\iota\chi_{NT}(\overrightarrow{b}_c+\overrightarrow{s})}|\phi_0\rangle|^2\}. \end{aligned} \tag{2.91}$$

and that for inelastic component is expressed as

$$\begin{aligned}\sigma_{-N}^{inel} &= \int d\overrightarrow{b}\{\langle\phi_0|e^{-2Im\chi_{CT}(\overrightarrow{b}_c)} \\ &\quad -e^{-2Im\chi_{CT}(\overrightarrow{b}_c)-2Im\chi_{NT}(\overrightarrow{b}_c+\overrightarrow{s})}|\phi_0\rangle|\}. \end{aligned} \tag{2.92}$$

2.4.5 Longitudinal momentum distribution

The momentum distribution of a core fragment after the inelastic breakup of the projectile can be written as:

$$\frac{d\sigma_{-N}^{inel}}{d\overrightarrow{P}} = \int \frac{d\overrightarrow{q}}{K^2}\sum_{c\neq 0}\int d\overrightarrow{k}\,\delta(\overrightarrow{P} - \frac{A_C}{A_P}\hbar\overrightarrow{q} + \hbar\overrightarrow{k})|F_{(\overrightarrow{k},0)c}(\overrightarrow{q})|^2. \tag{2.93}$$

Where the momentum of the core is expressed as $P = (P_\parallel, \overrightarrow{P}_\perp)$ and the nucleon going to a continuum state be $\hbar\overrightarrow{k}$. Scattering amplitude for the reaction in the continuum state is $F_{(\overrightarrow{k},0)c}(\overrightarrow{q})$. The core-nucleon scattering wave function is approximated by a plane wave and we assume that the core remains in its ground state, which reduces the above expression as

$$\begin{aligned}\frac{d\sigma_{-N}^{inel}}{d\overrightarrow{P}} &= \int d\overrightarrow{b}_N(1 - e^{-2Im\chi_{NT}(\overrightarrow{b}_N)}) \times \frac{1}{(2\pi\hbar)^3}\frac{1}{2j+1} \\ &\quad \sum_{mm_s}|\int d\overrightarrow{r}\,e^{\frac{i}{\hbar}\overrightarrow{P}.\overrightarrow{r}}\chi_{\frac{1}{2}m_s}e^{i\chi_{CT}(\overrightarrow{b}_N-\overrightarrow{s})}\varphi_{nljm}(\overrightarrow{r})|^2, \end{aligned} \tag{2.94}$$

where $\overrightarrow{b}_N$ stands for the impact parameter of valence nucleon with respect to the target and $\varphi_{nljm}(\overrightarrow{r})$ is the wave function of valence nucleon which may expressed as

$$\varphi_{nljm}(\overrightarrow{r}) = u_{nlj}(r)\sum_{m_l m_s}\langle lm_l\frac{1}{2}m_s|jm\rangle Y_{lm_l}(\hat{r}')\chi_{\frac{1}{2}m_s}. \tag{2.95}$$

The longitudinal momentum distribution obtained by the integration over transverse component of momentum ($\overrightarrow{P}_{\perp}$), gives.

$$\begin{aligned}\frac{d\sigma_{-N}^{inel}}{dP_{||}} &= \int d\overrightarrow{P}_{\perp}\frac{d\sigma_{-N}^{inel}}{d\overrightarrow{P}} \\ &= \frac{1}{2\pi\hbar}\int d\overrightarrow{b}_N(1-e^{-2I_m\chi_{NT}(\overrightarrow{b}_N)})\int d\overrightarrow{s}e^{-2I_m\chi_{CT}(\overrightarrow{b}_N-\overrightarrow{s})} \\ &\quad\times\int dz\int dz' e^{\frac{\iota}{\hbar}P_{||}(z-z')}u^*_{nlj}(r')u_{nlj}(r)\frac{1}{4\pi}P_l(\hat{r}'.\hat{r}). \qquad (2.96)\end{aligned}$$

where $\overrightarrow{r}=(\overrightarrow{s},z)$ and $\overrightarrow{r}'=(\overrightarrow{s},z')$ and P_l is the Legendre Polynomial.

The results obtained by using above methodology of this chapter are discussed in the subsequent chapters.

Bibliography

[1] J. R. Stone and P. -G. Reinhard, Prog. Part. Nucl. Phys. **58**, 587 (2007).

[2] E. Chabanat, P. Bonche, P. Hansel, J. Meyer and R. Schaeffer, Nucl. Phys. A **627**, 710 (1997).

[3] H. A. Bethe, Phys. Rev. **57**, 1125 (1940).

[4] I. Tanihata *et al.*, Phys. Rev. Lett. **55**, 2676 (1985); Phys. Lett. B **160**, 380 (1985).

[5] R. J. Glauber, in Lecture on Theoretical Physics, edited by W. E. Brittin and L. C. Dunham Interscience, New York **1**, 315 (1959).

[6] P. J. Karol, Phys. Rev. C **11**, 1203 (1975).

[7] G. F. Bertsch, H. Esbensen and A. Sustich, Phys. Rev. C **42**, 758 (1990).

[8] Y. Ogawa, K. Yabana and Y. Suzuki, Nucl. Phys. A **543**, 722 (1992); Nucl. Phys. A **539**, 295 (1992).

[9] J. S. Al-Khalili and J. A. Tostevin, Phys. Rev. Lett. **76**, 3903 (1996); J. S. Al-Khalili, J. A. Tostevin and I. J. Thompson, Phys. Rev. C **54**, 1843 (1996).

[10] K. Yabana, Y. Ogawa and Y. Suzuki, Phys. Rev. C **45**, 2909 (1992).

[11] J. S. Al-Khalili, J. A. Tostevin and J. M. Brooke, Phys. Rev. C **55**, 1018(R) (1997).

[12] B. K. Agrawal, S. K. Dhiman and R. Kumar, Phys. Rev. C **73**, 034319 (2006).

[13] M. Dutra *et al.*, Phys. Rev. C **85**, 035201 (2012).

[14] S. K. Patra, C. L. Wu, C. R. Praharaj and R. K. Gupta, Nucl. Phys. A **651**, 117 (1991).

[15] E. Chabanat, P. Bonche, P. Hansel, J. Meyer and R. Schaeffer, Nucl. Phys. A **635**, 231 (1998).

[16] B. A. Brown, Phys. Rev. C **58**, 220 (1998).

[17] P. -G. Reinhard and H. Flocard, Nucl. Phys. A **584**, 467 (1995).

[18] B. Behera, X. Viñas, M. Bhuyan, T. R. Routray, B. K. Sharma and S. K. Patra, J. Phys. G: Nucl. Part. Phys. **40**, 095105 (2013).

[19] T. R. Routray, X. Viñas, S. K. Tripathy, M. bhuyan, S. K. Patra and B. Behera, J. Phys. Conf. Ser. **420**, 012114 (2013).

[20] A. Bouyssy, S. Marcos and Pham von Thieu, Nucl. Phys. A **422**, 541 (1984).

[21] P.-G. Reinhard, M. Rufa, J. Maruhn, W. Greiner and J. Friedrich, Z. Phys. A **323**, 13 (1986).

[22] J. Boguta and A. R. Bodmer, Nucl. Phys. A **292**, 413 (1977).

[23] L. G. Arnold, B. C. Clark, R. L. Mercer and P. Schwandt, Phys. Rev. C **23**, 1949 (1981).

[24] R. Brockmann and R. Machleidt, Phys. Lett. B **149**, 283 (1984).

[25] B. Ter Haar and R. Malfliet, Phys. Lett. B **172**, 10 (1986).

[26] B. D. Serot and J. D. Walecka, The Relativistic Nuclear ManyBody Problem, Advances in Nucl. Phys., J. W. Negele and Erich Vogt eds., **16**, Plenum Press, NY (1986).

[27] P. Ring, Prog. Part. Nucl. Phys. **37**, 193 (1996).

[28] W. Pannert, P. Ring and J. Boguta, Phys. Rev. Lett. **59**, 2420 (1987).

[29] S. K. Patra and C. R. Praharaj, Phys. Rev. C **44**, 2552 (1991).

[30] M. Del Estal, M. Centelles, X. Vinas and S. K. Patra, Phys. Rev. C **63**, 024314 (2001); Phys. Rev. C **63**, 044321 (2001).

[31] R. J. Furnstahl, B. D. Serot and H. B. Tang, Nucl. Phys. A **598**, 539 (1996).

[32] R. J. Furnstahl, H. B. Tang and B. D. Serot, Phys. Rev. C **52**, 1368 (1995).

[33] A. R. Bodmer, Nucl. Phys. A **526**, 703 (1991).

[34] C. J. Horowitz and B. D. Serot, Nucl. Phys. A **368**, 503 (1981).

[35] Y. K. Gambhir, P. Ring and A. Thimet, Ann. Phys. (N.Y.) **198**, 132 (1990).

[36] G. A. Lalazissis, J. Konig and P. Ring, Phys. Rev. C **55**, 540 (1997).

[37] G. A. Lalazissis, S. Karatzikos, R. Fossion, D. Pena Arteaga, A. V. Afanasjev and P. Ring, Phys. Lett. B **671**, 36 (2009).

[38] A. Shukla, B. K. Sharma, R. Chandra, P. Arumugam and S. K. Patra, Phys. Rev. C **76** 034601 (2007).

[39] S. K. Patra, Phys. Rev. C **48** 1449 (1993).

[40] M. A. Preston and R. K. Bhaduri, Structure of Nucleus, **Chap. 8**, 309 (Addison-Wesley Publishing Company, 1982).

[41] D. G. Madland and J. R. Nix, Nucl. Phys. A **476**, 1 (1981).

[42] P. Moller and J. R. Nix, Atom. Data and Nucl. Data Tables **39**, 213 (1988).

[43] R. J. Gauber, Phys. Rev. **100**, 242 (1955).

[44] J. Chauvin *et al.*, Phys. Rev. C **28**, 1970 (1983).

[45] B. Abu-Ibrahim, Y. Ogawa, Y. Suzuki and I. Tanihata, Comp. Phys. Comm. **151**, 369 (2003).

[46] B. Abu-Ibrahim, K. Fujimura and Y. Suzuki, Nucl. Phys. A **657**, 391 (1997).

[47] A. G. Sitenko, Ukr. Fiz. J. **4**, 152 (1959).

[48] L. D. Landau and E. M. Lifshitz, Quantum Mechanics (Non-relativistic theory) Pergamon Press (1965).

[49] L. I. Schiff., Quantum Mechanics (International Pure and Applied Physics Series) McGraw Hill Companies (1968).

[50] C. A. Bertulani and A. Gade, Comp. Phys. Comm. **175**, 372 (2006).

[51] S. K. Gupta and S. Kailas, Z. Phys. A **317**, 75 (1984).

[52] A. Vitturi and F. Zardi, Phys. Rev. C **36**, 1404 (1987).

[53] S. M. Lenzi, A. Vitturi and F. Zardi, Phys. Rev. C **40**, 2114 (1989).

[54] S. K. Charagi and S. K. Gupta, Phys. Rev. C **46**, 1982 (1992).

[55] A. Y. Abul-Magd and M. T. Alhinai, Nuovo Cimento A **110**, 1281 (1997).

[56] J. Y. Hostachy *et al.*, Nucl. Phys. A **490**, 441 (1988).

[57] S. K. Charagi and S. K. Gupta, Phys. Rev. C **41**, 4 (1990).

[58] M. Buenerd *et al.*, Nucl. Phys. A **424**, 313 (1984).

[59] A. Bhagwat and Y. K. Gambhir, Phys. Rev. C **73**, 054601 (2006).

[60] T. Zheng *et al.*, Nucl. Phys. **709**, 103 (2003).

[61] J. Hfner and M. C. Nemes, Phys. Rev. C **23**, 2538 (1981).

[62] N. Metropolis, A. Rosenbluth, M. Rosenbluth, A. Teller and E. Teller, J. Chem. Phys. **21**, 1087 (1953).

[63] K. Varga, S. C. Pieper, Y. Suzuki and R. B. Wiringa, Phys. Rev. C **66**, 034611 (2002).

[64] S. K. Patra, R. N. Panda, P. Arumugam and R. K. Gupta, Phys. Rev. C **80**, 064602 (2009).

[65] R. N. Panda and S. K. Patra, Int. J. Mod. Phys. E **20**, 2505 (2011).

Chapter 3

Structure properties of nuclei using relativistic and non relativistic mean field formalism

3.1 Introduction

The nuclear structure effects have been extensively studied in recent time because many anomalies have appeared in the shell structure due to a large value of neutron/proton ratio. The atomic nucleus is a very complex structure, which consists of strongly-interacting many-body quantum mechanical systems. It exhibits a variety of shapes (from spherical to super deformed) and various excitation modes are exercised to understand nuclear behavior. These excitations can be from single protons and neutrons to collective vibrations and rotations in the whole nucleus. The study of the nuclear structure is utilized to explain numerous features/patterns of a behavior emerging from the strong nuclear interaction between the nucleons in the nucleus. The most essential part of this study is the concept of nuclear shell structure, in which the nucleons occupy some quantized

energy levels within a potential, which was generated due to interactions from all other nucleons. The effective interactions and an interplay of these interactions among the central, spin-orbit, and tensor components may cause the shifting of effective single-particle energies relative to each other, towards the neutron excess side [1–3]. The change in the separation between a single particle orbital due to a change in nuclear forces at exotic regions, consequently reduces the energy gap between single particle orbital, and the new shell gaps may start appearing. The conventional magic numbers at N=20 and 28 disappear, and new magic numbers at N=14, 16, 32 and 34 seem to appear [4–10] in the neutron rich nuclei. Since the structure of the nuclei from stable to drip line region is measured via respective bulk properties like binding energy, root mean square radius, charge radius, quadruple deformation, densities distribution of the systems *etc.* Various other phenomenological formalism are also available to study such properties, But the mean field formalisms provide the most successful tool to investigate these properties. As non-relativistic and relativistic mean field formalism are capable of identifying these properties quite accurately, for stable as well as drip line region, so both the formalisms are well established and are extensively used to predict such nuclear properties, exhibiting a decent agreement with the available experimental data. In this chapter, the structural properties of the light mass nuclei have been studied using these mean field formalisms. The relevant details of the formalisms were given in previous Chapter 2.

3.2 Parameterizations

There are many parameter sets available for exploring the ground state properties of the stable and the unstable nuclei using relativistic mean field (RMF) and Skyrme Hartree Fock (SHF) formalisms. These models are reasonably successful to reproduce the ground

Table 3.1 The calculated observable are compared with the results of various parameter sets. We have used SkI4 and SLy4 for non relativistic Skyrme Hartree-Fock and NL3* and NL-SH relativistic mean field formalisms. The charge radius (r_c) is in fm and binding energy (B.E.) is in MeV.

Nucleus	Observables	RMF		SHF		
		NL3*	NL-SH	SkI4	SLy4	Expt.
^{12}C	B.E.	87.7	89.8	88.4	85.1	92.2
	r_{ch}	2.692	2.696	2.585	2.653	2.47
	β_2	0.004	0.068	0.001	0.002	
^{19}C	B.E.	117.1	117.1	114.5	112.8	116.2
	r_{ch}	2.613	2.597	2.709	2.756	
	β_2	0.354	0.367	0.414	0.347	
^{22}N	B.E.	143.3	143.6	139.2	139.3	140.1
	r_{ch}	2.678	2.655	2.752	2.815	
	β_2	0.005	0.015	0.061	0.013	
^{23}O	B.E.	166.4	167.1	163.0	161.8	174.1
	r_{ch}	2.744	2.719	2.795	2.871	
	β_2	0.001	0.009	0.009	0.003	

state properties of nuclei near the valley of β-stability as well as far away from the β-stability line. The NL3 parameter set seems to provide the most successful non-linear RMF force [11]. With the advancement of the experimental laboratories, new experimental data on the finite nuclei have been available which contains more reliable information about the neutron skin. The small problem observed for light Hg and Pb isotopes with NL3 set has been rectified by the improved NL3* set [12]. This force also provides excellent results for the collective properties of the vibrational and the rotational character. On the other hand, the non-relativistic SkI4 force is well known to account for the spin-orbit interaction in the finite nuclei and seems to provide the best overall agreement on both the isotopic shift and the ground state properties in Pb region [13]. The parameters b_4 and b'_4 are explicitly used to take care of a proper spin orbit interaction in the finite nuclei. The NL3* and SkI4 force parameters are well suited for the investigation of the exotic nuclei. To see the parameter dependence on the results, we have done the calculations for

some representative cases using NL-SH set [11] for RMF and SLy4 parametrization [14] for SHF densities. The results are listed in Table 3.1 for a comparison. In general, the results obtained with different force parameters are almost close to each other for both RMF and SHF, *i.e.* similar results with NL3* and NL-SH and SkI4 and SLy4 as shown in Table 3.1. The calculated results reflect the marginal effect of force parameters. Hence, we have NL3/NL3* and SkI4 for our future analysis in this chapter. As we know that Skyrme force is a zero range force, so one new force has been developed known as a simple effective interaction (SEI), which is a combination of Skyrme and Gogny interaction. We also intend to see the role of SEI in various structure and reaction dynamical problems. In addition to this, an attempt is made to estimate the structural properties by Hartree-Fock formalism using newly developed simple effective interaction (SEI) [15, 16].

3.3 Role of Fermionic and Bosonic model space

We have obtained the field equations for nucleons and mesons using the RMF Lagrangian. For the deformed case, these equations are solved by expanding the upper and the lower components of the Dirac spinners and the Boson fields in an axially deformed harmonic oscillator basis. A set of a coupled equations are solved numerically by a self-consistent iteration method taking different inputs of the initial deformation β_0 [17–20]. For spherical densities, we follow the numerical procedure of Refs. [21,22]. In our numerical calculations, we fix fermionic and bosonic model space to an optimal limit, which should take care of all the energy levels of the nucleus including the continuum. For this, we have taken ^{36}Si nucleus as the test case, which is the heaviest among the considered in the present work. The calculations are estimated with the fermionic and bosonic shells N_F=N_B=6 to 20 and the corresponding results of B.E., rms radii (r_n,r_p,r_m) and β_2 are shown in

Table 3.2 A comparison for different bosonic shell for ^{36}Si isotopes.

N_F=N_B	B.E.	r_n	r_p	r_c	β_2
6	287.18	3.341	3.061	3.164	0.14222
8	290.95	3.389	3.075	3.177	0.16793
10	291.49	3.414	3.078	3.181	0.18638
12	291.48	3.423	3.082	3.184	0.1935
14	291.43	3.429	3.083	3.185	0.19545
16	291.44	3.431	3.084	3.186	0.19673
18	281.44	3.432	3.084	3.186	0.19727
20	290.95	3.433	3.084	3.186	0.19747

Table 3.2. From the table, It is clear that the results do not change for N_F=N_B=10 or more. Therefore, in rest of our calculations, we have used 12 as the model space for both fermionic and bosonic shells. This type of test is consistent with the earlier works [23–26].

3.4 Nuclear bulk properties of Be-Ar isotopes

3.4.1 Binding Energy

One of the major parameter which is explored experimentally and theoretically for a broad range of nuclear isotopes is binding energy. Broadly speaking, binding energy is the energy required by a nuclear system to bind the nuclei together, and is responsible for the existence of a nucleus. This parameter also suggests the stability of the nuclear systems and the forces existing inside the nucleus. This in turn means that if the binding energy per nucleon is higher, the concerned nucleus is more stable. The binding energies of some of the light to medium mass nuclei is estimated with the help of non-relativistic and relativistic mean field formalisms. The calculated values of binding energies for light to medium mass region are listed in Tables 3.3, 3.4 and 3.5. For better description, these results are also plotted in Figures 3.1, 3.2 and 3.3. Table 3.3 and Fig. 3.1 consist

Table 3.3 The binding energies of $^{9-12}$Be, $^{12-15}$B, $^{12-22}$C, $^{20-23}$N, $^{20-24}$O and $^{23-29}$F isotopes, obtained from relativistic mean field and non-relativistic Hartree-Fock calculations are compared with experimental data wherever available. The values of B.E.'s are in MeV.

B.E. in MeV						
Nuclei	RMF(NL3) sph.	RMF(NL3) def.	RMF(NL3*) def.	HF(SEI-I) sph.	SHF(SkI4) def.	Expt. [27, 28]
^{9}Be	54.76	58.018	-	54.927	-	58.164±0.000
^{10}Be	63.49	64.855	-	65.302	-	64.970±0.000
^{11}Be	67.97	67.780	-	69.380	-	65.478±0.000
^{12}Be	73.61	71.378	-	73.190	-	68.649±0.004
^{12}B	82.85	82.176	-	82.172	-	79.575±0.001
^{13}B	88.84	88.842	-	88.250	-	84.453±0.001
^{14}B	91.88	89.874	-	89.256	-	85.423±0.021
^{15}B	93.64	92.593	-	90.162	-	88.194±0.022
^{12}C	88.23	91.349	89.7	88.422	88.4	92.160±1.700
^{13}C	96.31	98.098	-	97.489	-	97.108±0.000
^{14}C	104.38	106.929	-	105.829	-	105.284±0.000
^{15}C	108.66	108.477	-	108.846	-	106.502±0.000
^{16}C	113.45	111.874	-	111.642	-	110.752±0.003
^{17}C	116.40	114.083	-	114.248	-	111.486±0.017
^{18}C	118.79	116.842	-	116.709	-	115.670±0.030
^{19}C	119.91	119.511	117.1	119.015	114.5	116.242±0.100
^{20}C	122.54	119.736	118.5	121.154	115.4	119.18±0.200
^{21}C	-	-	120.4	-	116.3	119.15±0.4
^{22}C	-	-	122.9	-	118.2	120.736±0.5
^{20}N	139.37	136.772	-	139.487	-	134.184±0.055
^{21}N	142.59	141.475	139.9	143.095	136.2	138.768±0.100
^{22}N	145.55	143.948	143.3	146.205	139.2	140.052±0.200
^{23}N	148.17	147.864	146.8	148.765	142.4	141.726±0.300
^{20}O	152.71	151.585	151.8	154.043	149.5	151.36±0.100
^{21}O	157.95	156.944	156.9	159.645	154.1	158.928±0.100
^{22}O	164.18	163.192	162.0	164.758	159.1	166.496±0.100
^{23}O	168.32	167.227	166.4	169.040	163.0	174.064±0.100
^{24}O	171.87	171.665	170.3	172.508	166.8	181.632±0.100
^{23}F	176.75	175.378	175.9	177.956	173.4	175.283±0.100
^{24}F	182.06	180.162	181.0	183.433	178.0	179.11±0.100
^{25}F	186.90	185.221	185.5	186.026	182.6	183.375±0.100
^{26}F	191.76	187.928	188.3	188.890	184.8	184.158±0.100
^{27}F	195.00	191.245	190.8	191.507	187.4	186.246±0.200
^{28}F	-	-	193.6	-	189.5	185.836±0.500
^{29}F	-	-	196.5	-	192.2	187.079±0.600

of calculated values of binding energy (B.E.) of $^{9-12}$Be, $^{12-15}$B, $^{12-22}$C, $^{20-23}$N, $^{20-24}$O and $^{23-29}$F isotopes using sph. RMF(NL3), def. RMF(NL3), def. RMF(NL3*), sph. HF(SEI-I) and def. SHF(SkI4) formalisms along with the experimental data [27,28]. The calculated values of B.E. overestimate the experimental data for the considered set of isotopes of Be, B, C, N and F, whereas the reverse trend is seen for the case of O-isotopes. *i.e.* value of B.E. underestimate the data for $^{20-24}$O isotopes. The calculated value of B.E. of ^{12}C is 88.23, 91.349, 89.7, 88.422, 88.4 and 92.16 ± 1.7 MeV using sph. RMF(NL3), def RMF(NL3), def RMF(NL3*), HF(SEI-I), SHF(SkI4) and experimental value, respectively. Similarly the calculated values of B.E. of ^{20}C are 122.54, 119.736, 118.5,121.154, 115.4 and 119.18±0.2 MeV from sph. RMF(NL3), def. RMF(NL3), def. RMF(NL3*), HF(SEI-I), SHF(SkI4) and experimental values, respectively. Figure 3.1 clearly demonstrates that both the formalisms are capable of reproducing the B.E. of these light mass isotopes. The values of B.E. from both the formalisms slightly overestimate the data, except for O-isotopes. The comparison between spherical and deformed formalisms clearly shows that the estimated values of the results are slightly higher for the spherical formalisms as compared to that for the deformed formalism. For further clarifications, we have extended our calculation to some medium mass region. The experimental values of B.E. for these systems are also given in Table's 3.4, 3.5 for comparison [27,28]. These predicted results of our calculations for some medium mass region are given in Tables 3.4, 3.5 and Figure's 3.2 and 3.3 along with the experimental data.

The Figure 3.2 represents the B.E. for $^{28-32}$Ne, $^{27-35}$Na, $^{30-42}$Mg and $^{32-35}$Si isotopes for the same sets of parameters/formalisms as discussed in Fig. 3.1. It is clearly seen from this figure that the estimated values of B.E. are very close to the experimental values for the isotopes of Na, Mg and Si nuclei. Whereas, the value of B.E.'s are overestimated for Ne-isotopes somewhat similar to the case of O-isotopes in previous figure. Similarly

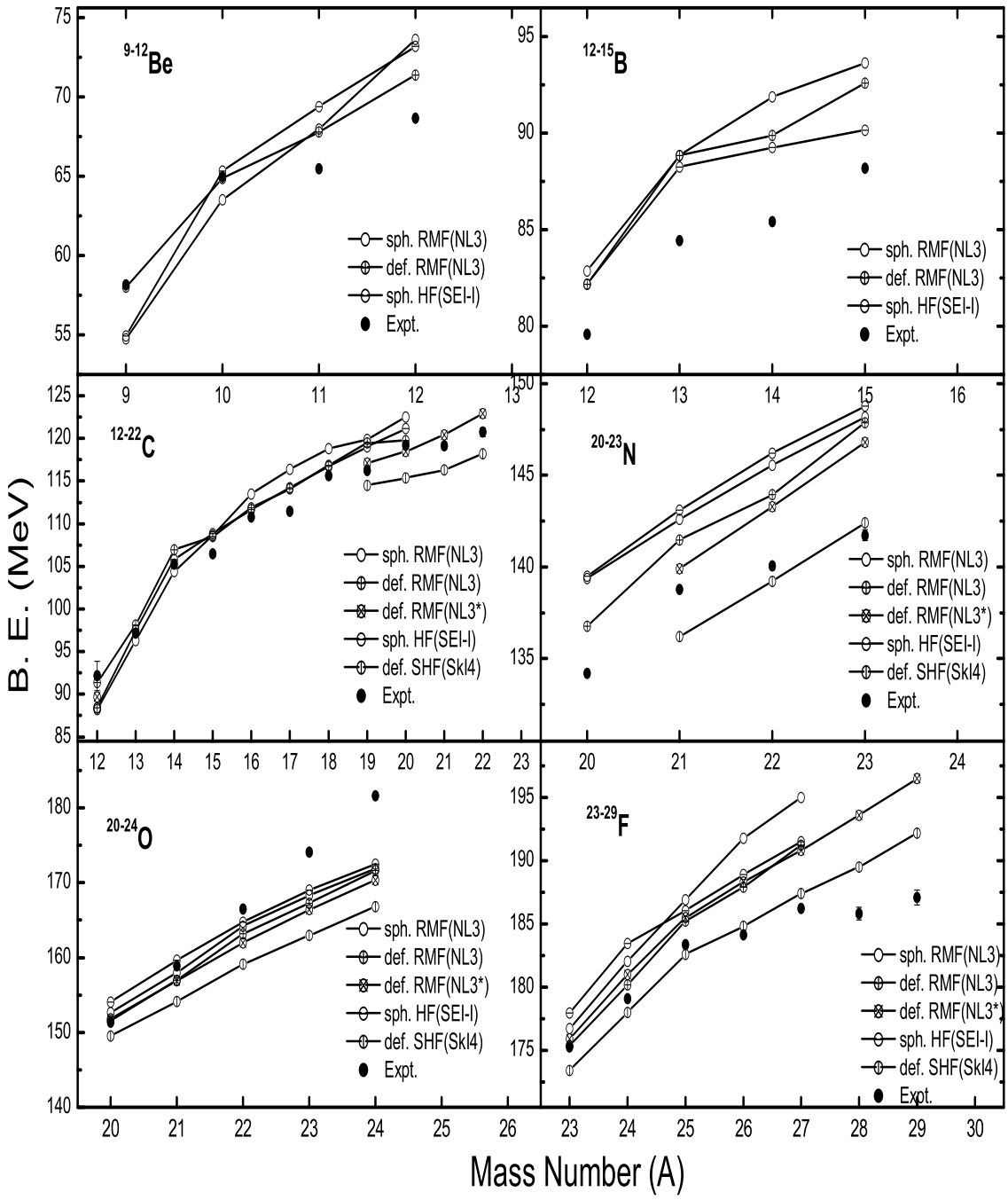

Figure 3.1 The comparison of binding energies in MeV for Be, B, C, N, O and F isotopes using sph. RMF(NL3), def. RMF(NL3), def. RMF(NL3*), sph. HF(SEI-I) and SHF(SkI4) formalism

Table 3.4 Same as Table 3.3, but for the isotopes of $^{28-32}$Ne, $^{27-35}$Na, $^{30-42}$Mg, and $^{32-35}$Si nuclei.

	B.E. in MeV					
Nuclei	RMF(NL3) Sph.	RMF(NL3) def.	RMF(NL3*) def.	HF(SEI-I) sph.	SHF(SkI4) def.	Expt. [27, 28]
^{28}Ne	210.62	208.122	207.7	207.273	205.9	206.89±0.100
^{29}Ne	214.35	211.140	211.0	210.833	208.3	207.843±0.100
^{30}Ne	218.02	214.920	214.7	214.160	211.9	211.29±0.300
^{31}Ne	221.97	215.812	214.8	214.569	212.0	211.42±0.200
^{32}Ne	223.95	218.409	217.1	214.860	213.4	213.472±0.500
^{27}Na	-	-	214.5	-	214.3	214.836±0.4
^{28}Na	-	-	219.7	-	218.7	218.380±0.1
^{29}Na	-	-	224.4	-	223.5	222.792±0.1
^{30}Na	-	-	228.5	-	227.0	225.150±0.2
^{31}Na	-	-	232.8	-	231.2	229.059±0.1
^{32}Na	-	-	234.1	-	232.2	230.880±0.1
^{33}Na	-	-	237.0	-	234.5	233.772±0.6
^{34}Na	-	-	239.0	-	235.6	234.532±0.5
^{35}Na	-	-	240.8	-	237.1	236.040±0.6
^{30}Mg	-	-	240.1	-	240.5	241.620±0.1
^{31}Mg	-	-	245.1	-	244.9	244.013±0.2
^{32}Mg	252.06	250.387	250.5	249.390	250.2	249.804±0.200
^{33}Mg	256.02	252.982	252.3	252.015	252.1	252.017±0.200
^{34}Mg	259.14	257.169	256.1	254.355	255.3	256.462±0.100
^{35}Mg	261.82	260.211	259.3	256.498	257.5	257.460±0.200
^{36}Mg	-	-	262.2	-	260.2	260.784±0.5
^{37}Mg	-	-	263.6	-	260.8	260.961±0.5
^{38}Mg	-	-	264.7	-	261.6	263.264±0.5
^{39}Mg	-	-	266.0	-	262.1	263.133±0.5
^{40}Mg	-	-	267.4	-	263.0	264.840±0.5
^{41}Mg	-	-	267.2	-	262.6	-
^{42}Mg	-	-	266.9	-	262.3	-
^{32}Si	267.69	268.203	-	267.928	-	271.407±0.000
^{33}Si	275.97	275.359	-	275.953	-	275.915±0.000
^{34}Si	283.78	278.249	-	283.470	-	283.428±0.014
^{35}Si	289.77	287.135	-	288.258	-	285.903±0.038

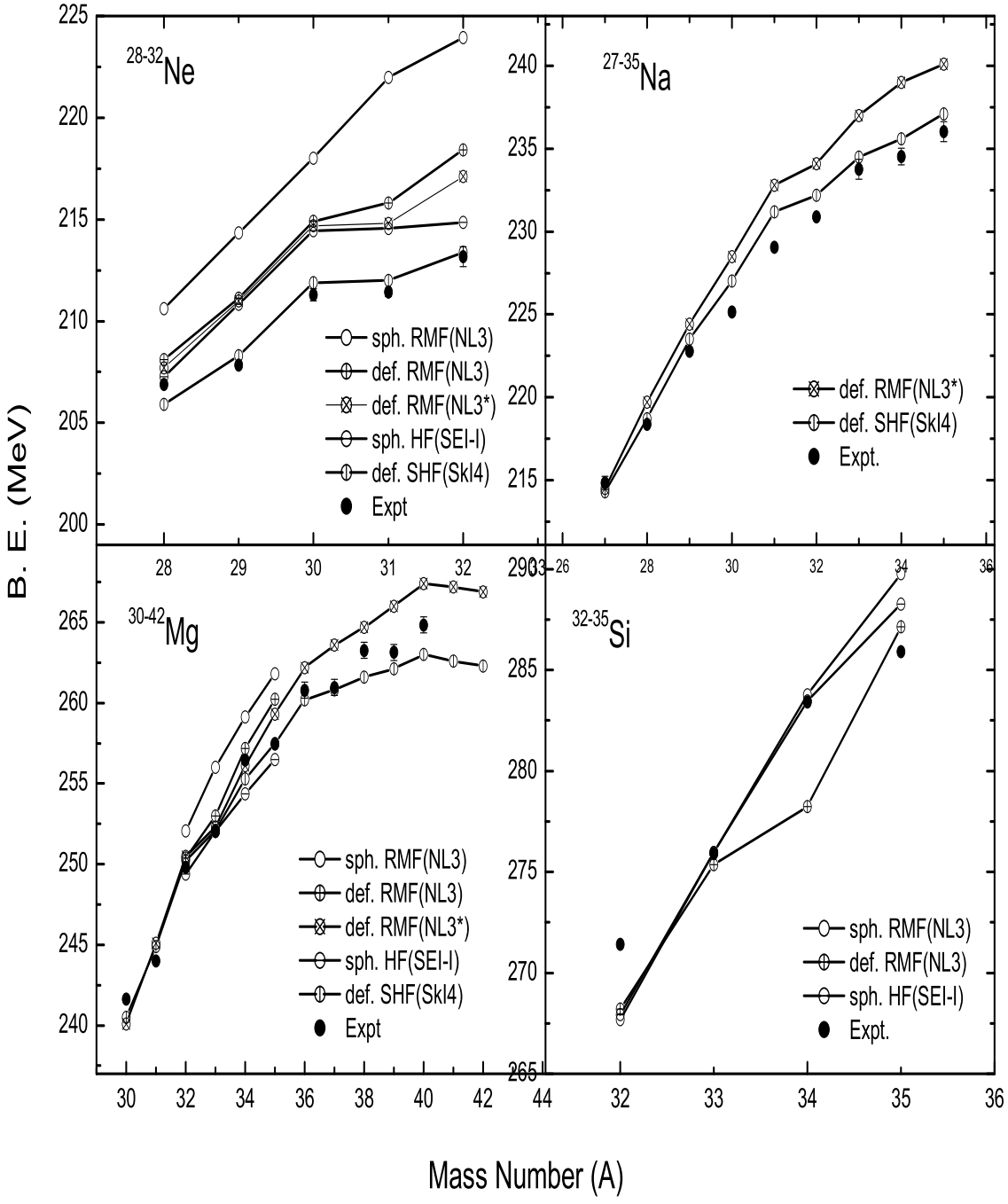

Figure 3.2 Same as figure 3.1, but for Ne, Na, Mg and Si isotopes.

Table 3.5 Same as Table 3.3, but for the isotopes of $^{34-37}$S, $^{33-43}$Al and $^{34-48}$Ar nuclei.

B.E. in MeV						
Nuclei	RMF(NL3) Sph.	RMF(NL3) def.	RMF(NL3*) def.	HF(SEI-I) sph.	SHF(SkI4) def.	Expt. [27, 28]
^{34}S	286.05	286.295	-	286.424	-	291.838±0.000
^{35}S	296.71	295.543	-	296.491	-	298.824±0.000
^{36}S	306.52	299.502	-	305.978	-	308.714±0.000
^{37}S	313.58	309.946	-	312.676	-	313.017±0.000
^{33}Al	-	-	267.8	-	268.6	264.594±0.7
^{34}Al	-	-	270.8	-	270.5	267.301±0.6
^{35}Al	-	-	273.6	-	273.8	272.545±0.7
^{36}Al	-	-	277.3	-	276.6	274.428±0.1
^{37}Al	-	-	280.6	-	279.7	278.647±0.1
^{38}Al	-	-	282.7	-	280.6	280.326±0.3
^{39}Al	-	-	284.5	-	281.9	283.608±0.6
^{40}Al	-	-	286.5	-	283.4	284.720±0.7
^{41}Al	-	-	288.7	-	285.2	286.877±0.8
^{42}Al	-	-	289.2	-	285.2	287.364±0.9
^{43}Al	-	-	289.4	-	285.3	288.487±0.9
^{44}Al	-	-	289.2	-	285.3	-
^{34}Ar	273.76	273.397	-	273.357	-	278.719±0.000
^{36}Ar	300.25	302.268	-	300.129	-	306.716±0.000
^{38}Ar	325.59	319.946	-	324.432	-	327.342±0.000
^{40}Ar	342.31	340.945	-	341.555	-	343.810±0.000
^{42}Ar	357.39	356.393	-	357.013	-	359.335±0.005
^{44}Ar	371.42	370.639	-	371.135	-	373.728±0.001
^{46}Ar	384.57	384.603	-	383.672	-	386.927±0.040
^{48}Ar	394.58	392.810	-	391.79	-	396±0.720

Fig. 3.3 and Table 3.5 represent the values of B.E. of $^{34-37}$S, $^{33-44}$Al and $^{34-48}$Ar nuclei. Fig. 3.3 also shows that the B.E.'s are match excellently with the experimental data for these set of nuclei. Therefore, we conclude from the above discussion that the mean field formalisms show an excellent comparison of B.E. for a medium mass region and reasonably nice results for the lighter mass region. The comparison of the calculated and the experimental values of the binding energies suggest that both the formalisms are capable to reproduce the B.E's of the isotopes from stable to drip line nuclei. In general, it

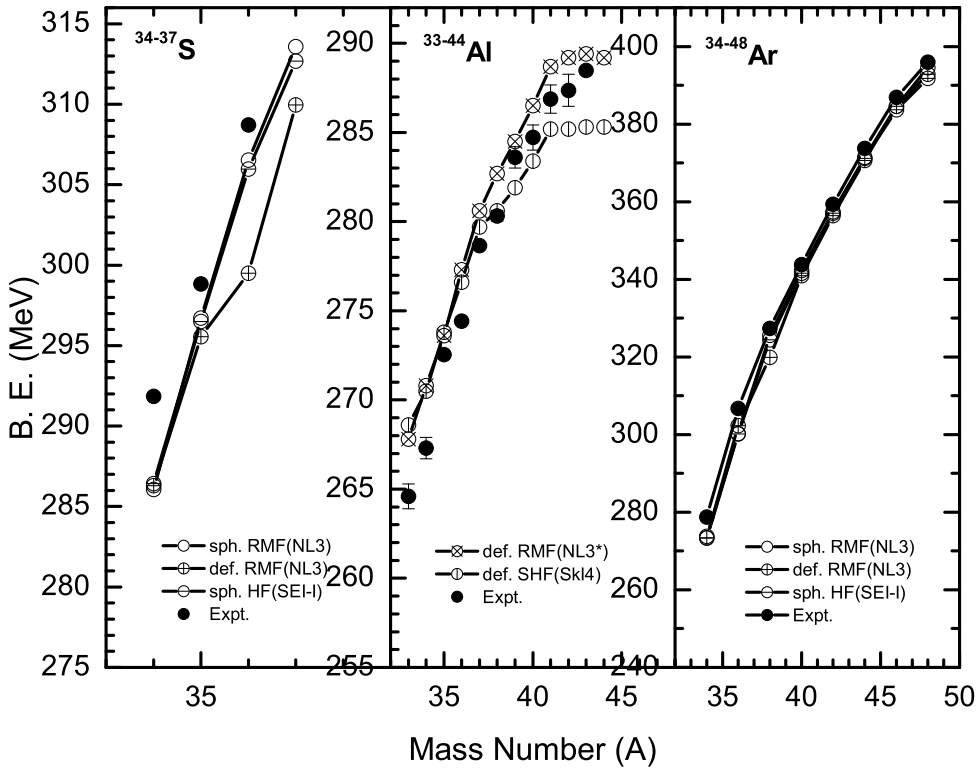

Figure 3.3 Same as figure 3.1, but for S, Al and Ar isotopes.

is clear from the Tables and Figures that, the error between the estimated values of B.E.'s and the experimental data are of very small (∼3 MeV) in comparison to B.E.'s values. A more careful comparison reveals that the RMF binding energies in most of the cases slightly overestimates the data contrary to the marginal under-estimation by the non-relativistic approach. The results obtained with both the spherical RMF and the spherical HF(SEI-I) formalism show slightly higher values than that for the deformed formalisms. The comparison of the experimental data with our results suggests that the RMF(NL3*) parameters show relatively better results when compared with both RMF(NL3) and HF formalism. In general, we find that both the formalisms are equally capable of reproducing the results of the binding energies from stable to drip line nuclei. For further insight we also intent to address other structure properties of nuclei like nuclear radii, quadrupole

deformation, nucleonic density distributions *etc.*

3.4.2 Nuclear radii

Another important parameter of the bulk properties is the root mean square radius. Tables 3.6, 3.7 and 3.8 show the calculated values of the nuclear charge radius r_c using spherical and deformed RMF(NL3), def. RMF (NL3*), HF(SEI-I) and SHF(SkI4) formalisms. An experimental data is also given for a comparison wherever available [29, 30]. Table 3.6 and Figure 3.4 show the values of charge radius (r_c) for $^{9-12}$Be, $^{12-15}$B, $^{12-22}$C, $^{20-23}$N, $^{20-24}$O and $^{23-29}$F isotopes as a function of the mass number. The figure clearly shows that the value of r_c is close to the available experimental values. The calculated values of charge radius are 2.364, 2.310, 2.692, 2.436, 2.583, 2.47 for ^{12}C from sph. RMF(NL3), def. RMF(NL3), def. RMF(NL3*), HF(SEI-I), SHF(SkI4) and experimental data respectively.

The observation from this figure suggests that the charge radius has higher values for sph. RMF(NL3) than the sph. HF(SEI-I), whereas a reverse trend has been observed in the case of deformed formalisms. The observation from these values and Tables 3.7 and 3.8 signify the utility of RMF and Hartree-Fock formalims by exhibiting a nice comparison with the available data. Similarly figures 3.5 and 3.6 represent the comparison of charge radius of $^{28-32}$Ne, $^{27-35}$Na, $^{30-42}$Mg, $^{32-35}$Si and $^{34-37}$S, $^{33-43}$Al, $^{34-48}$Ar isotopes with the experimental values in the respective figures. The value of r_c are 2.964, 2.966, 2.916, 2.892, 3.025, 2.963 for ^{28}Ne and 3.095, 3.091, 3,094, 3.032, 3.146, 3.186 for ^{32}Mg using sph RMF(NL3), def RMF(NL3), def RMF(NL3*), HF(SEI-I) and SHF(SkI4). These comparisons of the results shown in Fig 3.4-3.7, suggest that both the formalisms are very much appropriate to study the bulk properties of the light and the medium mass region from the stability to the drip-line nuclei. Hence one may conclude that the results of B.E. and r_c are reasonably good for the lighter mass region where one finds an excellent comparison with the data for medium mass regions.

Table 3.6 The charge radius (r_c) of $^{9-12}$Be, $^{12-15}$B, $^{12-22}$C, $^{20-23}$N, $^{20-24}$O and $^{23-29}$F isotopes, obtained from relativistic mean field and non-relativistic Hartree-Fock calculations. The experimental data are also given for comparison wherever available. The values of r_c are in fm.

r_c in fm						
Nuclei	RMF(NL3) sph.	RMF(NL3) def.	RMF(NL3*) def.	HF(SEI-I) sph.	SHF(SkI4) def.	Expt. [29,30]
^{9}Be	2.461	2.510	-	2.305	-	2.519
^{10}Be	2.537	2.423	-	2.302	-	2.36
^{11}Be	2.479	2.449	-	2.329	-	2.46
^{12}Be	2.549	2.450	-	2.353	-	-
^{12}B	2.498	2.457	-	2.393	-	-
^{13}B	2.540	2.492	-	2.411	-	-
^{14}B	2.534	2.522	-	2.423	-	-
^{15}B	2.532	2.564	-	2.435	-	2.511
^{12}C	2.364	2.310	2.692	2.436	2.585	2.47
^{13}C	2.459	2.466	-	2.454	-	2.46
^{14}C	2.504	2.517	-	2.470	-	2.56
^{15}C	2.516	2.535	-	2.480	-	-
^{16}C	2.531	2.565	-	2.489	-	-
^{17}C	2.542	2.582	-	2.500	-	-
^{18}C	2.552	2.601	-	2.509	-	-
^{19}C	2.562	2.629	2.613	2.521	2.709	-
^{20}C	2.573	2.590	2.599	2.532	2.708	-
^{21}C	-	-	2.587	-	2.699	-
^{22}C	-	-	2.584	-	2.698	-
^{20}N	2.671	2.683	-	2.605	-	-
^{21}N	2.674	2.694	2.681	2.614	2.746	-
^{22}N	2.679	2.678	2.678	2.634	2.752	-
^{23}N	2.687	2.674	2.682	2.637	2.760	-
^{20}O	2.720	2.726	2.767	2.668	2.792	-
^{21}O	2.721	2.716	2.753	2.673	2.784	-
^{22}O	2.735	2.712	2.744	2.678	2.783	-
^{23}O	2.741	2.725	2.744	2.689	2.795	-
^{24}O	2.752	2.737	2.750	2.701	2.807	-
^{23}F	2.839	2.805	2.850	2.768	2.873	-
^{24}F	2.838	2.812	2.844	2.778	2.879	-
^{25}F	2.853	2.821	2.846	2.782	2.888	-
^{26}F	2.875	2.852	2.862	2.806	2.920	-
^{27}F	2.891	2.886	2.887	2.827	2.949	-
^{28}F	-	-	2.913	-	2.971	2.966
^{29}F	-	-	2.938	-	2.993	-

Table 3.7 Same as Table 3.6, but for the isotopes of $^{28-32}$Ne, $^{27-35}$Na, $^{30-42}$Mg, and $^{32-35}$Si nuclei.

	r_c in fm					
Nuclei	RMF(NL3) Sph.	RMF(NL3) def.	RMF(NL3*) def.	HF(SEI-I) sph.	SHF(SkI4) def.	Expt. [29,30]
^{28}Ne	2.964	2.966	2.916	2.892	3.025	2.963
^{29}Ne	2.982	2.981	2.977	2.912	3.033	-
^{30}Ne	2.998	2.999	3.000	2.933	3.051	-
^{31}Ne	3.012	3.032	3.019	2.944	3.084	-
^{32}Ne	3.024	3.071	3.084	2.956	3.022	-
^{27}Na	-	-	3.006	-	3.052	3.01
^{28}Na	-	-	3.016	-	3.065	3.04
^{29}Na	-	-	3.027	-	3.078	3.09
^{30}Na	-	-	3.036	-	3.092	3.12
^{31}Na	-	-	3.050	-	3.101	3.101
^{32}Na	-	-	3.072	-	3.135	-
^{33}Na	-	-	3.115	-	3.174	-
^{34}Na	-	-	3.140	-	3.199	-
^{35}Na	-	-	3.163	-	3.224	-
^{30}Mg	-	-	3.078	-	3.128	3.111
^{31}Mg	-	-	3.079	-	3.138	3.148
^{32}Mg	3.095	3.091	3.094	3.032	3.146	3.186
^{33}Mg	3.107	3.118	3.104	3.043	3.179	-
^{34}Mg	3.118	3.151	3.152	3.053	3.215	-
^{35}Mg	3.129	3.174	3.178	3.064	3.240	-
^{36}Mg	-	-	3.200	-	3.266	-
^{37}Mg	-	-	3.214	-	3.281	-
^{38}Mg	-	-	3.226	-	3.298	-
^{39}Mg	-	-	3.238	-	3.309	-
^{40}Mg	-	-	3.250	-	3.320	-
^{41}Mg	-	-	3.266	-	3.3	-
^{42}Mg	-	-	3.284	-	3.3	-
^{32}Si	3.113	3.141	-	3.078	-	-
^{33}Si	3.133	3.134	-	3.095	-	-
^{34}Si	3.153	3.206	-	3.111	-	-
^{35}Si	3.163	3.164	-	3.119	-	-

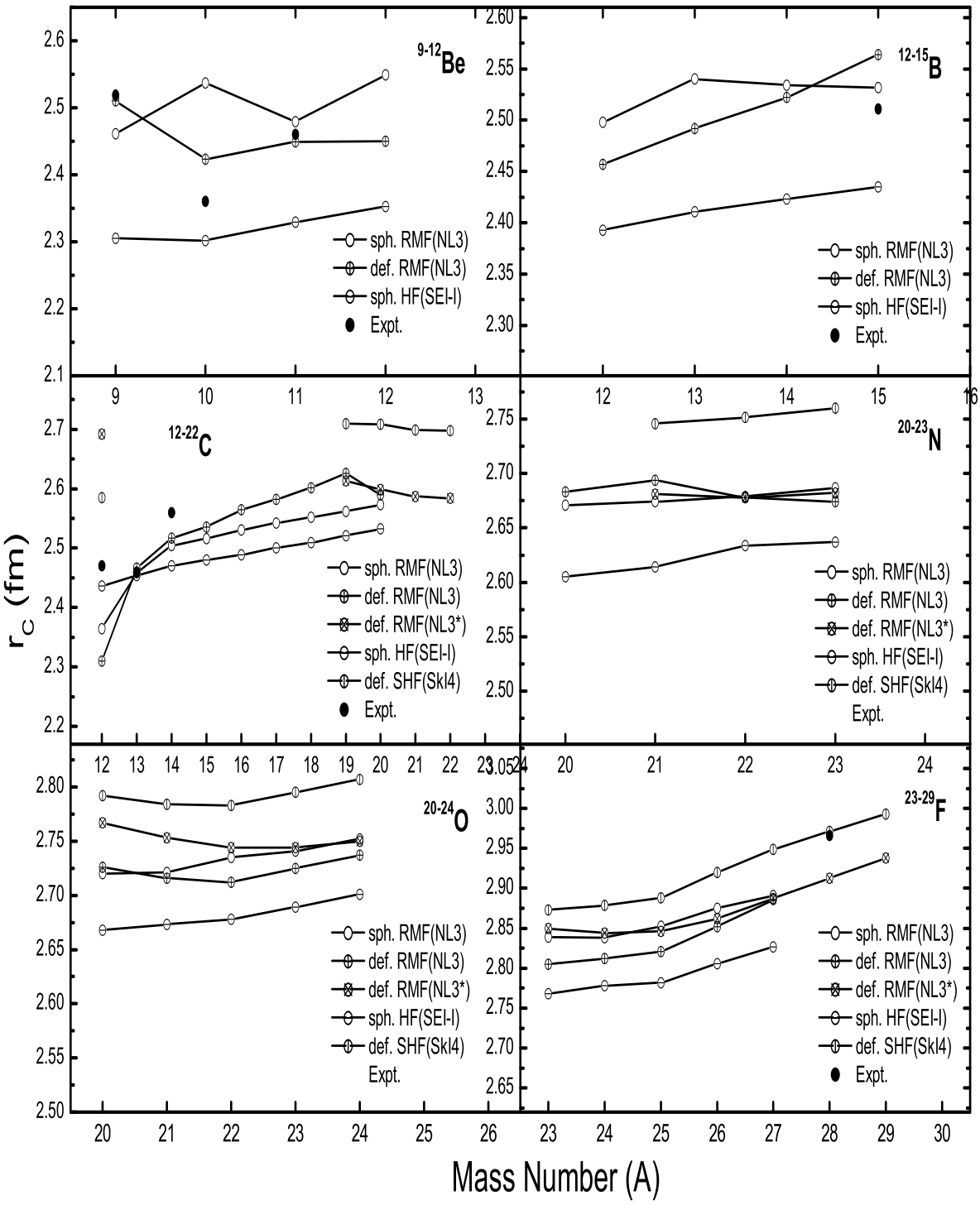

Figure 3.4 The comparison of charge radius (r_c) in fm for Be, B, C, N, O, and F isotopes using sph. RMF(NL3), def. RMF(NL3), def. RMF(NL3*), sph. HF(SEI-I) and SHF(SkI4) formalisms.

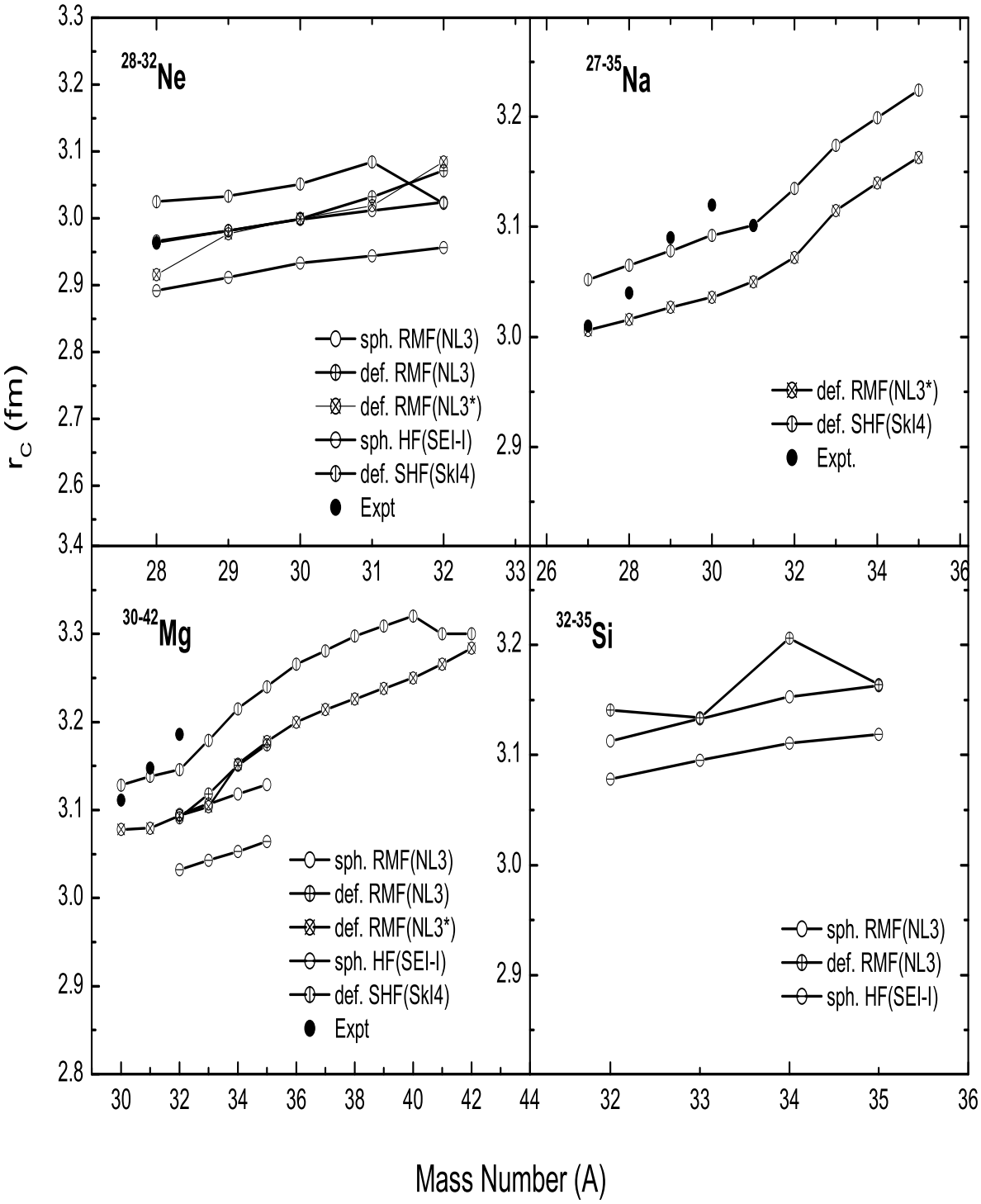

Figure 3.5 Same as figure 3.4, but for Ne, Na, Mg and Si isotopes.

Table 3.8 Same as Table 3.6, but for the isotopes of $^{34-37}$S, $^{33-43}$Al and $^{34-48}$Ar nuclei.

r_c in fm						
Nuclei	RMF(NL3) sph.	RMF(NL3) def.	RMF(NL3*) def.	HF(SEI-I) sph.	SHF(SkI4) def.	Expt. [29, 30]
^{34}S	3.270	3.259	-	3.199	-	3.28
^{35}S	3.282	3.262	-	3.209	-	-
^{36}S	3.293	3.312	-	3.219	-	3.29
^{37}S	3.299	3.290	-	3.224	-	-
^{33}Al	-	-	3.134	-	3.184	-
^{34}Al	-	-	3.1424	-	3.204	-
^{35}Al	-	-	3.169	-	3.234	-
^{36}Al	-	-	3.198	-	3.254	-
^{37}Al	-	-	3.223	-	3.277	-
^{38}Al	-	-	3.240	-	3.288	-
^{39}Al	-	-	3.261	-	3.302	-
^{40}Al	-	-	3.290	-	3.317	-
^{41}Al	-	-	3.316	-	3.328	-
^{42}Al	-	-	3.337	-	3.339	-
^{43}Al	-	-	3.359	-	3.351	-
^{44}Al	-	-	3.3	-	3.346	-
^{34}Ar	3.387	3.360	-	3.295	-	3.365
^{36}Ar	3.388	3.379	-	3.305	-	3.390
^{38}Ar	3.397	3.396	-	3.318	-	3.402
^{40}Ar	3.401	3.392	-	3.326	-	3.427
^{42}Ar	3.406	3.402	-	3.335	-	3.435
^{44}Ar	3.410	3.410	-	3.345	-	3.445
^{46}Ar	3.410	3.415	-	3.373	-	3.437
^{48}Ar	3.437	3.442	-	3.393	-	-

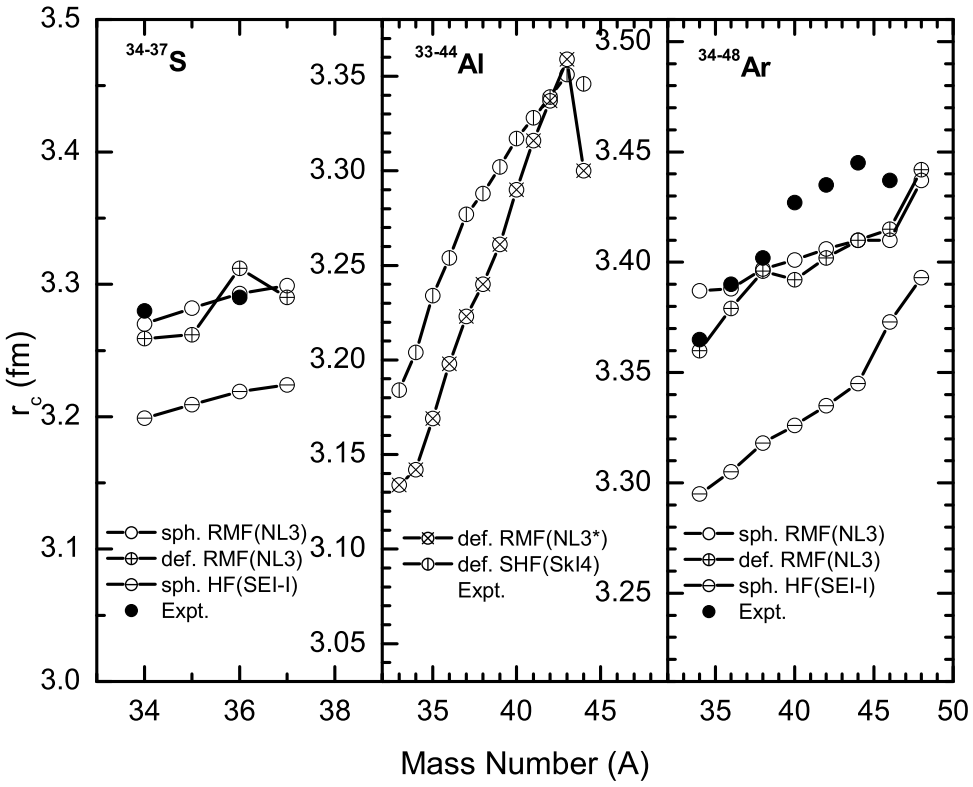

Figure 3.6 Same as figure 3.4, but for S, Al and Ar isotopes.

3.4.3 Deformation parameter

Figure 3.7 shows the plot of a quadrupole deformation parameter (β_2) for some light mass nuclei in terms of their mass number (A) using deformed RMF(NL3*) and SHF(SkI4) formalisms. The values of the deformation parameter decreases for $^{19-22}$C, $^{21-23}$N, $^{20-24}$O and $^{23-29}$F isotopes with an increase of the mass number. Whereas, on the other hand for $^{28-31}$Ne, the calculated values of β_2 first decreases and then increases. But for the heavier isotopes of Na, Mg and Al, the β_2 increases with 'A' as shown in the figure 3.7. In broad observation, almost similar trends are obtained from both the formalisms except for the isotopes of O and F (see Fig. 3.7). The β_2 values of these isotopes are much smaller for RMF as compared to SHF. The O and F isotopes are almost spherical in RMF calculations with an opposite trend of a finite prolate deformation for $^{21-22}$O and $^{23-27}$F in SHF formalisms. In general, for most of the cases, the values of β_2 obtained by

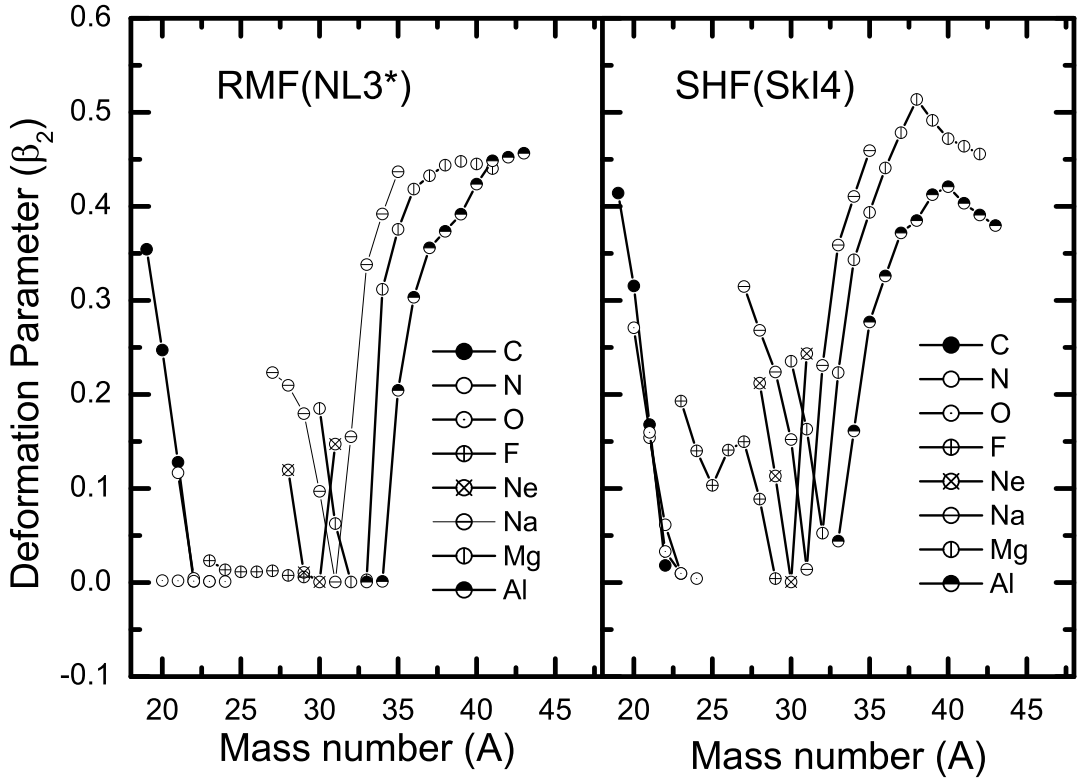

Figure 3.7 Quadrupole deformation parameter β_2 as a function of mass number 'A' obtained from RMF(NL3*) and SHF(SkI4).

the non-relativistic SHF formalism is slightly more than the RMF formalism. In a specific case of ^{12}C, nucleus is almost spherical, whereas majority of the other isotopes of nuclei have prolate deformation.

3.4.4 Nuclear density

A study of a density distribution profile is an important part in our analysis, it is so because our approach of reaction dynamics strongly depends on the profile of the density distributions. The accuracy of reaction observable is based on these profiles. Figure 3.8 represents the densities of $^{9-12}$Be, $^{12-15}$B, $^{12-22}$C, $^{20-23}$N, $^{20-24}$O, $^{23-27}$F, $^{28-32}$Ne, $^{32-35}$Mg, $^{32-35}$Si, $^{34-37}$S and even set of isotopes of $^{34-48}$Ar nuclei as a function of radial distance. The nucleons distribution inside the nucleus is maximum at the centre and starts de-

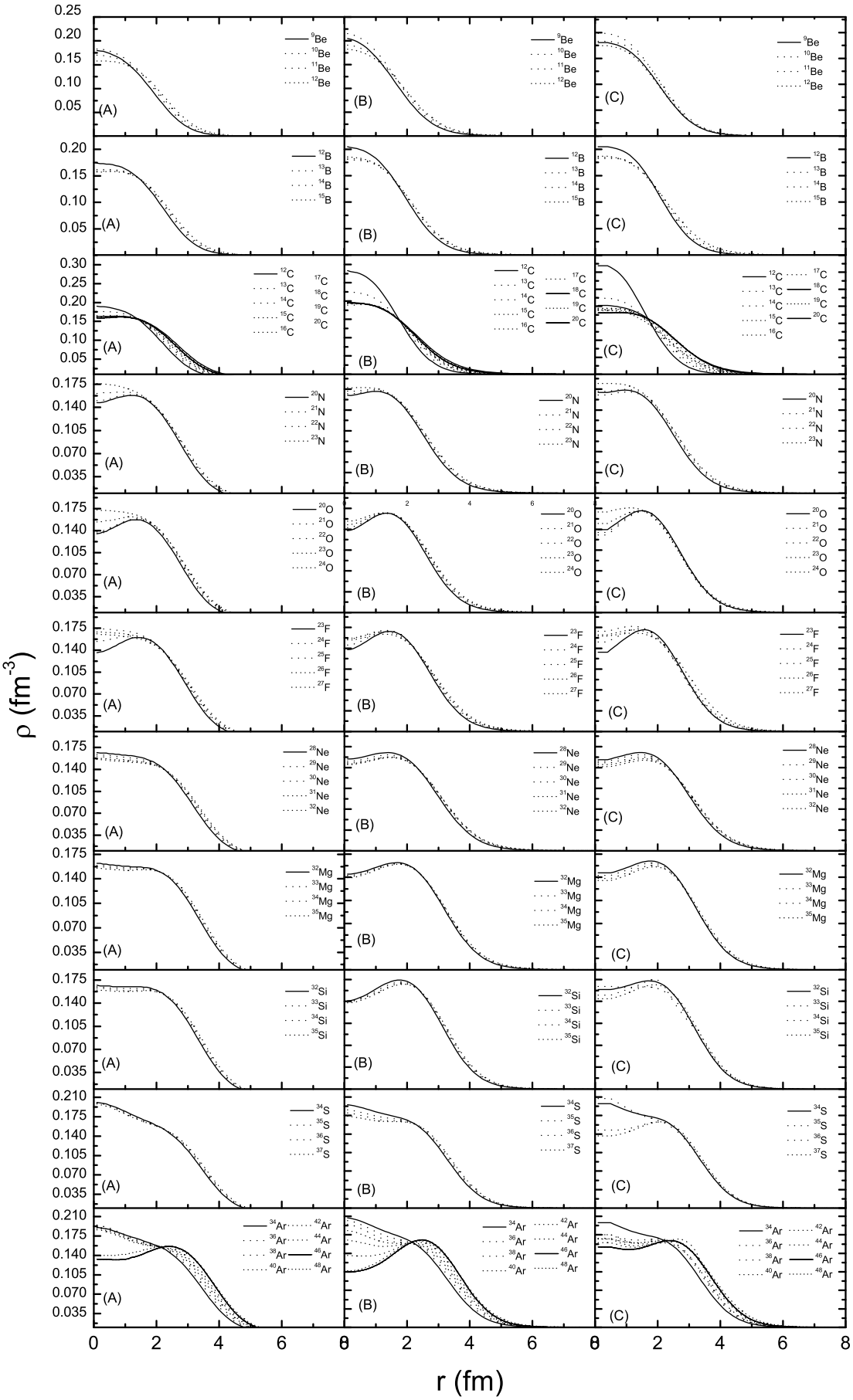

Figure 3.8 The radial density plot of light mass nuclei from Be-Ar isotopes using HF(SEI-I), sph. RMF(NL3) and def. RMF(NL3)formalisms.

creasing continuously towards the surface region. The left panel of the figure represents the nucleonic density distribution obtained by non-relativistic mean field HF(SEI-I) approach. The right panel shows a spherical equivalent of deformed RMF densities with NL3 parameter, whereas the central panel of the figure shows the density distribution obtained from spherical RMF model. It is clear from the figure that the densities of the considered nuclei show a similar kind of trend for all the formalism. A deep inspection of Fig. 3.8 indicates that some of the isotopes of O, F, Si, S and Ar show a depletion of the densities at the centre, which is a primary indication for their bubble structure [31–33]. The details of this effect will be discussed later in the Chapter 4.

3.4.5 Role of BCS paring on bulk properties

The constant gap BCS pairing adds the pairing effects for open shell nuclei. In the present calculations, we have dealt with the nuclei of Ne, Mg and Si isotopes. All these nuclei are in the lower region of the mass table, where the contribution of the pairing effect is minimal even for open the shell nuclei [34]. We also understand that pairing plays a crucial role for the open shell nuclei for a relatively heavier mass region. If we use the conventional pairing gaps similar to $\triangle = 11.2/\sqrt{A}$ MeV, then BCS treatment of pairing is not reliable for nuclei near the driplines. However, using a variable pairing as a function of neutron and proton number near the dripline as suggested by Madland and Nix [35] and successfully used by Patra *et al.* [22], this error can be minimized. To determine the effect of pairing in our calculations, we have estimated B.E., rms charge radii and quadrupole deformation parameter with and without taking pairing into account. The calculated values of the bulk properties such as binding energy (B.E.), root mean square charge radius r_c, and quadrupole deformation parameter β_2 for the neutron rich $^{18-32}$Ne, $^{24-34}$Mg and $^{26-36}$Si are depicted in Table 3.9 and have been compared with the experimental data wherever

Table 3.9 Calculated results for binding energy (B.E.), root mean square charge radius r_c, and quadrupole deformation parameter β_2 for the even sets of neutron rich $^{18-32}$Ne, $^{22-36}$Mg and $^{26-36}$Si isotopes using RMF densities obtained from NL3* parameter set. The available experimental data are also given for the comparison. The B.E. is in MeV and r_c in fm.

Nucleus	B.E.(MeV)		r_c(fm)		β_2			Δ_p	Δ_n
	RMF	Expt.	RMF	Expt [27,36,37].	RMF	Ref. [38,39]	Expt. [27,36,37]		
^{18}Ne	134.35	132.14	3.125	2.972	0.063		0.68(3)	2.3705	2.6213
	131.84		2.963		0.238				
^{20}Ne	155.52	160.65	3.067	3.00	0.063		0.70(20)	2.655	2.655
	156.68		2.972		0.537	0.479			
^{22}Ne	175.34	177.77	3.015	2.954	0.402		0.564(4)	2.5094	2.3114
	175.65		2.94		0.502	0.400			
^{24}Ne	188.92	191.84	2.946	2.903	0.238		0.41(5)	2.1610	1.8572
	189.09		2.88		0.259	0.258			
^{26}Ne	199.78	201.55	2.921	2.927	0.069		0.39(3)	1.7705	1.4335
	200.02		2.926		0.277	0.221			
^{28}Ne	207.62	206.88	2.961	2.963	0.133		0.36(3)	1.4152	1.0876
	208.26		2.965		0.225	0.526			
^{30}Ne	214.66	211.29	2.999		0.010		0.49(17)	1.1202	0.8219
	214.43		2.999		0.099	0.400			
^{31}Ne	214.84	211.62	3.019		0.174			0.9959	0.7152
	214.99		3.031		0.244	0.422			
^{32}Ne	217.12	213.47	3.069		0.368			0.8859	0.06234
	217.62		3.071		0.363	0.335			
^{22}Mg	166.23	168.58	3.213		0.420			2.3114	2.5094
	166.42		3.092		0.513	0.326			
^{24}Mg	193.55	198.26	3.163	3.057	0.467		0.613(14)	2.4984	2.4984
	194.31		3.043		0.487	0.374			
^{26}Mg	212.59	216.68	3.098	3.033			0.484(6)	2.4029	2.2415
	212.54		2.978		0.273	0.310			
^{28}Mg	228.14	231.63	3.071		0.267		0.484(20)	2.1529	1.8912
	228.76		3.048		0.345	0.323			
^{30}Mg	240.08	241.64	3.079		0.197		0.41(3)	1.8487	1.5405
	240.51		3.062		0.241	0.222			
^{32}Mg	250.51	249.81	3.093		0.011		0.51(5)	1.5491	1.2317
	250.59		3.090		0.119	0.000			
^{34}Mg	256.17	256.48	3.151		0.324		0.55(6)	1.2814	0.9768
	257.39		3.150		0.343	0.406			
^{36}Mg	262.25	260.80	3.200		0.429			1.0542	0.7734
	264.13		3.198		0.434	0.328			
^{26}Si	202.14	206.04	3.275		0.373		0.444(21)	2.2415	2.4029
	200.86		3.118		0.280	0.353			
^{28}Si	230.07	236.54	3.149	3.122	0.105		0.412(4)	2.3733	2.3733
	232.13		3.122		0.331	0.478			
^{30}Si	250.81	255.62	3.14	3.133	0.061		0.330(22)	2.3073	2.1724
	250.58		3.070		0.148	0.000			
^{32}Si	267.81	271.41	3.154		0.030		0.26(4)	2.1216	1.8944
	268.45		3.137		0.201	0.000			
^{34}Si	283.57	283.43	3.179		0.011		0.18(4)	1.8818	1.6027
	284.45		3.147		0.001	0.000			
^{36}Si	290.72	292.03	3.189		0.044		0.25(4)	1.6315	1.3316
	291.48		3.184		0.194	0.000			

available [27, 36, 37]. The pairing gaps for proton Δ_p and neutron Δ_n given in the last column of the table, are obtained from equations (2.66) and (2.67). The calculated β_2 values have also been compared with other theoretical calculations [38, 39] and available experimental data in Table 3.9. It is clear that our results agree well with the data. For example, the RMF binding energy for ^{18}Ne is 131.8 MeV whereas the experimental value is 132.1 MeV. Similarly, the r_c value for this nucleus is 2.963 and 2.972 fm for RMF and experiment respectively. A comparison with the study of T. Sumi *et al.* [38] for the deformation parameter β_2 is also depicted in Table 3.9.

3.5 Summary

In this chapter, we have compared the bulk properties like binding energy, root mean square radius, quadrupole deformation, nucleonic densities distribution *etc.* of light mass nuclei from the $\beta-$stability line to the drip-line region. For an investigation of these properties, we have used two different mean field formalisms *i.e.* relativistic and non-relativistic mean field formalism. Firstly we have seen the comparative studies of bulk properties using parameters NL3* and NL-SH for some test cases in relativistic mean field and SkI4 and SLy4 in non-relativistic mean field for the optimization of parameters used. The subsequently study of bosonic and fermionic model space is also done before performing the calculations for drip line systems in RMF formalism. The availability of the experimental data helps us to compare and test our theoretical predictions. The comparison between the estimated values and the experimental data suggests that both the formalisms are capable to reproduce these properties reasonably well. While the deeper inspection of results reveal that the RMF formalism works relatively better when compared with the non-relativistic mean field formalism. The agreement of the

predicted values of B.E., charge radius and other parameters match remarkably well with the experimental observations. This gives enough confidence for further utilization of the densities obtained from RMF(NL3*) and SHF(SkI4), for the reaction dynamics part, which has been covered in Chapters 5 and 6. As the pairing plays an important role in the open shell nuclei, so the role of BCS-pairing is also investigated for the understanding of its effect on the bulk properties of Ne, Mg and Si isotopes in the RMF formalism. As expected, the pairing effect seems to play a marginal role in the light mass region.

Bibliography

[1] T. Otsuka, R. Fujimoto, Y. Utsuno, B. A. Brown, M. Honma and T. Mizusaki, Phys. Rev. Lett. **87**, 082502 (2001).

[2] T. Otsuka, T. Suzuki, R. Fujimoto, H. Grawe and Y. Akaishi, Phys. Rev. Lett. **95**, 232502 (2005).

[3] T. Otsuka, T. Suzuki, J. D. Holt, A. Schwenk and Y. Akaishi, Phys. Rev. Lett. **105**, 032501 (2010).

[4] A. Ozawa, T. Kobayashi, T. Suzuki, K. Yoshida and I. Tanihata, Phys. Rev. Lett. **84**, 493 (2000).

[5] M. Stanoiu *et al.*, Phys. Rev. C **69**, 034312 (2004).

[6] C. R. Hoffman *et al.*, Phys. Lett. B **672**, 17 (2009).

[7] K. Tshoo *et al.*, Phys. Rev. Lett. **109**, 022501 (2012).

[8] R. Kanungo, I. Tanihata and A. Ozawa, Phys. Lett. B **528**, 58 (2002)

[9] J. I. Prisciandaro *et al.*, Phys. Lett. B **510**, 17 (2001).

[10] D. C. Dinca *et al.*, Phys. Rev. C **71**, 041302 (2005).

[11] G. A. Lalazissis, J. Konig and P. Ring, Phys. Rev. C **55**, 540 (1997).

[12] G. A. Lalazissis, S. Karatzikos, R. Fossion, D. Pena Arteaga, A. V. Afanasjev and P. Ring, Phys. Lett. B **671**, 36 (2009).

[13] P. G. Reinhard and H. Flocard, Nucl. Phys. A **584**, 467 (1995).

[14] E. Chabanat, P. Bonche, P. Hansel, J. Mayer and R. Schaeffer, Nucl. Phys. A **627**, 710 (1997).

[15] B. Behera, X. Viñas, M. Bhuyan, T. R. Routray, B. K. Sharma and S. K. Patra, J. Phys. G: Nucl. Part. Phys. **40**, 095105 (2013).

[16] T. R. Routray, X. Viñas, S. K. Tripathy, M. bhuyan, S. K. Patra and B. Behera, J. Phys. Conf. Ser. **420**, 012114 (2013).

[17] S. K. Patra and C. R. Praharaj, Phys. Rev. C **44**, 2552 (1991).

[18] B. D. Serot and J. D. Walecka, Adv. Nucl. Phys. **16**, 1 (1986).

[19] P. Ring, Prog. Part. Nucl. Phys. **37**, 193 (1996).

[20] Y. K. Gambhir, P. Ring and A. Thimet, Ann. Phys. (N. Y.) **198**, 132 (1990).

[21] M. Del Estal, M. Centelles, X. Vinas and S. K. Patra, Phys. Rev. C **63**, 044321 (2001).

[22] S. K. Patra, M. Del Estal, M. Centelles and X. Vinas, Phys. Rev. C **63**, 024311 (2001).

[23] B. K. Sharma, S. K. Patra, R. K. Gupta, A. Shukla, P. Arumugam, P. D. Stevenson and G. Walter, J. Phys. G **32**, 2089 (2006).

[24] S. K. Patra, R. N. Panda, P. Arumugam and R. K. Gupta, Phys. Rev. C **80**, 064602 (2009).

[25] R. N. Panda and S. K. Patra, Int. J. Mod. Phys. E **20**, 2505 (2011).

[26] Mahesh K. Sharma, M. S. Mehta and S. K. Patra, Int. J. Mod. Phys. E **22**, 1350005 (2012).

[27] G. Audi, A. H. Wapstra and C. Thibault, Nucl. Phys. A **729**, 337 (2003).

[28] http://amdc.in2p3.fr/masstable/Ame 2011int/mass.

[29] D. T. Yordanov *et al.*, Phys. Rev. Lett. **108**, 042504 (2012).

[30] I. Angeli, Atom. Data Nucl Table **87**, 185a (2004).

[31] M. Grasso *et al.*, Int. J. Mod. Phys. E **18**, 2099 (2009).

[32] M. Grasso *et al.*, Phys. Rev. C **79**, 034318 (2009).

[33] H. A. Wilson, Phys. Rev. **69**, 538 (1946).

[34] A. Bohr and B. R. Mottelson, Nuclear Structure **Vol II**, 653 (W. A. Benjmin, 1975).

[35] D. G. Madland and J. R. Nix, Nucl. Phys. A **476**, 1 (1981).

[36] G. Audi and M. Wang, Private communication, April (2011).

[37] National Nuclear Data Center, Brookhven National Laboratory, based on ENSDF and the nuclear Wallet Cards.

[38] T. Sumi *et al.*, Phys. Rev. C **85**, 064613 (2012).

[39] P. Moller and J. R. Nix, Atom. Data Nucl. Data Tables **59**, 185 (1995).

Chapter 4

Study of bubble nuclei using mean field densities

4.1 Introduction

A study of the nuclear structure is one of the major area of nuclear science investigations. The simplest topologies other than that of a sphere are those of a torus and bubble. The idea of such type of formalism is suggested by Wheeler [1, 2]. With the advancement of radio-active ion beam facilities, the nucleon-antinucleon annihilation may take place deep in the interior of the nucleus, which in turn results in the creation of a hole in the interior of the nucleus. The simplest idea about the nuclear behavior can be generated via liquid drop model and spherical shell model description, but they don't exhibit the behavior of nuclear shapes. For exhibiting the behavior of nuclear deformations, one has to adopt a collective model description, where the rotational and the vibrational degrees of freedom play significantly an important role. It may be noted that when a heavy ion of high energy (such as ^{14}N beam at few GeV) [3] collides with a target nucleus, then those target nucleons which make collisions (either with the primary nucleons of projectile or

the secondary elementary particles), will travel forward in the projectile direction and become knocked out from the target nucleus. Thus, if the trajectory of the projectile lies inside the target nucleus, the local density of nucleons along the trajectory in the target nucleus gets depleted. It is therefore conceivable that for some trajectories, the remnant after the collision has a hole in the middle, which has the topology of a torus. The bubble and toroidal nuclei may also be expected in the boiling off nuclear matter stage exhibited in a neutron star [4]. In series of papers, Wong [5–7] studied the effects of bubble and toroidal nuclei using the shell correction method. The bubble structure has been observed in some nuclei like ^{22}O, ^{23}F, ^{34}Si, ^{36}S, ^{36}Ar, ^{46}Ar, ^{84}Se, ^{134}Ce, ^{174}Yb, ^{200}Hg *etc.* [7–9]. The densities of such cases is depleted in the central region. This phenomenon has greater interest, as it may change its shape of density distribution from normal nuclei due to different mean field interactions. The possibility of the formation of bubble nuclei has been studied by various nuclear models. The microscopic calculations using Skyrme Hartree-Fock (SHF) formalism have been carried out to investigate this effect for various region as in Ref's. [10–12]. Recently, relativistic and non-relativistic mean field formalism are used to investigate such effect in light [13] and superheavy mass regions [14]. In the following, we have used the concept of mean field densities to address the behavior of light mass bubble nuclei.

4.2 Nucleonic density profiles using mean field formalisms

The success of the mean field formalism to reproduce the bulk properties of nuclei forming wide range of nuclear chart, provides a sufficient confidence to use this approach for extracting nuclear densities. The capability to reproduce the bulk properties of light mass region and the observation of bubble effect in density, discussed in previous chapter, motivates us to see the bubble effect in the considered cases.

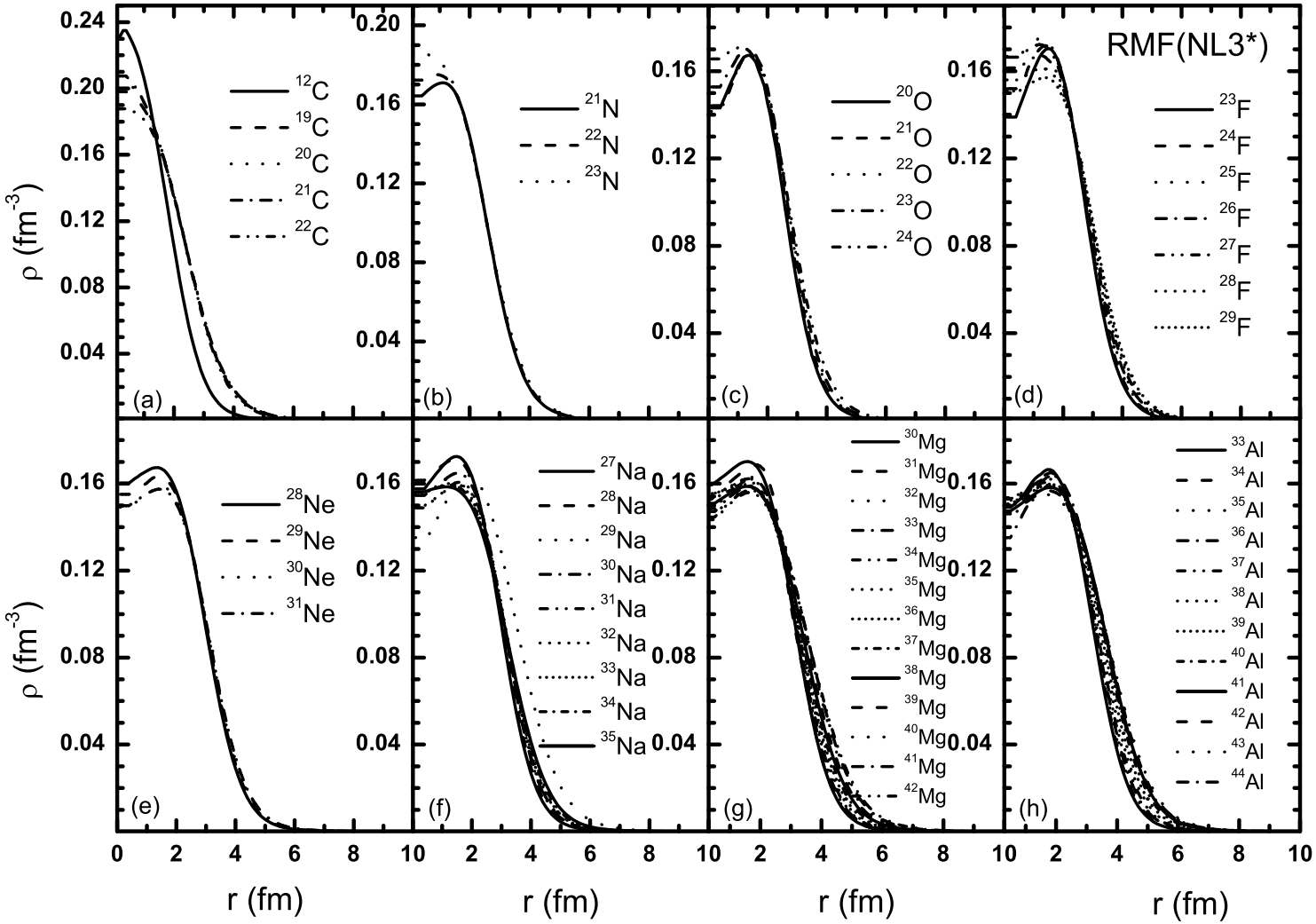

Figure 4.1 The nuclear density distributions for an isotopes of C-Al nuclei as a function of radial distance obtained from RMF(NL3*).

The densities of $^{12-22}$C, $^{21-23}$N, $^{20-24}$O, $^{23-29}$F, $^{28-31}$Ne, $^{27-35}$Na, $^{30-42}$Mg and $^{33-44}$Al obtained from relativistic and non-relativistic mean field calculations are plotted in Figure's 4.1 and 4.2, respectively. The RMF densities for $^{12-22}$C isotopes indicate that nucleons in ^{12}C are more compact at the center as compared to other isotopes of the series. The lighter isotopes of N, O, F are relatively less dense at the center, indicating the recently discussed bubble type shape [8, 9].

The depletion in density for some of the nuclei in the central region suggests to look out for the bubble structure of such nuclei [1, 2, 10]. The bubble effect of nuclei are studied by the depletion factor (D.F.) defined as [8, 9]

$$D.F. = \frac{\rho_{max} - \rho_{cen}}{\rho_{max}}, \tag{4.1}$$

where ρ_{max} is the maximum value and ρ_{cen} is the central density of the nucleus. From Figure 4.1, it is clear that except for C isotopes, the density at the center of all other nuclei i.e. $^{21-23}$N, $^{20-24}$O and $^{23-29}$F (upper panel) increases with neutron number N. The D.F. of ^{21}N are 4% and 4% respectively for RMF and SHF calculations. These values for $^{20-24}$O are 14%, 14%, 16%, 10%, 3% with RMF and 8%, 9%, 11%, 5%, 2% with SHF. Similarly, the depletion factor values for $^{23-24}$F are 18% and 11% with RMF and 9% and 5% with SHF, respectively. The calculated D.F. are shown in Table 4.1. In other nuclei, the trend in the density distribution is somewhat reversed *i.e.*, for C, Ne, Na and Mg, a slight depression occurs at the center with an increase in skin thickness as a function of neutron number. For such cases a linger tail appears. The different trend in the density distribution for ^{29}Na compared to its neighboring isotopes may be due to the filling of last neutrons. In ^{28}Na, the last single neutron is in $[200]^{\frac{3}{2}^+}$ level whereas in ^{29}Na there are two (even number) neutrons in the same orbital, which may shift the energy levels to upward causing

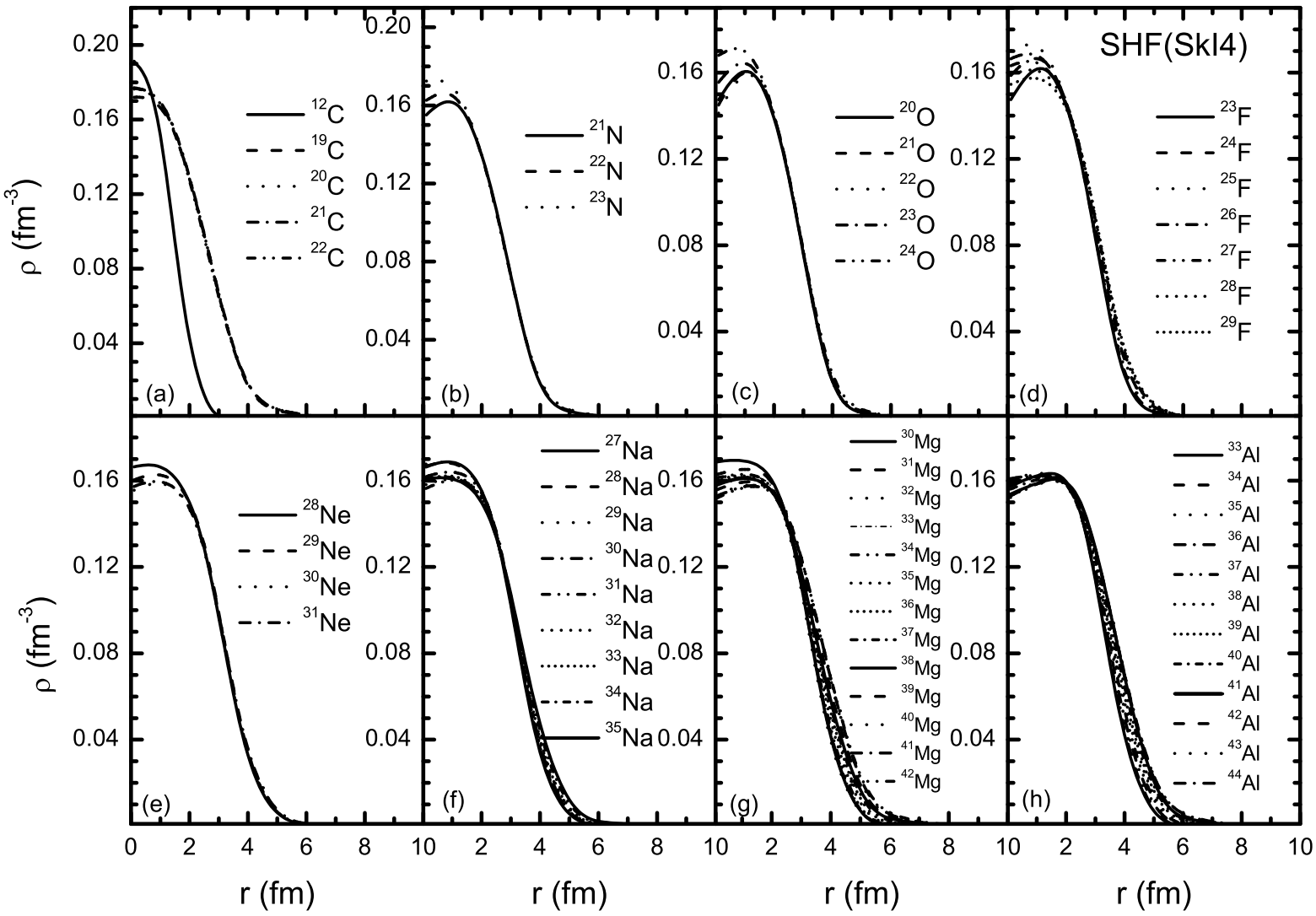

Figure 4.2 The nuclear density distribution for same set of isotopes as in Fig. 4.1, but obtained from SHF(SkI4).

Table 4.1 Depletion factor (D.F. in %) for total density distribution of nucleons in RMF(NL3*) and SHF(SkI4).

D.F. in %								
Nuclei	RMF	SHF	*Nuclei*	RMF	SHF	*Nuclei*	RMF	SHF
^{12}C	1	0	^{19}C	0	0	^{20}C	0	0
^{21}C	0	0	^{22}C	0	0	^{21}N	4	4
^{22}N	1	2	^{23}N	0	0	^{20}O	14	8
^{21}O	14	9	^{22}O	16	11	^{23}O	10	5
^{24}O	3	2	^{23}F	18	9	^{24}F	11	5
^{25}F	5	2	^{26}F	3	1	^{27}F	3	1
^{28}F	3	1	^{29}F	4	2	^{28}Ne	4	0
^{29}Ne	5	1	^{30}Ne	6	2	^{31}Ne	5	1
^{27}Na	9	1	^{28}Na	5	1	^{29}Na	17	0
^{30}Na	6	1	^{31}Na	7	2	^{32}Na	6	1
^{33}Na	3	1	^{34}Na	2	0	^{35}Na	1	0
^{30}Mg	6	0	^{31}Mg	9	1	^{32}Mg	8	3
^{33}Mg	9	2	^{34}Mg	5	1	^{35}Mg	4	0
^{36}Mg	2	0	^{37}Mg	5	1	^{38}Mg	5	2
^{39}Mg	6	2	^{40}Mg	7	3	^{41}Mg	8	3
^{42}Mg	8	3	^{33}Al	10	3	^{34}Al	11	3
^{35}Al	8	1	^{36}Al	6	1	^{37}Al	4	0
^{38}Al	5	1	^{39}Al	5	2	^{40}Al	6	3
^{41}Al	7	4	^{42}Al	7	4	^{43}Al	6	5
^{44}Al	17	5						

the decrease in central density. The calculated D.F. for ^{29}Na are ∼17% and ∼0% with RMF and SHF respectively. The qualitative trend of the non-relativistic SHF densities as shown in Fig. 4.2 are almost similar to the RMF evaluation, of course showing smaller magnitude as compared to RMF results. Hence from above observation, we conclude that the isotopes $^{20-24}$O and $^{23-24}$F are having significant values of depletion factors, which indicates their bubble like structure. This observation is independent of SHF or RMF choice of densities. The most prominent isotopes, which exhibit bubble structure are ^{22}O and ^{23}F with largest values of depletion factors 16 %, 11 % and 18 %, 9 % from RMF(NL3*) and SHF(SkI4) respectively. Therefore in the search of some other bubble nuclei and more information in the structure of these isotopes, we have extended our study for some selective cases like ^{22}O, ^{23}F, ^{34}Si, ^{36}S, ^{36}Ar and ^{46}Ar. In this regard, a study of the structural properties of these nuclei has been done using microscopic non-relativistic Hartree-Fock formalism with recently developed simple effective interaction [15, 16]. The calculations have also been compared with the results of well known relativistic mean field formalism [17–21]. The structural properties like binding energy, charge radius *etc.* for such nuclei are found to be in good agreement with the experimental data. The details of the further calculations are given below:

4.3 Bulk properties of bubble nuclei

The bubble effect seems evident in some of the nuclei where the density of a nucleus is depleted at the central part. The main mechanism for the formation of bubble nuclei is the lack of particles at the center of the nucleus, which causes the *s*-levels to be less bound than the ones observed in usual cases having a uniform density distribution.

4.3.1 Binding energies (B.E.) and Charge radius (r_c)

Fig. 4.3 represents the B.E. and charge radius (r_c) of ^{22}O, ^{23}F, ^{34}Si, ^{36}S ^{36}Ar and ^{46}Ar bubble nuclei obtained from HF(SEI-I), sph. RMF(NL3) and def. RMF(NL3) formalism

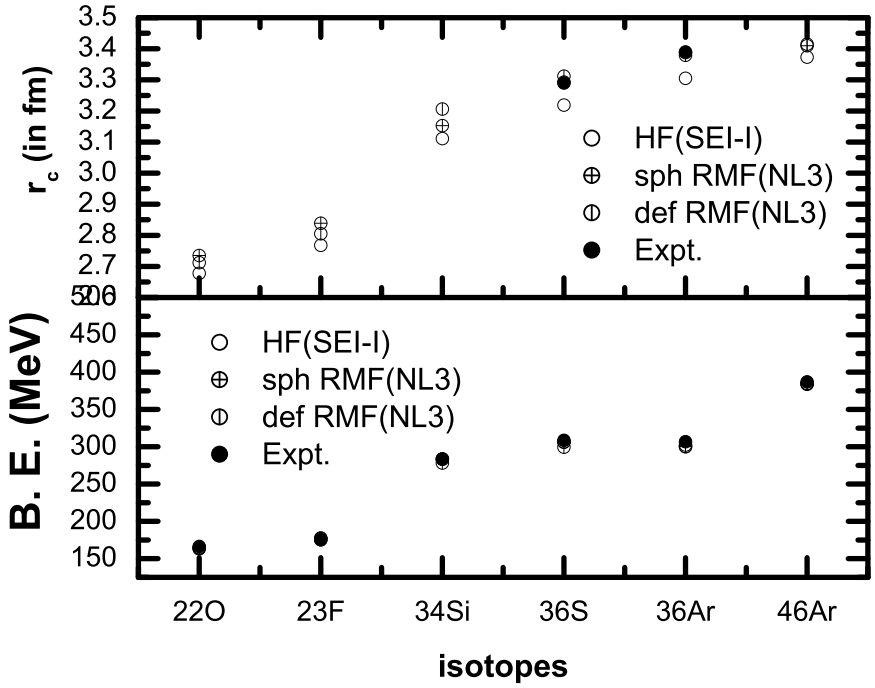

Figure 4.3 Binding energy and charge radius of ^{22}O, ^{23}F, ^{34}Si, ^{36}S, ^{36}Ar and ^{46}Ar bubble nuclei along with available experimental data [22–24].

along with the experimental data [22–24]. The upper panel of the figure shows the charge radius and the lower panel depicts B.E. of selected cases with the experimental data, wherever available [22–24]. This figure suggests that both relativistic mean field and non-relativistic mean field formalisms are capable of reproducing the bulk properties of the bubble nuclei. The deep inspection of the figure suggests that the results obtained with the relativistic mean field formalism are much closer to the experimental values in comparison to that of the non-relativistic mean field formalism.

4.3.2 Density profile of ^{22}O, ^{23}F, ^{34}Si, ^{36}S, ^{36}Ar and ^{46}Ar nuclei

Fig. 4.4 represents the radial density distribution of the considered set of a bubble nuclei. In normal cases, nucleon distribution inside the nucleus is maximum at the center and

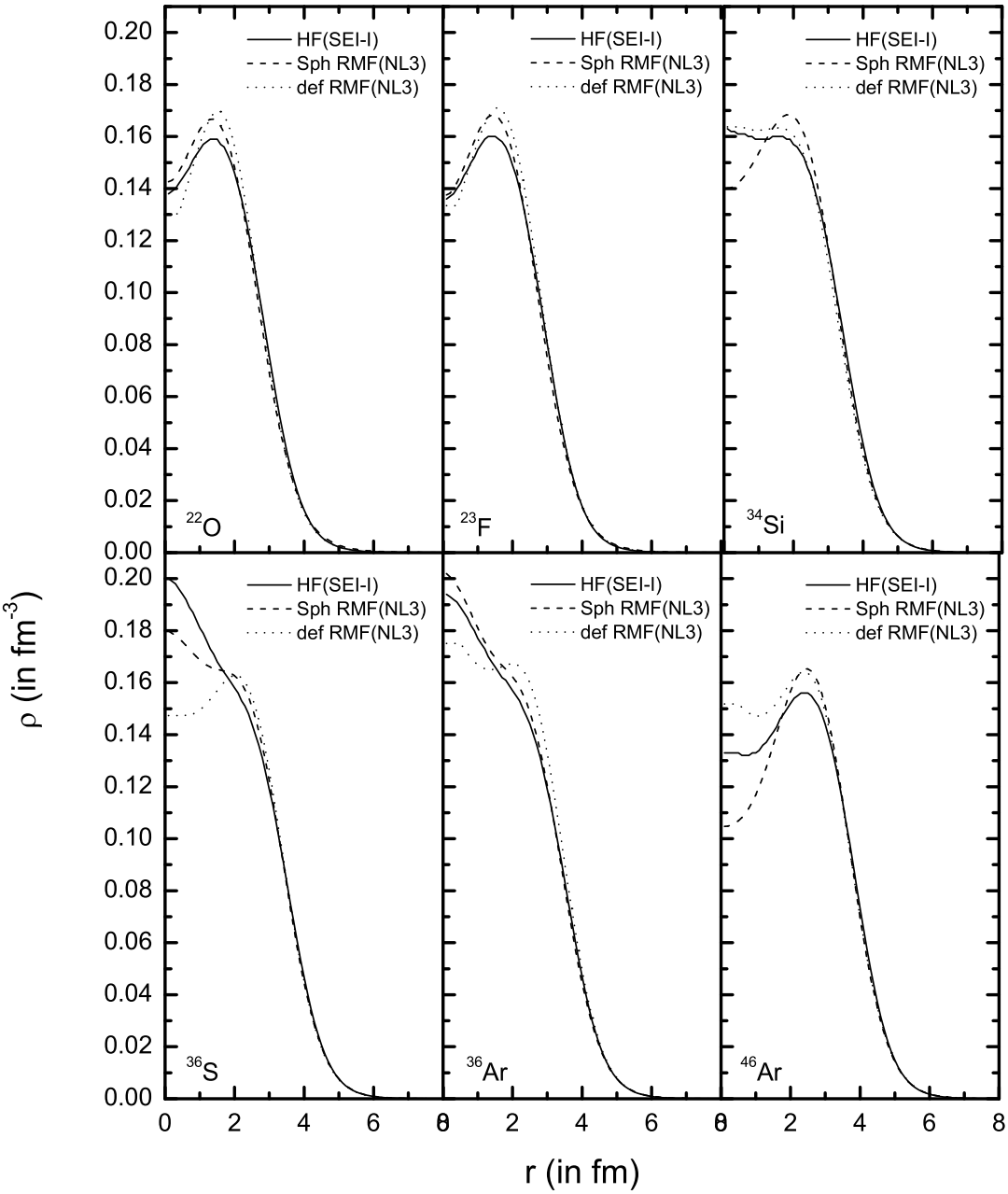

Figure 4.4 Radial density plots of ^{22}O, ^{23}F, ^{34}Si, ^{36}S, ^{36}Ar and ^{46}Ar bubble nuclei obtained from HF(SEI-I), sph. RMF(NL3) and def. RMF(NL3) formalisms.

starts decreasing continuously towards the surface. A keen inspection of this figure suggests that a considered set of nuclei show a depletion of the densities at the center, which is the primary indication for their bubble structure. It is also evident from the figure that densities of these nuclei show a similar kind of trend, independent of choice of formalism. Fig. 4.5 contains the proton and neutron density distributions of same set of bubble nuclei as a function of the radial distance. The left panel of the figure consists of the neutron density distribution and the right panel shows the proton density distribution of these bubble cases for HF(SEI-I), sph. RMF(NL3) and def. RMF(NL3) densities, respectively. It is also evident from the figure that, the depletion for proton density distribution is more than the neutron counterpart. This may be due to the Coulomb repulsion between the protons. So the particles rise high enough in energy and the highest s-level becomes empty, resulting in the depletion of the central density of particles, as a consequence of which the radius of the nucleus increases. The calculated values of D.F. in % for the ^{22}O, ^{23}F, ^{34}Si, ^{36}S, ^{36}Ar and ^{46}Ar are presented in Table 4.2. The values of $(D.F.)_T$ in % for ^{22}O are 13.21, 14.46 and 23.28 for the HF(SEI-I), sph. RMF(NL3) and def. RMF(NL3) densities, respectively. Similarly the $(D.F.)_T$ for the ^{23}F are 15, 18.26 and 21.99 from same densities. The $(D.F.)_P$ in % for the ^{34}Si and ^{46}Ar nuclei are 36.36 and 51.06 for HF(SEI-I), 36.27 and 62.08 for sph. RMF(NL3) and 3.72 and 14.72 for def. RMF(NL3) densities which clearly indicate the nature of their proton bubble. This table also suggests no bubble effect appears for ^{36}Ar, whereas 16.25% $(D.F.)_P$ for ^{36}S in def. RMF(NL3) indicates that it may be a case for proton bubble along with ^{34}Si and ^{46}Ar nuclei. Thus, the prominent cases having bubble effects are observed to be ^{22}O, ^{23}F, ^{34}Si and ^{46}Ar.

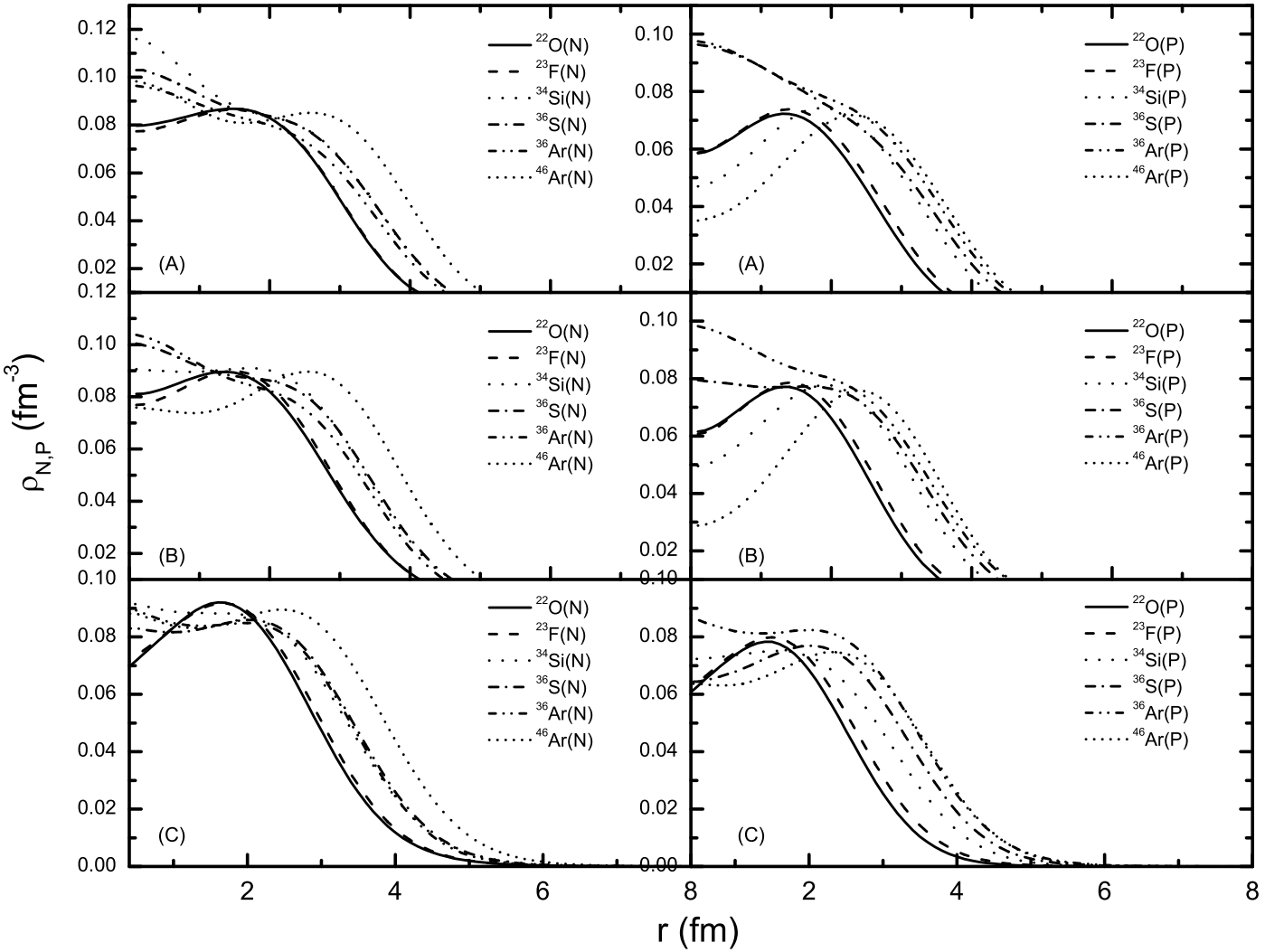

Figure 4.5 Nucleonic density distribution for some expected bubble nuclei ^{22}O, ^{23}F, ^{34}Si, ^{36}S, ^{36}Ar and ^{46}Ar as a function of radial distance obtained by (A) HF(SEI-I) (B) sph. RMF(NL3) (C) def. RMF(NL3) formalisms.

Table 4.2 The Depletion Factor (D.F. in %) of neutron (N), proton (P) and total (T) densities for some probable cases of bubble nuclei obtained from HF(SEI-I), sph. RMF(NL3) and def. RMF(NL3).

Nuclei	D.F.% HF(SEI-I)			D.F.% sph. RMF			D.F.% def. RMF		
	N	P	T	N	P	T	N	P	T
^{22}O	8.21	19.14	13.21	9.49	20.23	14.46	24.35	22.47	23.29
^{23}F	10.67	20.45	15	14.44	22.71	18.26	22.14	22.30	21.99
^{34}Si	-	36.66	-	0.36	36.27	16.75	-	3.73	-
^{36}S	-	-	-	-	-	-	3.49	16.25	9.49
^{36}Ar	-	-	-	-	-	-	-	-	-
^{46}Ar	-	51.05	14.74	15.31	62.08	36.64	1.56	14.73	7.51

4.4 Summary and Conclusions

In this chapter, we have studied the density distribution of $^{9-12}$Be, $^{12-15}$B, $^{13-20}$C, $^{20-23}$N, $^{20-24}$O, $^{23-27}$F, $^{28-32}$Ne, $^{32-35}$Mg, $^{32-35}$Si, $^{34-37}$S and $^{34-48}$Ar isotopes in the frame-work of non-relativistic Hartree-Fock mean field formalism with SkI4 parameter and relativistic mean field formalism with NL3 parameters. As the density is an important parameter to analyze the nuclear structure and an associated dynamical behavior, so an attempt has been made to see an exclusive role of the density distribution in the context of the bubble shape of the nuclei. Many deviations have been seen in the profile of density distributions from their normal trend like neutron/proton skin and depletion in the center (bubble shapes). The bubble effect of the light mass nuclei such as Be-Ar isotopes has been investigated, and such effect has been explored for ^{22}O, ^{23}F, ^{34}Si, ^{36}S, ^{36}Ar and ^{46}Ar isotopes via both relativistic and non-relativistic mean field densities. A systematic study of the density profile and the depletion factor suggests that prominent cases having bubble effects are ^{22}O, ^{23}F, ^{34}Si and ^{46}Ar nuclei.

Bibliography

[1] H. A. Wilson, Phys. Rev. **69**, 538 (1946).

[2] J. A. Wheeler (prior to 1950) unpublished.

[3] J. Hudis and S. Katcoff, Bull. Am. Phys. Soc. II **17**, 489 (1972).

[4] M. G. Mayer and E. Teller, Phys. Rev. **76**, 1226 (1948).

[5] C. Y. Wong, Phys. Lett. B **41**, 446 (1972).

[6] C. Y. Wong, Phys. Lett. B **41**, 451 (1972).

[7] K. T. R Davies, C. Y. Wong and S. J. Krieger, Phys. Lett. B **41**, 455 (1972).

[8] M. Grasso *et al.*, Int. J. Mod. Phys. E **18**, 2099 (2009).

[9] M. Grasso *et al.*, Phys. Rev. C **79**, 034318 (2009).

[10] X. Campi, D. W. L. Sprung, Phys. Lett. B **46**, 291 (1973).

[11] M. Bender, K. Rutz, P. G. Reinhard, J. A. Maruhn and W. Greiner, Phys. Rev. C **60**, 55 (2003).

[12] J. Decharge, J. F. Berger, M. Girod and K. Dietrich, Nucl. Phys. A **716**, 55 (2003).

[13] A. Shukla, Sven A^{0}berg and S. K. Patra, J. Phys. G: Nucl. Part. Phys. **38**, 095103 (2011)

[14] S. K. Singh, M. Ikram and S. K. Patra, Int. J. Mod. Phys. E **22**, 135001 (2013).

[15] B. Behera, X. Vinas, M. Bhuyan, T. R. Routray, B. K. Sharma and S. K. Patra, J. Phys. G: Nucl. Part. Phys. **40**, 095105 (2013).

[16] T. R. Routray, X. Vinas, S. K. Tripathy, M. Bhuyan, S. K. Patra and B. Behera, J. Phys. Conf. Ser. **420**, 012114 (2013).

[17] W. Pannert, P. Ring and J. Boguta, J. Phys. Rev. Lett. **59**, 2420 (1987).

[18] J. Boguta and A. R. Bodmer, Nucl. Phys. A **292**, 413 (1977).

[19] P. Ring, Prog. Part. Nucl. Phys. **37**, 193 (1996).

[20] S. K. Patra and C. R. Praharaj, Phys. Rev. C **44**, 2552 (1991).

[21] M. Del Estal, M. Centelles, X. Vinas and S. K. Patra, Phys. Rev. C **63**, 024314 (2001).

[22] G. Audi, A. H. Wapstra and C. Thibault, Nucl. Phys. A **729**, 337 (2003).

[23] http://amdc.in2p3.fr/masstable/Ame 2011int/mass.

[24] I. Angeli and K. P. Marinova, Atomic Data and Nucl. Data Table **99**, 69 (2013).

Chapter 5

Reaction dynamics of stable and drip-line nuclei

5.1 Introduction

The reaction dynamics is one of the standard tool to investigate the nuclear structure and its related stability aspects. In the last few decades, a series of experiments have been performed on elastic scattering of the unstable nuclei. It has been found that the scattering cross sections show a significantly different behavior for the weakly bound projectiles as compared to that for the tightly bound projectiles like α-particle. The small binding energy of the valence nucleons in an orbital with a small angular momentum leads to wave functions which extend to very large radii, exceeding by far the usual $A^{\frac{1}{3}}$ radius dependence. Due to the corresponding long range absorption, the Fresnel diffraction peak in the elastic scattering angular distribution is damped and the elastic scattering cross section at backward angles becomes relatively smaller. The development of a radioactive ion beam facility indicates further addition of numerous new isotopes towards the drip line. The total nuclear reaction cross section 'σ_R' in a nuclear reaction provides a significant

information regarding the structural aspects of the nuclear systems. It extends a useful quantity to analyze the halo nature of light mass drip-line isotopes. The reaction cross section, angular elastic differential cross section, one nucleon removal cross section and longitudinal momentum distribution cross section are some of the standard parameters, which can be exercised to explore the structure of the nuclear systems. The reaction cross section has direct consequence with the size of the nucleus.

The reaction cross sections of light mass nuclear systems are estimated by Glauber formalism. The Glauber model was initially designed for reactions at high energy. The main success of this model is based on the densities of the projectile and the target nuclei. One of the important inputs of this formalism are energy as well as isospin dependent parameter as discussed in chapter 2. The elastic scattering is the simplest process that occurs in heavy-ion collisions because it involves very little rearrangement of matter and energy. Therefore, this process has been studied in a large number of experimental investigations, and a huge amount of elastic cross section data is currently available. The angular distribution for the elastic scattering provides an unambiguous determination of the real part of an optical potential only in a region around a particular distance [1], hereafter referred as the radius sensitivity (RS). At energies close to the Coulomb barrier, the radius sensitivity is situated in the surface region. In this energy region, the systematization [2, 3] of experimental results for potential strengths at sensitivity radii has provided a universal exponential shape for the heavy-ion nuclear potential at the surface, but with a diffuseness value smaller than that of originally proposed in the proximity potential.

A descriptive discussion of various inputs of the Glauber formalism for the calculation of reaction cross sections are given in the following subsection.

5.2 Inputs of Glauber model

5.2.1 Energy and Isospin dependent parameters

The inputs like energy dependent parameters are required to measure the profile function in Glauber formalism. The appropriate average values of these parameters are estimated with reference to the experimental data. Here, we have estimated these parameters by interpolating various energies as done in Ref. [4–9] using spline interpolation, which is specified in Table 5.1. It is of worth mentioning here that the reaction cross sections for C−isotopes have been evaluated by using two successful methods (i) Glauber model and (ii) nucleon-target profile function in Glauber (NTG) eikonal approximation using a global optical potential [9]. In both the formalisms, the predictive power is almost similar. The calculated value of σ_R for ^{15}C is found to be consistently smaller at low energies [9].

5.2.2 Density conversion

The relativistic mean field (RMF) and Skyrme Hartree Fock (SHF) equations of motion are solved self-consistently in axially deformed coordinates. The obtained densities are in ω and z directions. We arrange the density as a function of ω and ρ for a constant value of z, which exhibits the distribution of the nucleons perpendicular to the symmetry axis. Again, for a particular ω, we re-arrange the density along the parallel direction of symmetry axis as a function of z. This is demonstrated in Fig. 5.1 as a representative case for ^{42}Mg, which is a well deformed nucleus. From the figure, it is clear that the density distribution is significantly different between the perpendicular ($\omega-$axis) and the parallel ($z-$axis) axes with respect to the symmetry axis. From simple geometric consideration, we have used the relation $r = \sqrt{x^2 + y^2 + z^2}$, with $\omega = \sqrt{x^2 + y^2}$ to get the spherical equivalent density as a function of r only as discussed earlier in section 2.3 of chapter 2.

Table 5.1 The nucleon-nucleon cross section σ_{NN} and other parameters like α_{NN} and β_{NN} used to calculate the profile function.

E(MeV/nucleon)	σ_{NN} (fm^2)	α_{NN}	$\beta_{NN}(fm^2)$
30.0	19.600000	0.8700000	0.6850000
38.0	14.600000	0.8900000	0.5210000
40.0	13.500000	0.9000000	0.4860000
49.0	10.400000	0.9400000	0.3900000
85.0	6.1000000	1.3700000	0.3490000
94.0	5.5000000	1.4090000	0.3270000
100.0	5.2950000	1.4350000	0.3220000
120.0	4.5000000	1.3590000	0.2550000
150.0	3.8450000	1.2450000	0.1950000
200.0	3.4500000	0.9530000	0.1310000
230.0	3.3077900	0.7462136	0.1042526
240.0	3.2668680	0.6800303	0.0978437
325.0	3.0300000	0.3050000	0.0750000
425.0	3.0300000	0.3600000	0.0780000
550.0	3.6200000	0.0400000	0.1250000
650.0	4.0000000	-0.0950000	0.1600000
730.0	4.1741300	-0.0828693	0.1896611
740.0	4.1897080	-0.0793203	0.1931483
760.0	4.2173360	-0.0731153	0.1996571
790.0	4.2507720	-0.0691061	0.2078210
800.0	4.2600000	-0.0700000	0.2100000
900.0	4.3116900	-0.1439280	0.2171934
905.0	4.3127750	-0.1498595	0.2170294
920.0	4.3154330	-0.1684008	0.2163436
950.0	4.3185540	-0.2078482	0.2142974
955.0	4.3188530	-0.2146004	0.2138945
960.0	4.3191030	-0.2213738	0.2134798
965.0	4.3193100	-0.2281574	0.2130555
980.0	4.3197250	-0.2484590	0.2117466
1000.0	4.3200000	-0.2750000	0.2100000
1005.0	4.3200550	-0.2814692	0.2095773
1010.0	4.3201100	-0.2878605	0.2091625
1020.0	4.3202200	-0.3004108	0.2083566

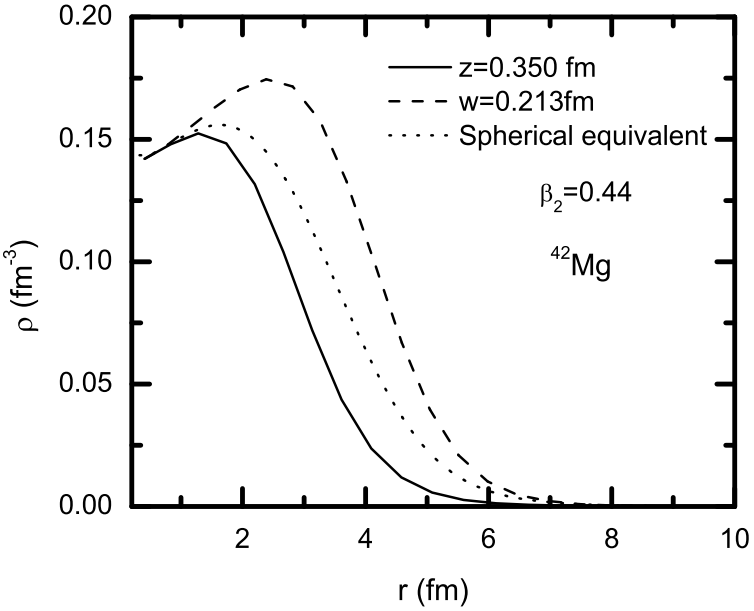

Figure 5.1 The parallel and perpendicular components of deformed RMF(NL3*) density distribution for ^{42}Mg isotope compared with its spherical equivalent.

This spherical equivalent $\rho(r)$ can be used like a one dimensional density, as discussed in our subsequent calculations. The one dimensional density is easy to convert in terms of Gaussian form (see eq'n 2.67), which in turn serves as an input to the Glauber model. A detail of the conversion process is given in the next subsection.

5.2.3 Gaussian coefficients

Another important ingredient of the Glauber model for an estimation of the reaction dynamics is the densities of the projectile and the target nuclei. The success of relativistic and non-relativistic mean field formalisms leads us to predict more accurate values of such distributions. These mean field densities cannot be feeded directly to the Glauber model. To use these densities in the Glauber model one needs to convert these densities in terms of Gaussian coefficients.

In this subsection, first we have fitted the spherically equivalent deformed densities for 2

Gaussian (2G) and 4 Gaussian (4G) fit by taking $n = 2$ and 4 in equation (2.67). These coefficients of c_i and a_i ($i = 2$ and 4) are listed in Tables 5.2, 5.3 and 5.4. Table 5.2 consists of 2G fitted coefficients for $^{12,19-22}$C, $^{21-23}$N, $^{20-24}$O, $^{23-29}$F, $^{28-32}$Ne, $^{27-35}$Na, $^{30-42}$Mg and $^{33-44}$Al isotopes for both RMF(NL3*) and SHF(SkI4) densities. Whereas Tables 5.2 and 5.3 consists of 4G fitted coefficients for the same set of isotopes using RMF(NL3*) and SHF(SkI4) densities, respectively. It is relevant to see a comparison between the densities of the Gaussian coefficient and mean field densities before using these coefficients as an input of Glauber model. In this concern, the actual RMF density for some of the selected test cases of ^{12}C, ^{19}C, ^{20}C, ^{21}N, ^{30}Na and ^{40}Mg isotopes are compared with the density simulated with 2 and 4 Gaussian fit and the results are depicted in Fig 5.2. The lower panel of the figure demonstrates the density in logarithmic scale to have a better picture of the tail region, because the tail region contributes much in reaction dynamics. From this figure, it is clearly seen that the overall fit with the 2 Gaussian (2G) densities appear reasonably better for RMF densities as compared to the (4G) fit densities.

Figure 5.3 shows a similar comparison of the simulated densities with the SHF cases. In this figure, the reversed trend has appeared. The fitting is somewhat better in the tail region, when a four Gaussian (4G) is compared to 2 Gaussian (2G) fitting. The coefficient of (2G) fittings are given in Table 5.2 for both RMF and SHF densities, whereas the values of the coefficients c_i and a_i are listed in Table 5.3 for (4G) RMF densities and in Table 5.4 for (4G) SHF densities.

Table 5.2 The second order Gaussian coefficients (2G) with RMF(NL3*) and SHF (SkI4) fitting.

	RMF(NL3*)				SHF(SkI4)			
$Nuclei$	c_1	a_1	c_2	a_2	c_1	a_1	c_2	a_2
^{12}C	-0.169195	0.577368	0.418511	0.300552	-3.19344	0.351467	3.38116	0.334461
^{19}C	-1.87914	0.259339	2.01367	0.235328	-1.28523	0.219322	1.41374	0.199015
^{20}C	-1.66632	0.254873	1.82126	0.229729	-1.26702	0.219759	1.40684	0.198654
^{21}C	-2.97731	0.245056	3.15758	0.231707	-1.28856	0.229014	1.44526	0.205384
^{22}C	-0.13063	0.35694	0.344777	0.178756	-0.46197	0.270469	0.644662	0.199519
^{21}N	-2.38804	0.271078	2.53082	0.246417	-1.36151	0.248036	1.49832	0.2173
^{22}N	-0.883986	0.29461	1.05663	0.231644	-1.55019	0.248562	1.70531	0.220601
^{23}N	-0.456336	0.301253	0.644644	0.20612	-1.42762	0.245538	1.60143	0.216816
^{20}O	-2.63298	0.310682	2.76965	0.278993	-1.3913	0.247438	1.5068	0.217118
^{21}O	-2.73861	0.302688	2.8717	0.272288	-1.73028	0.253495	1.85409	0.225394
^{22}O	-2.83427	0.293207	2.96827	0.264657	-2.08759	0.264442	2.22132	0.236606
^{23}O	-2.5036	0.281742	2.6512	0.252704	-1.9695	0.255628	2.12071	0.22888
^{24}O	-4.2204	0.259231	4.38671	0.244501	-4.20627	0.237479	4.37221	0.226148
^{23}F	-3.21319	0.285385	3.3394	0.259889	-1.47438	0.233065	1.59281	0.204429
^{24}F	-3.00539	0.275318	3.14594	0.250366	-1.54506	0.228806	1.67777	0.2024
^{25}F	-2.69645	0.260557	2.85593	0.236943	-1.54549	0.223303	1.69301	0.198565
^{26}F	-2.6063	0.248311	2.76589	0.226075	-1.4706	0.209273	1.60925	0.186201
^{27}F	-2.54674	0.235991	2.70055	0.215146	-1.47647	0.200593	1.60954	0.178841
^{28}F	-2.54235	0.227103	2.69029	0.207233	-1.65525	0.201775	1.79125	0.180857
^{29}F	-2.54852	0.219287	2.69126	0.200268	-4.48139	0.202954	4.62849	0.193868
^{28}Ne	-2.68685	0.218885	2.81286	0.200789	-1.41249	0.187338	1.53513	0.167237
^{29}Ne	-2.80577	0.223261	2.94678	0.204765	-3.92485	0.190228	4.0548	0.181334
^{30}Ne	-2.90293	0.22326	3.04881	0.204765	-2.14573	0.206354	2.29097	0.187242
^{31}Ne	-2.69474	0.203279	2.81029	0.186235	-2.85161	0.17282	2.97359	0.162829
^{32}Ne	-1.0259	0.184479	1.15029	0.155872	-1.06253	0.183871	1.1926	0.156729
^{27}Na	-2.75311	0.220871	2.86195	0.202661	-1.43385	0.184957	1.54712	0.166011
^{28}Na	-2.74136	0.218955	2.8527	0.200466	-1.50194	0.184491	1.61798	0.165736
^{29}Na	-2.72488	0.210271	2.83723	0.192986	-1.55971	0.184238	1.67898	0.165537
^{30}Na	-2.88103	0.212688	2.99964	0.19529	-1.75712	0.188205	1.87959	0.16962
^{31}Na	-1.84859	0.227886	1.98941	0.198127	-2.21396	0.202805	2.35429	0.184094

Table 5.2 continued.

	RMF(NL3*)				SHF(SkI4)			
Nuclei	c_1	a_1	c_2	a_2	c_1	a_1	c_2	a_2
^{32}Na	-2.85085	0.201045	2.95989	0.18443	-1.47493	0.175272	1.59232	0.155993
^{33}Na	-2.61162	0.189684	2.71649	0.173667	-2.3097	0.15323	2.41969	0.143676
^{34}Na	-2.47959	0.180204	2.58218	0.165026	-2.21549	0.143372	2.32036	0.134741
^{35}Na	-1.56633	0.13153	1.64195	0.120779	-2.13713	0.134652	2.23731	0.126826
^{30}Mg	-2.85085	0.207626	2.95863	0.190729	-1.67137	0.181447	1.78766	0.163621
^{31}Mg	-3.07236	0.214901	3.19436	0.197462	-4.11624	0.180562	4.23597	0.172326
^{32}Mg	-3.14121	0.215721	3.27192	0.198145	-2.14978	0.19549	2.28076	0.177045
^{33}Mg	-3.14637	0.211096	3.27551	0.193894	-1.65848	0.172959	1.77273	0.15522
^{34}Mg	-2.72369	0.186362	2.82369	0.170924	-1.26296	0.15775	1.3698	0.139606
^{35}Mg	-2.63207	0.17827	2.7282	0.16354	-1.31818	0.147535	1.41996	0.132193
^{36}Mg	-2.58396	0.171635	2.67618	0.157531	-2.51475	0.135506	2.61205	0.128241
^{37}Mg	-2.6057	0.168656	2.69665	0.154832	-1.38706	0.136493	1.48349	0.123582
^{38}Mg	-2.65101	0.16633	2.7405	0.152757	-1.30631	0.139371	1.40893	0.124877
^{39}Mg	-2.70506	0.164315	2.79411	0.151012	-2.72843	0.130763	2.82317	0.12394
^{40}Mg	-2.72653	0.161259	2.8146	0.148298	-2.98279	0.130434	3.07696	0.123961
^{41}Mg	-1.9176	0.143155	1.99748	0.129699	-1.44887	0.134225	1.54838	0.120924
^{42}Mg	-4.08053	0.135833	4.15992	0.129709	-1.55971	0.130426	1.65564	0.118372
^{33}Al	-3.30197	0.215088	3.42956	0.197664	-2.30312	0.194897	2.43549	0.177008
^{34}Al	-3.29727	0.210286	3.42323	0.193247	-1.87479	0.177221	1.99483	0.159783
^{35}Al	-1.30998	0.235532	1.37557	0.181819	-1.41032	0.161591	1.52229	0.143532
^{36}Al	-2.77458	0.179283	2.87145	0.164565	-2.98684	0.147428	3.0934	0.139725
^{37}Al	-2.68485	0.171731	2.77782	0.157672	-1.46515	0.143023	1.56671	0.129219
^{38}Al	-2.68058	0.167474	2.77188	0.153851	-1.47224	0.142153	1.57349	0.128173
^{39}Al	-2.68361	0.163411	2.77449	0.150276	-1.44322	0.141007	1.54397	0.126646
^{40}Al	-2.65962	0.158524	2.74834	0.145895	-1.4449	0.139122	1.54433	0.124807
^{41}Al	-2.6448	0.154438	2.73197	0.142219	-3.42826	0.134824	3.5272	0.128458
^{42}Al	-2.61286	0.151115	2.69952	0.13913	-3.41232	0.133449	3.51253	0.12708
^{43}Al	-2.56627	0.147747	2.6527	0.135973	-3.38838	0.13189	3.48966	0.125532
^{44}Al	-3.09818	0.165568	3.1971	0.15212	-1.60118	0.137808	1.70747	0.123801

Table 5.3 Same as Table 5.2, but for fourth order Gaussian fit (4G) with RMF(NL3*) density.

	RMF(NL3*)							
Nuclei	c_1	a_1	c_2	a_2	c_3	a_3	c_4	a_4
^{12}C	-0.526735	0.449935	-0.075015	0.269344	0.834403	0.341758	0.005696	0.078590
^{19}C	-0.175574	0.389343	0.023024	0.182887	0.320555	0.191013	0.000000	0.030000
^{20}C	-0.200915	0.342960	-0.212358	0.152290	0.603392	0.176117	0.000000	0.030000
^{21}C	-0.185163	0.342633	-0.238429	0.173284	0.625237	0.182821	0.000000	0.030000
^{22}C	-0.123660	0.369339	0.003452	0.177952	0.334174	0.177882	0.000000	0.030000
^{21}N	-0.657198	0.320473	-0.079272	0.227535	0.892167	0.229349	0.000000	0.059559
^{22}N	-0.533836	0.322229	-0.128727	0.217490	0.834635	0.219124	0.000000	0.096826
^{23}N	-0.386945	0.315025	-0.197194	0.201194	0.771692	0.201962	0.000000	0.045102
^{20}O	-1.565900	0.294641	-0.396372	0.187645	2.036440	0.238748	0.048739	0.154771
^{21}O	-1.601360	0.303475	-0.417038	0.186564	2.094500	0.242448	0.059202	0.153962
^{22}O	-1.737120	0.294418	-0.441427	0.188218	2.260790	0.238907	0.053189	0.155258
^{23}O	-1.747070	0.282305	-0.395305	0.189986	2.255770	0.233601	0.0350983	0.155760
^{24}O	-0.925814	0.273068	-0.013856	0.202176	1.097350	0.215767	0.000000	0.042424
^{23}F	-0.885744	0.271440	0.140750	0.210488	0.901116	0.214031	-0.015359	0.204620
^{24}F	-1.786080	0.288170	-0.137633	0.218391	1.964890	0.244923	0.099015	0.215352
^{25}F	-1.563080	0.273334	-0.091486	0.205594	1.749750	0.231518	0.063725	0.202335
^{26}F	-0.510410	0.298187	-0.175433	0.147918	0.845591	0.182054	0.000000	0.030000
^{27}F	0.842092	0.464736	-1.303760	0.397305	0.624182	0.192419	0.000000	0.030000
^{28}F	0.960048	0.449474	-1.422510	0.387785	0.620002	0.185965	0.000000	0.030000
^{29}F	0.970558	0.435184	-1.442900	0.373897	0.624611	0.180629	0.000000	0.030000
^{28}Ne	0.804787	0.410319	-2.337630	0.305965	1.711500	0.225351	-0.022270	0.215946
^{29}Ne	0.534925	0.444434	-1.445590	0.321586	1.044600	0.208558	0.021932	0.154759
^{30}Ne	1.282130	0.406850	-2.027370	0.345858	0.896827	0.195033	0.000000	0.030000
^{31}Ne	2.315910	0.197503	-5.558160	0.185995	4.149540	0.157223	-0.758952	0.120720
^{32}Ne	0.003830	0.189152	-1.065860	0.179841	1.188140	0.153931	0.000000	0.030000
^{27}Na	1.183950	0.411054	-3.321220	0.316098	2.314640	0.243068	-0.029623	0.227835
^{28}Na	2.321510	0.421160	-5.709710	0.335278	3.554250	0.265758	0.000000	0.030000
^{29}Na	0.239708	0.388324	-0.802123	0.256835	0.650921	0.157863	0.000000	0.030000
^{30}Na	0.561915	0.480679	-1.745900	0.318521	1.341390	0.215486	0.000115	0.185528

Table 5.3 continued.

Nuclei	RMF(NL3*)							
	c_1	a_1	c_2	a_2	c_3	a_3	c_4	a_4
^{31}Na	0.542793	0.439562	-1.638870	0.302712	1.283420	0.200706	-0.035750	0.133745
^{32}Na	0.561751	0.485240	-1.603180	0.317622	1.197570	0.203570	0.000000	0.030000
^{33}Na	2.893490	0.379239	-6.594020	0.305261	4.006570	0.240770	-0.136028	0.224166
^{34}Na	-0.137022	0.246391	-0.452815	0.246355	0.721347	0.163341	0.000000	0.030000
^{35}Na	0.141220	0.431829	-0.588160	0.239005	0.577609	0.141785	0.000000	0.030000
^{30}Mg	2.592090	0.407323	-6.103830	0.326123	3.790990	0.256545	-0.115072	0.238768
^{31}Mg	2.137760	0.389179	-5.182640	0.311005	3.297420	0.243035	-0.096175	0.228525
^{32}Mg	4.193560	0.345609	-7.645820	0.302216	3.956090	0.237521	-0.353128	0.237521
^{33}Mg	1.961810	0.363766	-4.282170	0.296226	2.612760	0.222400	-0.143600	0.222408
^{34}Mg	0.813743	0.464905	-2.161670	0.312644	1.513220	0.208441	0.000069	0.177941
^{35}Mg	3.488430	0.369219	-7.688960	0.300122	4.561640	0.237748	-0.191473	0.220351
^{36}Mg	3.546130	0.363071	-7.832630	0.294805	4.640730	0.234024	-0.182660	0.217145
^{37}Mg	0.864970	0.433936	-2.269340	0.294619	1.572890	0.198338	0.000000	0.030000
^{38}Mg	2.910640	0.350318	-6.738170	0.280814	4.104570	0.222018	-0.110774	0.207592
^{39}Mg	2.640130	0.343501	-6.175710	0.274174	3.786750	0.215309	-0.088951	0.199509
^{40}Mg	2.385150	0.336466	-5.781450	0.266383	3.555790	0.209767	0.000000	0.073830
^{41}Mg	2.153980	0.331553	-5.275180	0.261021	3.279330	0.203834	0.000000	0.030000
^{42}Mg	1.938140	0.327965	-4.772760	0.256332	2.992860	0.197894	0.000000	0.030000
^{33}Al	2.005900	0.375802	-4.914680	0.299067	3.150890	0.232168	-0.091960	0.218638
^{34}Al	7.762070	0.323392	-16.180000	0.287326	9.018520	0.248662	-0.452489	0.242904
^{35}Al	3.484320	0.370436	-8.038710	0.300560	4.832770	0.241557	-0.119586	0.228814
^{36}Al	0.891789	0.454546	-2.338640	0.305996	1.611340	0.204934	0.000000	0.030000
^{37}Al	3.884590	0.359287	-8.841610	0.292045	5.243580	0.235974	-0.118830	0.224414
^{38}Al	3.760320	0.352084	-8.449800	0.286205	5.006760	0.229599	-0.150074	0.215421
^{39}Al	3.543200	0.344582	-7.835530	0.279981	4.641770	0.222093	-0.184226	0.205731
^{40}Al	0.854275	0.411033	-2.257100	0.278476	1.565890	0.187427	0.000000	0.030000
^{41}Al	2.877830	0.330120	-6.805090	0.263819	4.089220	0.210281	0.000000	0.033399
^{42}Al	2.697300	0.324321	-6.411290	0.258267	3.875160	0.204892	0.000000	0.030000
^{43}Al	2.534430	0.319182	-6.040730	0.253241	3.667260	0.199791	0.000000	0.030000
^{44}Al	3.087180	0.330131	-7.302840	0.263807	4.389470	0.210285	0.000000	0.030000

Table 5.4 Same as Table 5.2, but for fourth order Gaussian fit (4G) with SHF(SkI4) density.

	SHF(SkI4)							
Nuclei	c_1	a_1	c_2	a_2	c_3	a_3	c_4	a_4
^{12}C	-25.801500	0.252892	-49.227300	0.215881	56.665600	0.236500	18.552300	0.202810
^{19}C	-0.226211	0.299254	-0.114207	0.097847	0.447605	0.169972	0.0398298	0.0703083
^{20}C	-0.232117	0.293723	-0.122644	0.098025	0.463115	0.170387	0.046864	0.071331
^{21}C	-0.302393	0.282487	-0.148184	0.104159	0.557232	0.176980	0.056439	0.075738
^{22}C	-6.643380	0.197106	-11.376500	0.151124	13.923900	0.176027	4.270630	0.136185
^{21}N	-1.845150	0.245293	-0.743545	0.181219	2.736740	0.209226	0.000000	0.030000
^{22}N	-1.796270	0.243308	-0.658633	0.182587	2.616140	0.209113	0.000000	0.030000
^{23}N	-1.662900	0.239979	-0.445581	0.185288	2.283860	0.209246	0.000000	0.030000
^{20}O	-0.628418	0.286684	-0.134859	0.138100	0.897160	0.196344	0.000000	0.030000
^{21}O	-0.826759	0.276995	-0.201911	0.147402	1.165250	0.200196	0.000000	0.030000
^{22}O	-1.237710	0.266166	-0.377416	0.160890	1.753590	0.205594	0.000000	0.030000
^{23}O	-1.013220	0.260477	-0.280076	0.153587	1.448410	0.198290	0.000000	0.030000
^{24}O	-0.801810	0.256267	-0.175417	0.145888	1.146280	0.191887	0.000000	0.030000
^{23}F	-0.000183	0.295357	-0.763064	0.255010	1.101850	0.178905	-0.205427	0.127628
^{24}F	0.217542	0.500482	-0.807710	0.327402	0.834852	0.193120	-0.094997	0.139076
^{25}F	0.649642	0.407248	-1.789460	0.310774	1.371910	0.221816	-0.068778	0.192389
^{26}F	0.246640	0.472505	-0.825964	0.311172	0.806916	0.186801	-0.068934	0.139147
^{27}F	0.261834	0.458652	-0.850890	0.301849	0.814869	0.181394	-0.069720	0.135323
^{28}F	0.282971	0.454978	-0.904170	0.299885	0.844714	0.180747	-0.069102	0.135687
^{29}F	1.059410	0.384744	-1.825510	0.321458	0.923511	0.194300	0.000000	0.030000
^{28}Ne	0.006036	0.211948	-1.165500	0.206471	1.298620	0.177349	0.000000	0.030000
^{29}Ne	1.420600	0.204901	-3.359860	0.190769	2.892990	0.149851	-0.796177	0.117933
^{30}Ne	-0.117584	0.231704	-0.098982	0.161911	0.559820	0.170389	0.000000	0.030000
^{31}Ne	0.136515	0.487488	-1.389480	0.231714	1.395830	0.184371	0.000000	0.030000
^{32}Ne	0.471702	0.388370	-0.756438	0.318318	0.420274	0.140182	0.000000	0.030000
^{27}Na	0.083718	0.633751	-2.191540	0.235067	2.252030	0.207011	0.000000	0.030000
^{28}Na	0.478022	0.395037	-1.384910	0.276194	1.282490	0.176424	-0.224057	0.132140
^{29}Na	0.337217	0.426713	-1.027910	0.280497	1.005680	0.166452	-0.159804	0.118986
^{30}Na	0.367982	0.427453	-1.113110	0.281583	1.067450	0.167507	-0.168258	0.119915

Table 5.4 continued.

Nuclei	SHF(SkI4)							
	c_1	a_1	c_2	a_2	c_3	a_3	c_4	a_4
^{31}Na	9.447780	0.293228	-21.261700	0.262587	16.695700	0.226641	-4.723580	0.205619
^{32}Na	0.398942	0.389093	-1.820500	0.247198	1.564150	0.189809	0.000000	0.030000
^{33}Na	0.037784	0.733888	-1.051430	0.196836	1.147890	0.160184	0.000000	0.030000
^{34}Na	0.038891	0.674753	-1.150430	0.187510	1.244560	0.155985	0.000000	0.030000
^{35}Na	0.040233	0.617685	-1.076990	0.181637	1.168470	0.150003	0.000000	0.030000
^{30}Mg	0.967548	0.350427	-2.536880	0.263149	2.199210	0.182389	-0.474243	0.143552
^{31}Mg	1.238090	0.343206	-3.178720	0.262964	2.694200	0.186790	-0.599204	0.149237
^{32}Mg	2.313760	0.322990	-5.640500	0.261879	4.629150	0.198944	-1.147040	0.166131
^{33}Mg	6.462870	0.233913	-15.784600	0.216738	9.454370	0.200598	0.000000	0.030000
^{34}Mg	0.216805	0.393300	-2.369690	0.207825	2.288960	0.178953	0.000000	0.030000
^{35}Mg	0.096001	0.485277	-1.320150	0.198622	1.357990	0.161544	0.000000	0.030000
^{36}Mg	0.324293	0.325122	-2.423400	0.197739	2.232310	0.168501	0.000000	0.030000
^{37}Mg	0.059670	0.528715	-1.474690	0.180731	1.547550	0.153708	0.000000	0.030000
^{38}Mg	0.097497	0.395723	-1.196830	0.186923	1.231510	0.149797	0.000000	0.030000
^{39}Mg	0.101680	0.391614	-1.825450	0.178964	1.856440	0.154070	0.000000	0.030000
^{40}Mg	0.056251	0.499351	-1.156400	0.179242	1.232490	0.145261	0.000000	0.030000
^{41}Mg	0.093914	0.389983	-1.730400	0.174947	1.769490	0.149466	0.000000	0.030000
^{42}Mg	0.078809	0.395136	-1.561610	0.171561	1.615540	0.145203	0.000000	0.030000
^{33}Al	2.531400	0.320178	-6.151030	0.259487	5.128940	0.196453	-1.351960	0.163673
^{34}Al	0.245609	0.495687	-1.051060	0.267794	0.948977	0.174783	0.000000	0.030000
^{35}Al	0.102819	0.572296	-2.491920	0.202198	2.527940	0.178740	0.000000	0.030000
^{36}Al	0.098348	0.559208	-2.427870	0.195144	2.466830	0.172634	0.000000	0.030000
^{37}Al	0.101511	0.531377	-1.483640	0.197049	1.518030	0.161708	0.000000	0.030000
^{38}Al	0.080294	0.570367	-2.332850	0.184932	2.388930	0.164002	0.000000	0.030000
^{39}Al	0.062912	0.595526	-2.145200	0.181262	2.218630	0.160013	0.000000	0.030000
^{40}Al	0.056326	0.607024	-2.047970	0.178108	2.127670	0.156679	0.000000	0.030000
^{41}Al	0.061514	0.581649	-2.185630	0.177146	2.260300	0.156422	0.000000	0.030000
^{42}Al	0.148271	0.378527	-2.026860	0.184237	2.013920	0.156485	0.000000	0.030000
^{43}Al	0.153818	0.364136	-1.404150	0.189083	1.386490	0.149031	0.000000	0.030000
^{44}Al	0.053388	0.339712	-0.427454	0.219687	0.505891	0.122631	0.000000	0.030000

In general view, we have realized from both the figures and conclude that both fittings 2G and 4G densities could reproduce the RMF and SHF densities. Whereas a deeper inspection suggests that the 2G fitting is marginally better at the tail part and 4G fit appears superior at the center region. The role of these densities in terms of the Gaussian coefficients can be analyzed through the reaction dynamics. These results have been described in the next section.

5.3 Reaction cross section (σ_R) with 2G and 4G fitted parameters

In this section, an effort has been made to study the reaction dynamics of light mass nuclei from β-stability line to drip line, using the well known Glauber formalism. The densities from microscopic relativistic mean field (RMF) and non-relativistic mean field (SHF) are used. The densities of these mean field formalisms are converted in terms of Gaussian coefficients as discussed in the previous section. The value of n is determined by comparing the fitted density with the actual RMF and SHF densities. The results of our calculations by using fitted densities are given in Table 5.5 and Figure's $(5.4 - 5.7)$.

Figure 5.4 presents the variation of a total nuclear reaction cross section for ^{12}C+^{12}C as a function of the projectile energy. The RMF(NL3*) and SHF(SkI4) densities are used while evaluating reaction cross sections (σ_R). The results obtained from the two Gaussian (2G) and four Gaussian (4G) fit are shown in this figure. The experimental data is also given for comparison [9, 10]. We find reasonable results using all the simulated densities. A further inspection of this figure signifies that σ_R obtained from RMF density is more close to the experimental values. In overview, the figure signifies that the result obtained from the 2G RMF (NL3*) density is better than other considered cases. For more con-

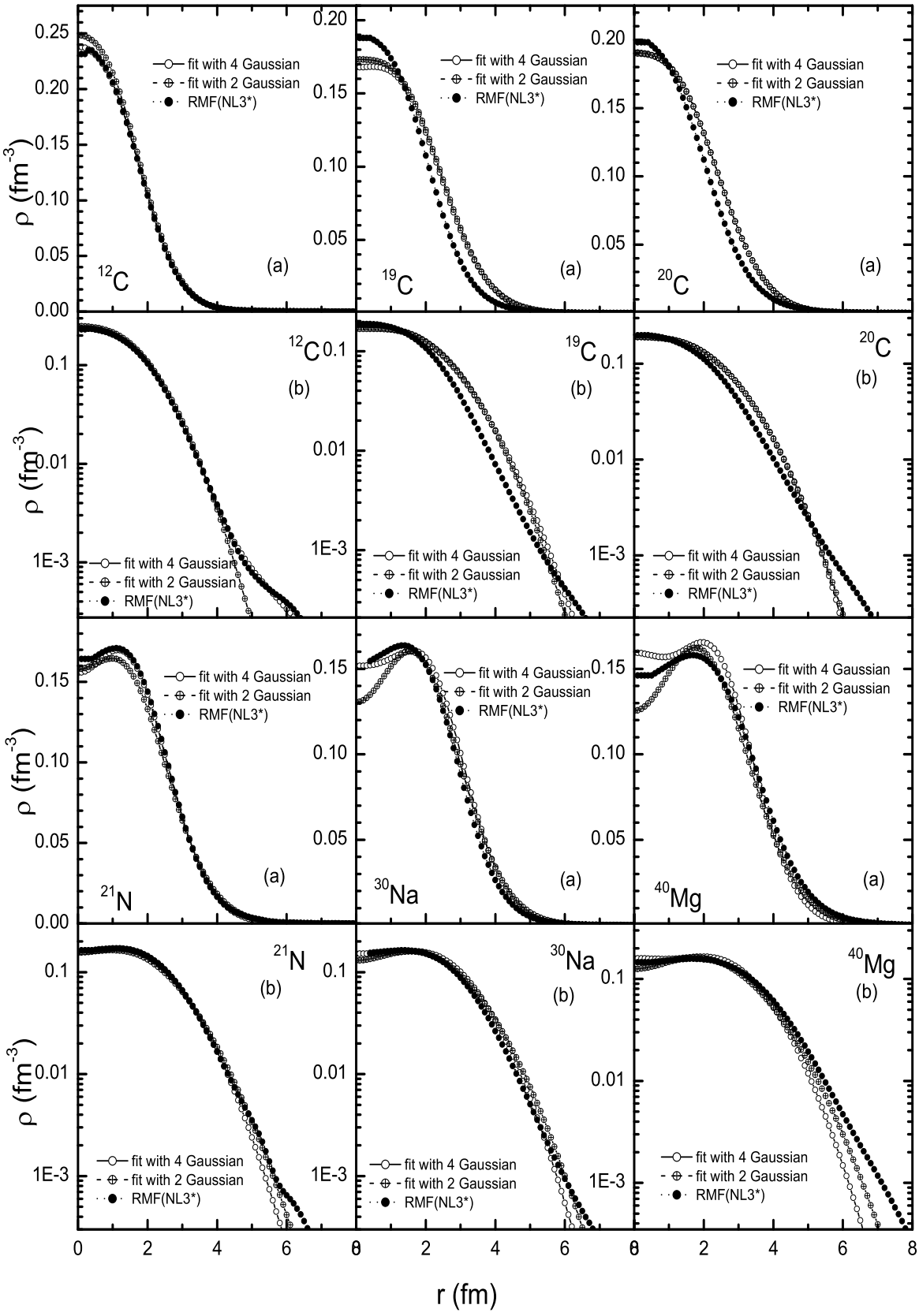

Figure 5.2 The RMF radial densities compared for ^{12}C, ^{19}C, ^{20}C, ^{21}N, ^{30}Na and ^{40}Mg isotopes with 2-Gaussian (2G) and 4-Gaussian (4G) fitted densities.

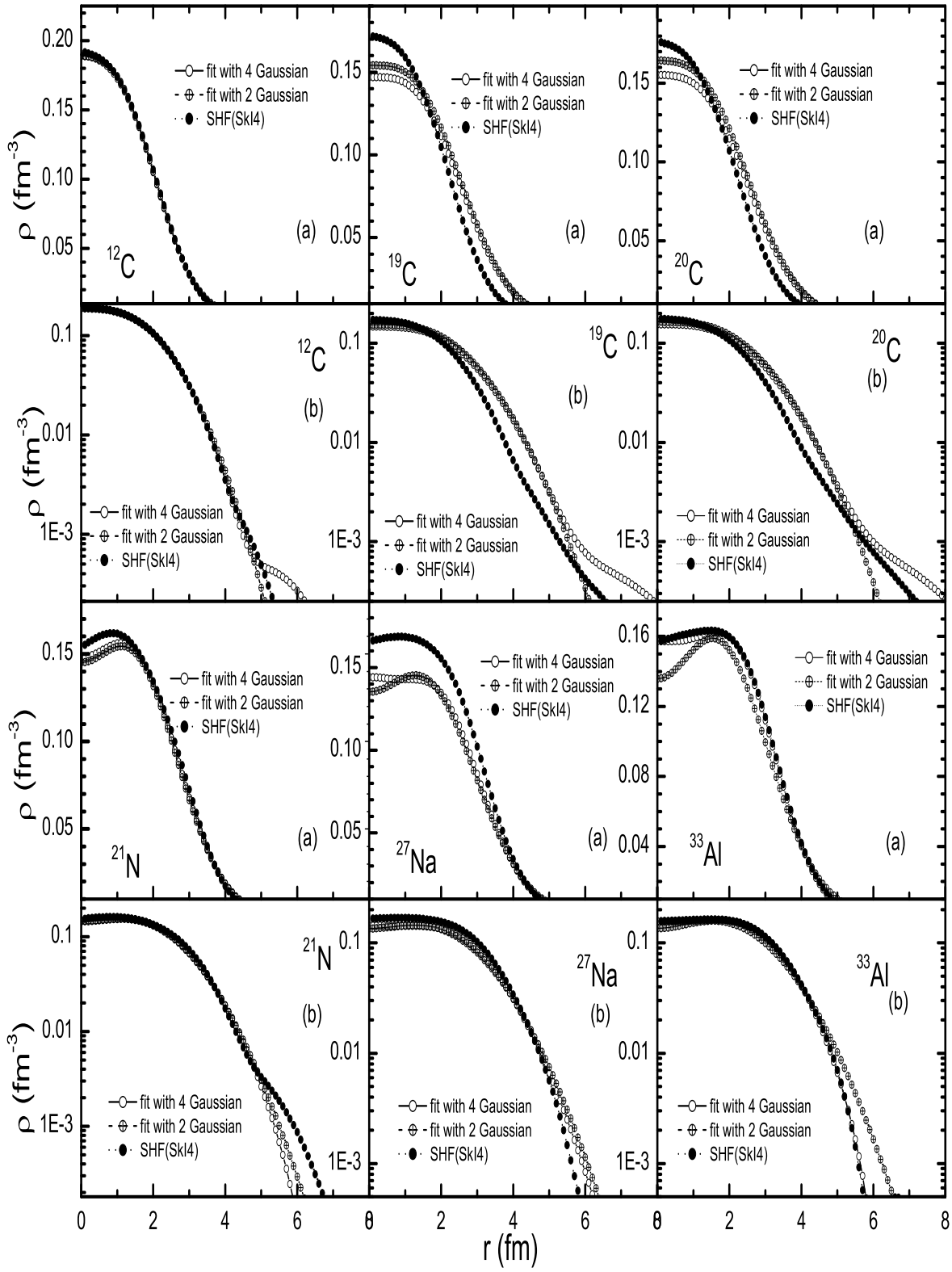

Figure 5.3 Same as figure 5.2 with same set of isotopes, but for SHF densities.

Table 5.5 Total nuclear reaction cross section with various projectiles over ^{12}C target. The experimental data are also given for comparison.

Projectile	Energy (MeV/nucleon)	$\sigma_R(mb)$ RMF(NL3*) (2G)	RMF(NL3*) (4G)	SHF(SkI4) (2G)	SHF(SkI4) (4G)	Expt. [11–16]
^{19}C	960	1228	1344	1345	1488	1231±28
^{20}C	905	1247	1333	1358	1537	1187±20
^{21}N	1005	1237	1347	1329	1311	1114±09
^{22}N	965	1244	1373	1334	1341	1245±49
^{23}N	920	1288	1415	1349	1379	1399±98
^{21}O	980	1193	1305	1321	1266	1098±11
^{22}O	900	1222	1336	1311	1282	1123±24
^{22}O	965	1221	1336	1310	1281	1172±22
^{23}O	900	1252	1373	1336	1321	1216±41
^{23}O	960	1252	1373	1336	1321	1308±16
^{24}O	965	1286	1444	1365	1367	1318±52
^{23}F	1020	1247	1435	1404	1287	1148±16
^{24}F	1005	1274	1404	1420	1348	1253±23
^{25}F	1010	1309	1440	1440	1414	1298±31
^{26}F	950	1348	1468	1499	1452	1353±54
^{28}Ne	240	1346	1395	1486	1468	1273±11
^{29}Ne	240	1342	1425	1465	1213	1344±14
^{30}Ne	240	1352	1456	1438	1377	1348±17
^{31}Ne	240	1434	1353	1563	1501	1435±22
^{32}Ne	240	1536	1660	1568	1600	1385±33
^{28}Ne	950	1458	1522	1609	1593	1244±40
^{29}Ne	950	1452	1554	1585	1299	1279±32
^{27}Na	950	1447	1486	1606	1516	1229±18
^{28}Na	950	1465	1476	1621	1464	1265±10
^{29}Na	950	1503	1723	1635	1471	1281±22
^{30}Na	950	1505	1576	1632	1485	1318±15
^{31}Na	950	1483	1583	1583	1524	1358±41
^{32}Na	950	1573	1609	1720	1632	1395±61
^{32}Mg	900	1515	1592	1627	1519	1331±24
^{33}Mg	900	1541	1622	1744	1676	1320±23
^{34}Mg	900	1657	1637	1843	1721	1372±46
^{35}Mg	900	1706	1640	1913	1777	1472±70

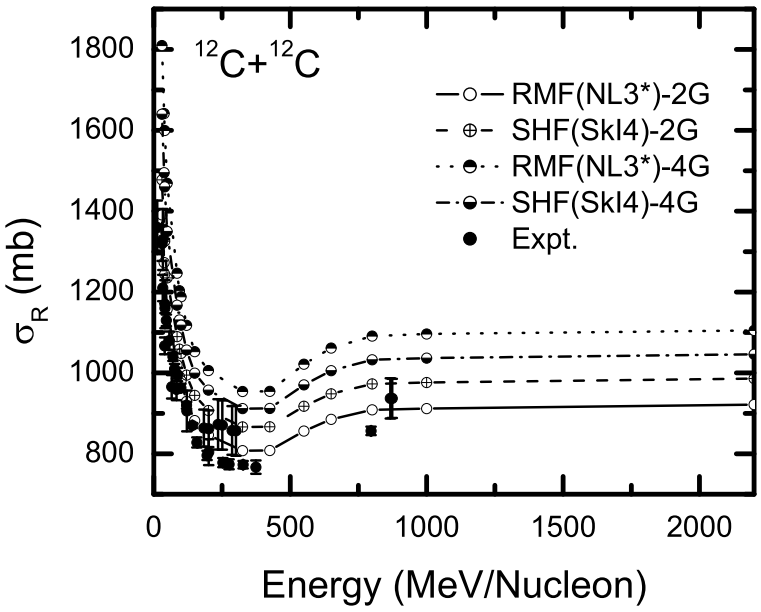

Figure 5.4 The total nuclear reaction cross section (σ_R) as a function of kinetic energy of projectile. The results obtained from RMF(NL3*) and SHF(SkI4) densities are compared with available experimental data [9, 10].

cluding remarks on this study, we have extended our calculations by estimating the total reaction cross sections 'σ_R' for light mass systems. Table 5.5 shows the total nuclear reaction cross sections for the isotopes of C, N, O, F, Ne, Na and Mg nuclei using RMF and SHF densities using 2G and 4G coefficients. The available experimentally measured σ_R of these nuclei are also listed in the last column of the table for comparison. The comparison between our theoretical calculations and the experimental data reveals that the calculated values agree well with the experimental data [11–16]. However a close observation seems to suggest that a slight overestimation is recorded for the C, N, O and F isotopes and some higher mass isotopes of Ne, Na and Mg nuclei. The σ_R obtained with the 4G coefficients for RMF densities are slightly higher than with the 2G coefficients whereas in case of SHF densities, the reaction cross sections obtained by the 4G coefficients are slightly lesser than the 2G coefficients. The superiority of the (2G) RMF coefficients still seems visible here as well. After this concluding analysis, we tried to investigate the dependence

of projectile energy (E_{proj}) on σ_R.

Figure's 5.4-5.7 show the variation of σ_R as a function of energy of the projectile E_{proj}. The calculations are made over a broad energy range from 30 MeV/nucleon-2200 MeV/nucleon of projectile. The values of σ_R are observed to be larger at a small incident energy and starts decreasing with the increase in E_{proj} up to $\sim$ 300 MeV/nucleon. A slight variation (increase) in σ_R appears within $300 - 750$ MeV/nucleon and it remains unchanged above to the energy 750 MeV/nucleon. A similar kind of trend is obtained for the isotopes of $^{27-35}$Na, $^{30-42}$Mg and $^{33-44}$Al nuclei in Figures's 5.5, 5.6 and 5.7.

In Fig. 5.5, we observe that the value of reaction cross section obtained from the non-relativistic density is slightly larger than the relativistic case for the 2G coefficients. A reverse effect is seen while taking the 4G fitted densities. This may be due to the reason of a better fitting of the 2 Gaussian, as discussed earlier. On another view, reaction cross section σ_R increases with the isotopic mass for both the densities. While changing the mass of the projectile from ^{34}Na to ^{35}Na, an abrupt variation in σ_R is seen in 2G RMF(NL3*) case. This may be correlated with the large quadrupole deformation of these nuclei. The quadrupole deformation parameter β_2 for ^{34}Na and ^{35}Na are 0.392 and 0.437 respectively. Because of such well deformed cases, the fitting with 2G or 4G may not be a proper approximation and needs an improvement in the density profile. This manifests a small gap in the 4G fitting (see Fig. 5.5).

Fig. 5.6 shows the variation of total reaction cross sections for Mg projectiles. Similar to the case of Na, the value of σ_R increases in the isotopic chain. It is observed from the figure that σ_R of ^{32}Mg is smaller than the nearby higher isotopes for both 2G (RMF & SHF) mean field density. The gap between the total reaction cross section for ^{33}Mg and ^{34}Mg is larger as compared to other isotopes of 2G RMF. The β_2 for ^{33}Mg and ^{34}Mg are 0.003 and 0.312 respectively. This is a clear effect of the deformation but the results show

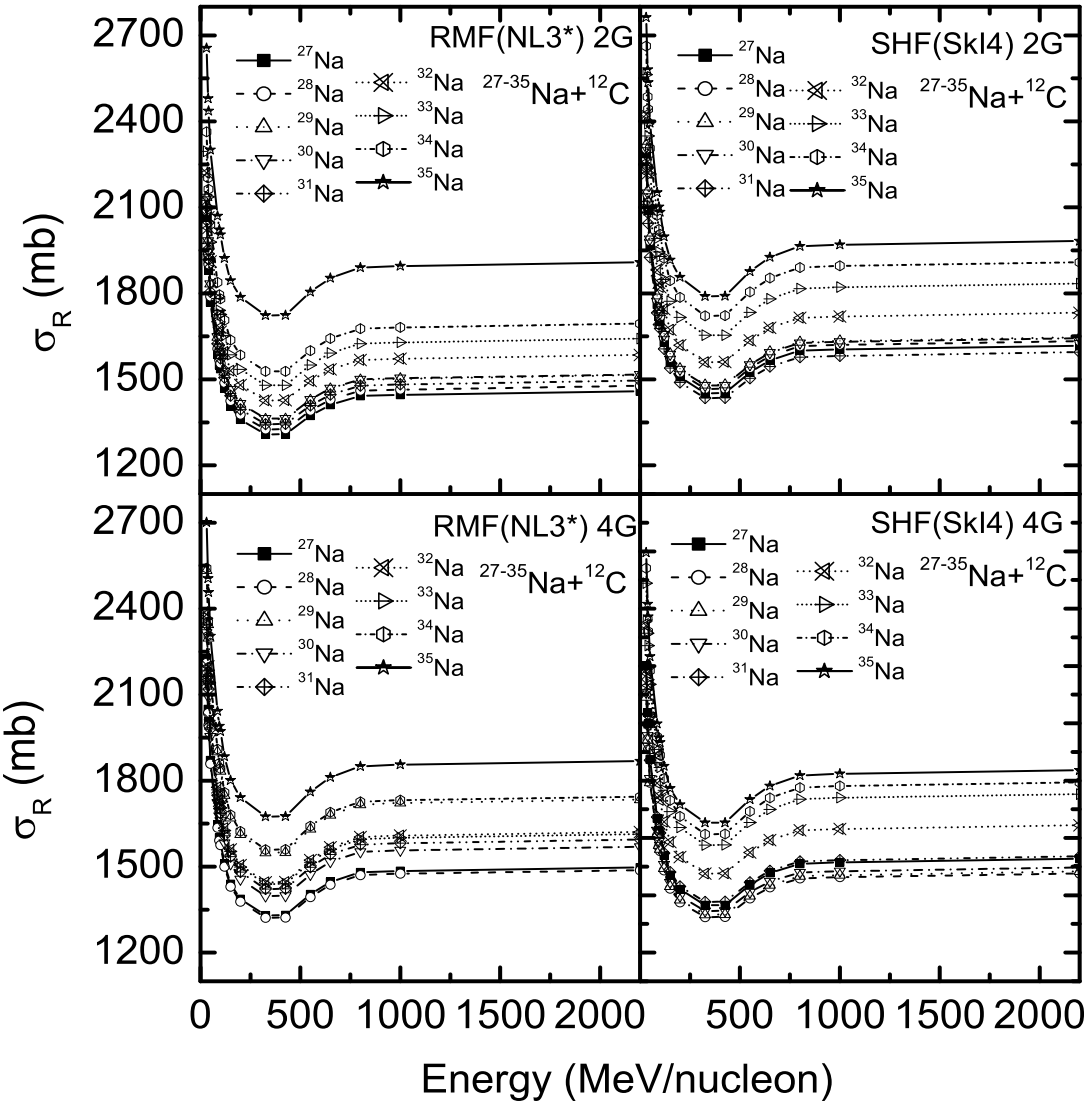

Figure 5.5 Variation of reaction cross section with projectile energy (E_{Proj}) for the Na-isotopes with ^{12}C target.

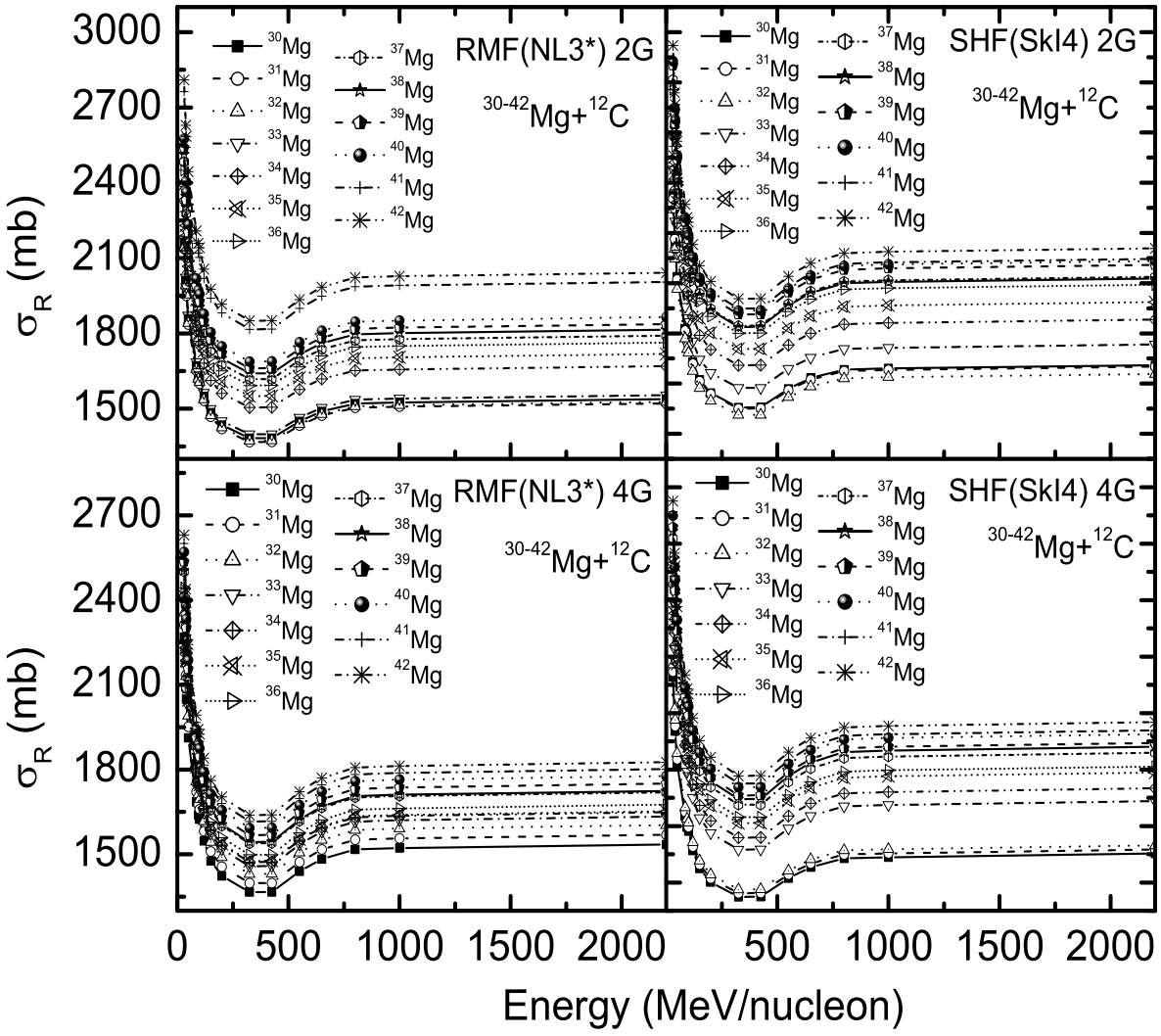

Figure 5.6 Same as figure 5.5, but for Mg-isotopes.

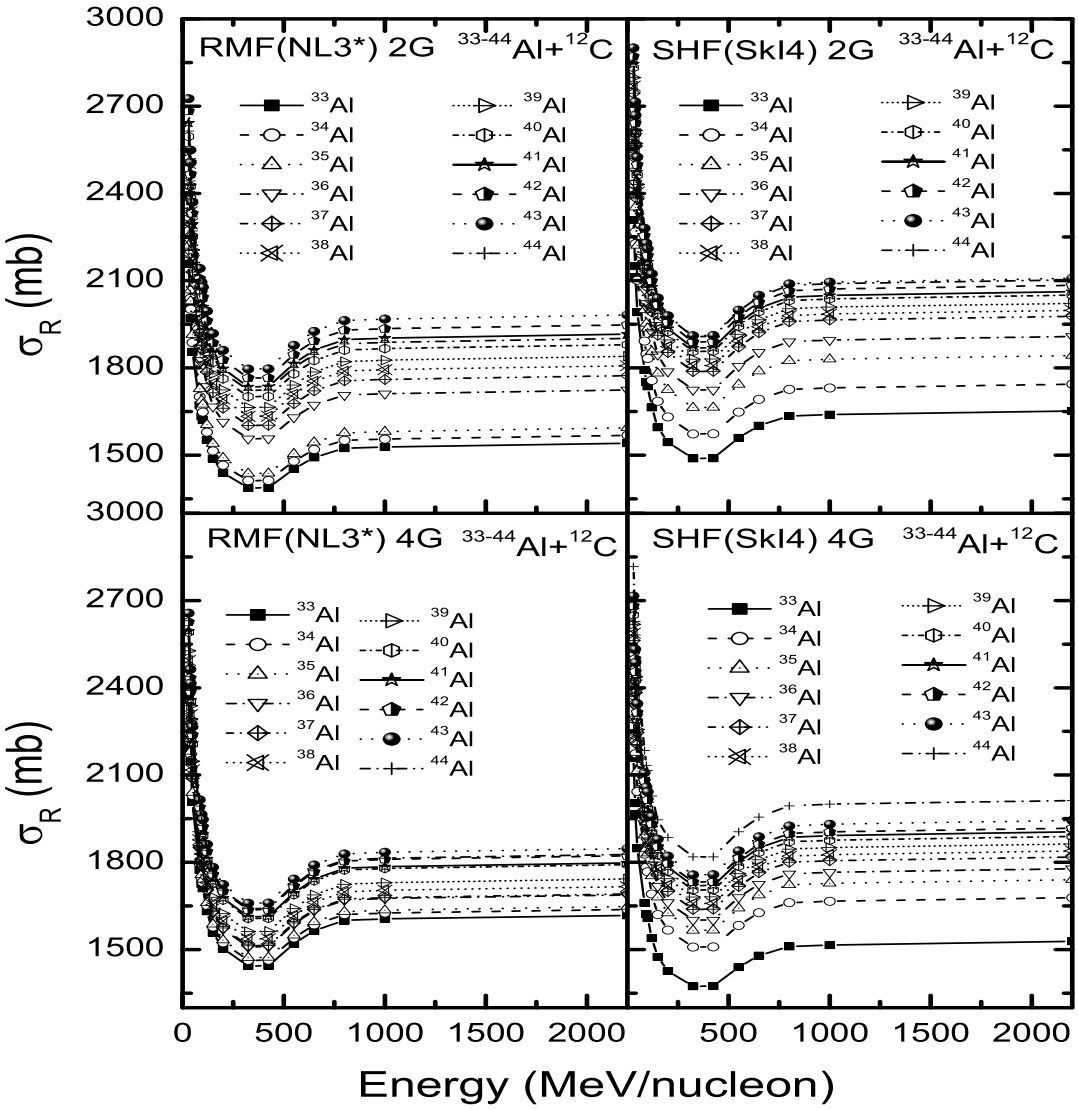

Figure 5.7 Same as figure 5.5, but for Al-isotopes.

contrast behavior between 2G (RMF) and 4G (RMF) of the Gaussian fitting . Similarly a large gap is seen for ^{32}Mg and ^{33}Mg isotopes in 4G SHF densities, with β_2 are 0.053 and 0.223 respectively for ^{32,33}Mg.

Fig. 5.7 shows the σ_R results for $^{33-44}$Al as a function of the projectile energy E_{proj}. The calculated σ_R with RMF densities are slightly smaller than the non-relativistic SHF calculations. The theoretical gap in σ_R is larger between ^{35}Al and ^{36}Al with 2G fitting corresponding to the deformation 0.204 and 0.303 for ^{35,36}Al, respectively. The total nuclear reaction cross sections are also smaller for ^{44}Al as compared to the value of ^{43}Al in both

the RMF (2G & 4G) cases. The deformation parameters for these nuclei are 0.457 and 0.220, showing similar structure effect of Na and Mg isotopes. The large gap appeared in ^{33}Al and ^{34}Al for 4G SHF density could be the structural manifestation whose β_2 values are 0.044 and 0.161 for ^{33,34}Al.

Another effect which appeared in the densities profile is the bubble effect. Detail investigation of such an effect is given in the previous chapter 4. In order to have a glance at the role of the bubble structure on the reaction cross section, we compared the depletion factor (D.F.) for some nuclei from Table 4.1 with the values of σ_R of Table 5.5. From this comparison we concluded that, the formation of bubble is related to the structure effect at the center of the nucleus. However, the reaction cross section is mostly a surface phenomenon. Thus the σ_R depends much on the tail part of the density. In other words, one can say that the reaction cross section is independent of the bubble effect, which is also evident from our results.

In above study, we observed that the deformation or structure of the projectile nuclei plays an important role in the reaction dynamics. To see the structure effect on σ_R specifically, we have calculated the total reaction cross sections for ^{19}C+^{12}C at projectile energy 960 MeV/nucleon. The results are presented in Table 5.6. In these calculations, we took the spherical target with the prolate deformed (β_2=0.354) projectile density. The reaction cross section is found to be 1228 mb with 2G RMF. Again with oblate deformation (β_2=-0.442) the value of σ_R = 1128 mb with the same 2G RMF density. These values are 1344 mb and 1096 mb with 4G RMF for prolate and oblate densities, respectively. This difference in the reaction cross section is a manifestation of the structure of the nucleus. The above study encouraged us to see the effect of deformation in the reaction cross sections. This study has been undertaken in the present work and a brief description is given in the subsequent section.

Table 5.6 Total reaction cross sections for deformed ^{19}C projectile over ^{12}C target with different values of deformation.

$E_{Proj.}$ (MeV/nucleon)	β_2	$\sigma_R(mb)$ RMF(NL3*) (2G)	(4G)	Expt. [13]
960	0.354	1228	1344	1231±28
960	-0.442	1128	1096	1231±28

5.4 Role of deformed densities in reaction dynamics

In view of present day developments, it becomes highly essential to investigate the role of deformed structure of the nucleus in the reaction dynamics. It is so because the collisions between the deformed nuclei have been of huge interest during a last few decades. It is evident from literature that the deformation effects play a significant role in the better description of the nuclear reaction dynamics. Since most of the nuclei are deformed so the nuclear shapes play an important role in the formation as well as the decay process of a nuclear system. The quest regarding the shape of a nucleus fascinated the nuclear physics community for many years. Hence to see the role of deformed densities on σ_R, we took the densities from the spherical symmetric terminology for the nuclei. The same calculations are performed with the axially deformed formalism. Further for comparison between the relativistic and the non-relativistic mean field densities, same set of calculations are also performed for HF with newly developed simple effective interaction.

Role of the densities is first checked through the stable projectile with the stable target nuclei, which also depicts the validity of the Glauber model. First of all, we compared the reaction cross section σ_R obtained from the forces SEI-I, NL3 and NL-SH for ^{12}C+^{12}C with the experimental measurements in Figure 5.8. It is clear from the figure that, the calculated σ_R are quite sensitive to the density used. Even within the same interaction, it gives distinct results for the use of the spherical or deformed densities. The theoretical

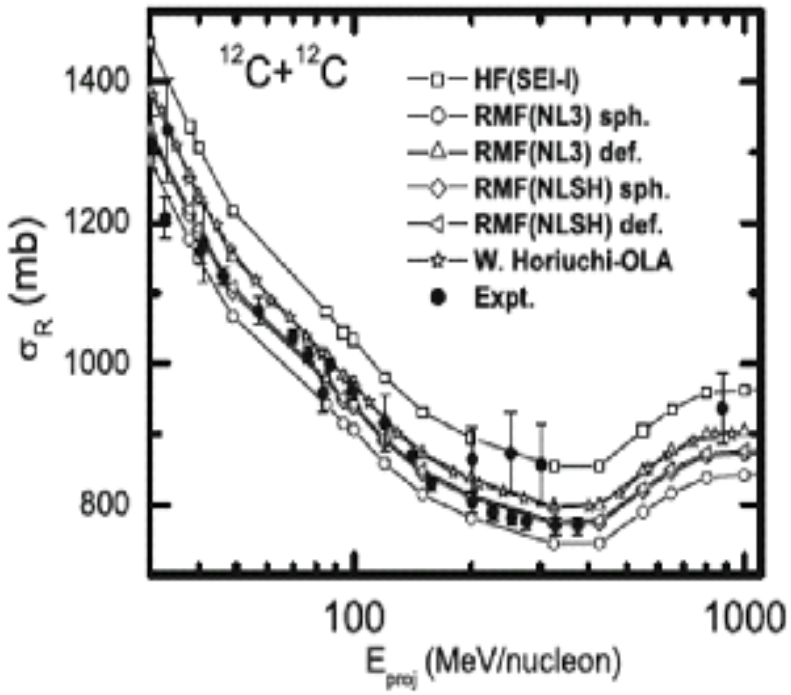

Figure 5.8 The nuclear reaction cross section (σ_R) obtained from various densities for ^{12}C+^{12}C reaction as a function of projectile energy. The available experimental data [9] are also given for comparison.

results of Horiuchi *et al.* [9] are also given in the figure for comparison. Our spherical RMF(NL3) results match well with the prediction of Ref. [9], but the deformed RMF(NL3) and spherical SEI-I slightly overestimate the data values. Here, it is worth mentioning that the experimental quadrupole deformation parameter of ^{12}C is about 0.58, which we do not get by using RMF or SEI parameterizations. We get $\beta_2 \sim -0.3$ in RMF(NL-SH) calculation. But the deformed solution of RMF(NL3) is slightly prolate, which may be the factor responsible for the deviation of RMF(NL3) results. For low energy region, the data and the prediction walk hand in hand confirming the applicability of the model. Again for the evaluation of σ_R using Glauber model, both the proton and the neutron density distributions are required as input. Thus, we can not verify the model by using the experimental density as the neutrons density distributions are not available experimentally.

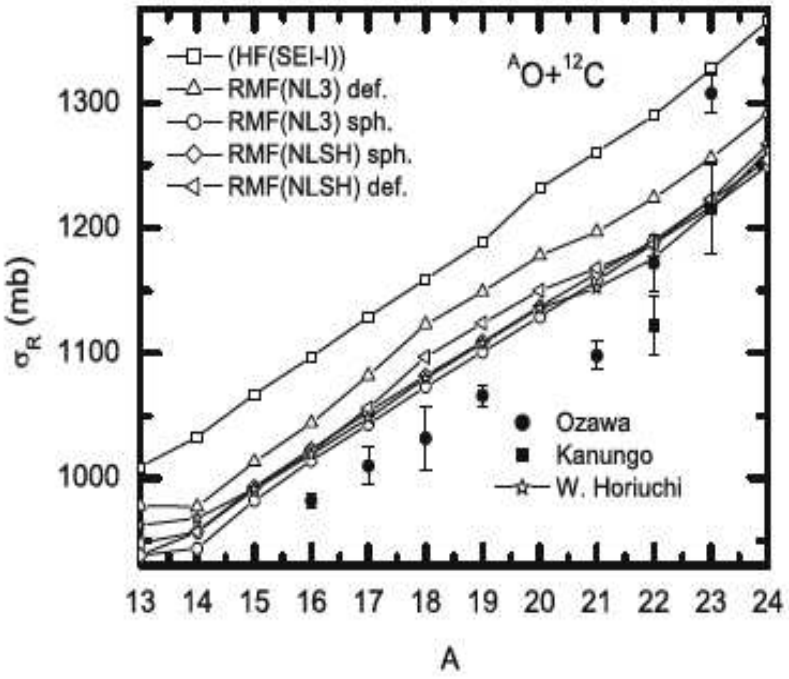

Figure 5.9 The nuclear reaction cross section (σ_R) with various densities as a function of mass number for O-isotopes with ^{12}C target. The experimental data Ozawa *et al.*, and Kanungo *et al.*, [13, 14] with theoretical prediction of Horiuchi *et al.*, [17] are given for comparison.

Also, we are unable to reproduce the large prolate deformed solution of ^{12}C using any of the RMF forces and it is beyond the scope for the present SEI model for deformed calculations. Therefore, we may have an impression that these factors of densities can not be overlooked while discussing the nuclear reaction cross section σ_R in the Glauber model. The oblate shape of NL-SH parameter set for ^{12}C may be able to compensate in some sense for these limitations to reproduce the experimental data of σ_R. Further, σ_R for ^{A}O+^{12}C with various RMF and HF(SEI-I) densities are depicted in Fig. 5.9 as a function of mass number 'A'. For comparison, the recently measured experimental data [13, 14] along with other theoretical estimations [17] are also included in this figure. As far as the experimental data is concerned, the prediction of σ_R by Horiuchi *et al.* [17] and spherical RMF (both NL3 and NL-SH) almost agree with each other. Also, the reaction cross sections obtained from the deformed NL-SH density agree well with the experimental estimations. Similar

to the case of ^{12}C+^{12}C, unlike to the NL-SH predictions, the deformed NL3 results slightly overestimate the experimental data as shown in figure. Here also the same arguments may hold good, as is discussed for ^{12}C+^{12}C to compare these with the reaction cross section. Further, in order to see the effect of the deformations on reaction dynamics from light mass to medium mass range, we have used the densities from spherically symmetric as well as deformed densities of the same set of projectiles. These results are also compared with the densities from newly developed SEI-I in HF formalism. The calculated values of σ_R for the considered nuclei using the HF(SEI-I), spherical and deformed RMF(NL3) densities are given in the Table 5.7. The calculated reaction cross sections are also compared with the experimental data [16,18–20]. One may clearly see from the table that the σ_R obtained from both the relativistic and non-relativistic formalisms are well compared with the experimental observations. We used the root mean square deviation or standard deviation (S.D) from the experimental observation to analyze the best densities. The general expression of (S.D) may be expressed as

$$S.D = \sqrt{\sum_{i=1}^{N} \frac{D_i^2}{N}} \tag{5.1}$$

$$D_i = (\sigma_R i(Obs) - \sigma_R i(Exp)). \tag{5.2}$$

The square of error of σ_R from the experimental values are also presented in the Table 5.7 for various densities. The values of $S.D$ for HF(SEI-I), spherical RMF(NL3) and deformed RMF(NL3) densities are 150.666, 78.584 and 97.438 respectively. The smallest value of $S.D$ for the spherical RMF(NL3) and deformed RMF(NL3) densities suggests that the σ_R obtained with the RMF density could reproduce better results as compared to the non-relativistic mean field densities. It may be noted that the σ_R values for ^{11}Be, ^{15}C, ^{19}C, ^{23}O

Table 5.7 The total nuclear reaction cross section (σ_R) and square of deviation (D_i) from experimental data (Expt.) for various projectiles with ^{12}C target using densities from HF(SEI), sph. RMF(NL3) and def. RMF(NL3). The experimental data [16, 18–20] of reaction cross sections are also given for comparison. The projectile energy is in MeV/nucleon.

Proj.	Energy	$\sigma_R(mb)$				D_i^2		
		HF(SEI-I) (Sph.)	RMF(NL3) (Sph.)	RMF(NL3) (Def.)	Expt.	HF(SEI-I) (Sph.)	RMF(NL3) (Sph.)	RMF(NL3) (Def.)
^{9}Be	790	857	810	844	806±9	2601	16	1444
^{10}Be	790	894	836	860	813±10	6561	529	2209
^{11}Be	790	942	890	902	942±8	0	2704	1600
^{12}Be	790	986	894	1004	927±18	3481	1089	5929
^{12}B	790	972	875	909	866±7	11236	81	1849
^{13}B	790	1012	916	960	883±14	16641	1089	5929
^{14}B	790	1049	951	1029	929±26	14400	484	10000
^{15}B	790	1086	991	1080	962±160	15376	841	13924
^{13}C	960	1005	901	931	862±12	20449	1521	4761
^{14}C	965	1003	944	978	880±19	15129	4096	9604
^{15}C	730	1065	959	1026	945±10	14400	196	6561
^{16}C	960	1113	1005	1084	1036±11	5929	961	2304
^{17}C	965	1147	1037	1117	1056±10	8281	361	3721
^{18}C	955	1182	1098	1150	1104±15	6084	36	2116
^{19}C	960	1215	1099	1120	1231±28	256	17424	12321
^{20}C	905	1271	1131	1179	1187±20	7056	3136	64
^{20}N	950	1239	1141	1174	1121±17	13924	400	2809
^{21}N	1005	1270	1172	1195	1114±9	24336	3364	6561
^{22}N	965	1306	1205	1278	1245±49	3721	1600	1089
^{23}N	920	1344	1240	1483	1399±98	3025	25281	7056
^{20}O	950	1233	1130	1179	1078±10	24025	2704	10201
^{21}O	980	1261	1158	1197	1098±11	26569	3600	9801
^{22}O	965	1291	1188	1225	1172±22	14161	256	2809
^{23}O	960	1327	1218	1257	1308±16	361	8100	2601
^{24}O	965	1367	1251	1292	1318±52	2401	4489	676
^{23}F	1020	1316	1211	1250	1148±16	28224	3969	10404
^{24}F	1005	1354	1242	1299	1253±23	10201	121	2116
^{25}F	1010	1393	1276	1363	1298±31	9025	484	4225
^{26}F	950	1434	1315	1388	1353±54	6561	1444	1225
^{28}Ne	240	1382	1272	1283	1273±11	11881	1	100
^{29}Ne	240	1417	1302	1340	1344±14	5329	1764	16
^{28}Ne	950	1497	1378	1391	1244±40	64009	17956	21609
^{29}Ne	950	1534	1410	1452	1279±32	65025	17161	29929
^{30}Ne	240	1454	1339	1401	1348±17	11236	81	2809
^{31}Ne	240	1481	1353	1408	1435±22	2116	6724	729
^{32}Ne	240	1509	1375	1417	1385±33	15376	100	1024
^{32}Mg	900	1613	1482	1545	1331±24	79524	22801	45796
^{32}Mg	950	1613	1482	1545	1340±24	74529	20164	42025
^{33}Mg	900	1641	1505	1538	1320±23	103041	34225	47524
^{34}Mg	900	1669	1526	1534	1372±46	88209	23716	26244
^{35}Mg	900	1697	1548	1553	1472±70	50625	5776	6561

and ^{31}Ne (all considered halo nuclei) are 942, 1065, 1215, 1327, 1481 mb with HF(SEI-I); 902, 1026, 1120, 1257, 1408 mb with deformed RMF(NL3); 890, 959, 1099, 1218, 1353 mb with spherical RMF(NL3) densities and 942±8, 945±10, 1231±28, 1308±16, 1435±22 mb from the experimental data. By a deep inspection of the Table 5.7, we easily concluded that the values of reaction cross sections obtained for halo systems (like ^{11}Be, ^{15}C, ^{19}C, ^{23}O, ^{31}Ne etc.) and other exotic nuclei show better results with deformed RMF(NL3) and HF(SEI-I) densities. Fig. 5.10 shows the total reaction cross sections of $^{9-12}$Be, $^{12-15}$B, $^{13-20}$C, $^{20-23}$N, $^{20-24}$O, $^{23-27}$F, $^{28-32}$Ne, $^{32-35}$Mg, $^{32-35}$Si, $^{34-37}$S and $^{34-48}$Ar nuclei as a function of the projectile energy (E_{proj}) over the energy range 30-1000 MeV/nucleon. The behavior of σ_R usually exhibits the similar pattern as we analyzed earlier in the previous subsection. The σ_R is higher at small E_{proj} and start decreasing upto the energy range of 300 MeV/nucleon. Small enhancement in σ_R is observed near 750 MeV/nucleon and after that it remains constant. The values of σ_R obtained from the HF(SEI-I) densities are slightly higher than the other densities (see Table 5.7). The reaction cross sections σ_R also increase by equal proportion in their isotopic chain with mass number 'A' for both HF(SEI-I) and RMF(NL3) spherical densities. However, some disorder is recorded in the enhancement for σ_R for deformed RMF(NL3) densities. This effect also justifies the importance of the deformation effects in the reaction dynamics.

5.5 Summary

In this chapter, we have done a systematic study of the reaction dynamics from light to medium mass region using the Glauber model within an optical limit approximation. The accuracy of the Glauber model is based on the density distribution of projectile and target nuclei. Therefore microscopic mean field densities have been used in terms of the

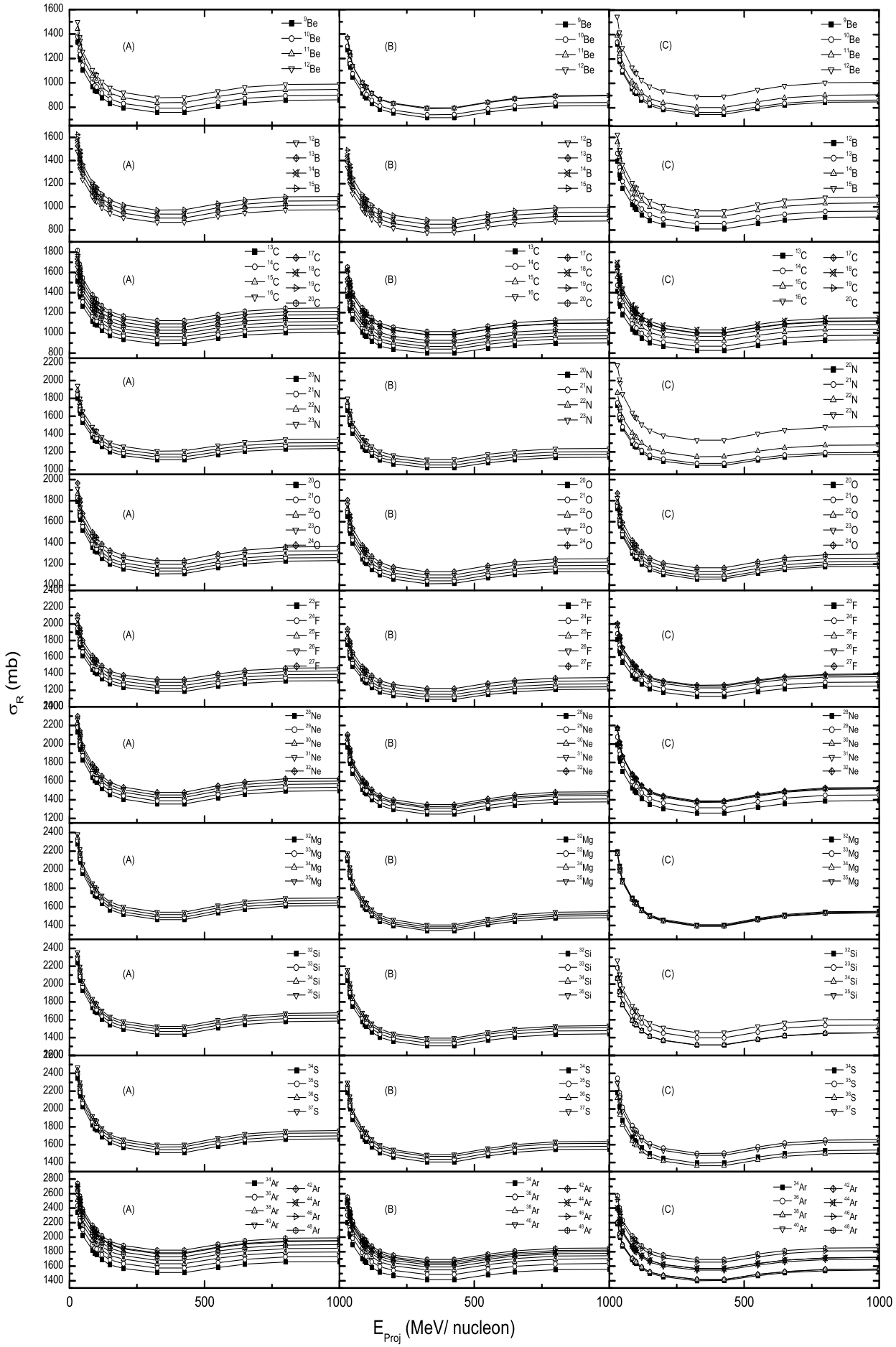

Figure 5.10 Variation of total reaction cross sections (σ_R) as a function of projectile energy (E_{proj}) using (A) HF(SEI-I), (B) sph. RMF(NL3), (C) def. RMF(NL3) densities for $^{9-12}$Be, $^{12-15}$B, $^{13-20}$C, $^{20-23}$N, $^{20-24}$O, $^{23-27}$F, $^{28-32}$Ne, $^{32-35}$Mg, $^{32-35}$Si, $^{34-37}$S and $^{34-48}$Ar nuclei. Here ^{12}C is used as target nucleus.

Gaussian coefficients in the Glauber formalism. First of all, the sensitivity of converted Gaussian densities are tested for some isotopes ^{12}C, ^{19}C, ^{20}C, ^{21}N, ^{27}Na and ^{33}Al. as test cases using both relativistic and non-relativistic densities. In this analysis we find the 2G fitting is better than the 4G fitting for RMF formalism, whereas a reverse trend seems evident for the SHF formalism. After that, the role of the fitting of densities as 2 Gaussian and 4 Gaussian form is studied on the reaction cross sections of various colliding systems. These calculations seem to suggest the superiority of 2G RMF densities over all the rest cases of the density distribution. The availability of the scattering/reaction data near the drip-line enhances our interest and encourages us to investigate the reaction dynamics of such nuclei. As most of the nuclei near the drip-line are deformed systems, henceforth the role of the deformation is also analysed through an investigation of the reaction cross sections, by feeding spherical RMF densities and deformed RMF densities.

In general, we observed that both the densities are capable of reproducing reasonable results, with the edge of RMF densities over non-relativistic mean field densities. The deformation or deformed structure effects the reaction dynamics significantly, so such effects need to be incorporated for having better understanding of the dynamics involved.

Bibliography

[1] M. E. Brandan and G. R. Satchler, Phys. Rep. **285**, 143 (1997), and references therein.

[2] P. R. Christensen and A. Winther, Phys. Lett. B **65**, 19 (1976).

[3] C. P. Silva *et al.*, Nucl. Phys. A **679**, 287 (2001).

[4] P. J. karol, Phys. Rev. C **11**, 1203 (1975).

[5] S. K. Charagi and S. K. Gupta, Phys. Rev. C **41**, 1610 (1990).

[6] S. K. Charagi and S. K. Gupta, Phys. Rev. C **46**, 1982 (1992).

[7] S. K. Charagi, Phys. Rev. C **48**, 452 (1993).

[8] S. K. Charagi and S. K. Gupta, Phys. Rev. C **56**, 1171 (1997).

[9] W. Horiuchi, Y. Suzuki, B. Abu-Ibrahim and A. Kohama, Phys. Rev. C **75**, 044607 (2007).

[10] B. Abu-ibrahim, Y. Ogawa, Y. Suzuki and I. Tanihata, Comput. Phys. Commun **151**, 369 (2003).

[11] K. Minomo *et al.*, Phys. Rev. Lett. **108**, 052503 (2012).

[12] S. Kox *et al.*, Phys. Rev. C **35**, 1678 (1987).

[13] A. Ozawa *et al.*, Nucl. Phys. A **693**, 32 (2001).

[14] R. Kanungo *et al.*, Phys. Rev. C **83**, 021302(R) (2011).

[15] R. Kanungo *et al.*, arXiv:1112.3282v1.

[16] M. Takachi *et al.*, Nucl. Phys. A **834**, 412c (2010).

[17] W. Horiuchi, T. Inakura, T. Nakatsukasa and Y. Suzuki, Phys. Rev. C **86**, 024614 (2012).

[18] M. Fukuda *et al.*, Phys. Lett. B **208**, 339 (1991).

[19] T. Kobayashi *et al.*, Phys. Lett. B **232**, 51 (1989).

[20] I. Tanihata *et al.*, Phys. Lett. B **206**, 592 (1988).

Chapter 6

Study of halo nuclear systems

In recent years, a study of the exotic nuclei has gained considerable attention on theoretical and experimental front. With the advancements in the radioactive ion beam facilities, it has become possible to perform numerous experiments to get more information regarding the structural behavior of such nuclei. Neutron and proton halos are one of such exotic phenomenon. The interaction cross sections of nuclei like ^{6,8}He, ^{11}Li and ^{11,14}Be [1–3] have been found to be anomalously larger due to their larger root-mean-square (rms) radii. The investigation of large matter radii and interaction cross sections for ^{19}C, ^{22}N, ^{23}O and ^{24}F suggest the feature of one-neutron halo nuclei [4]. A neutron/proton breakup of halo projectiles with a stable target at near/far barrier energies is one of the tools to investigate the structure of such systems [5]. In addition to this, the measurement of the nuclear reaction cross sections and longitudinal momentum distributions for ^{19,20,22}C [6–8] show that the drip-line nucleus ^{19}C and ^{22}C have a halo structure. It is also relevant to mention that ^{22}C has N = 16 which is a new magic number in the neutron-rich region [9,10] and form a Borromean halo structure (as ^{21}C is unstable). It is of large interest to study the structure and the reaction dynamics of such halo systems through our methodology. In this concern, we have used the Glauber model with two body (core +Neutron) formalism

for the study of the halo nuclei by calculating various reaction cross section observables. The main ingredient for such calculations are densities of the projectile (core) and the target nucleus which are accessed using the microscopic Mean field formalisms.

6.1 Calculations

6.1.1 Bulk properties of halo nuclei

The ground state properties like binding energy B.E., rms matter radius, charge radius, β_2 deformation of some of the halo projectile and core of the projectiles along with the C-target has been studied with the well known RMF formalism using NL3 parameter. These properties are also compared with the non-relativistic Hartree-Fock formalism using a simple effective interaction with SEI-I parameter along with the experimental observations which are available. We have also displayed the results for some of the known unbound nuclei like ^{5}He and ^{10}Li because of their involvement in the present core plus valence Glauber formalism.

Binding energy

The calculated values of B.E. for the core of projectile nuclei are presented in Table 6.1 using RMF(NL3) and non-relativistic HF with the SEI-I parameter. The calculated values of B.E. are in a close agreement with the experimental data [11,12]. The B.E.s, calculated by using RMF(NL3), are slightly higher in magnitude as compared to that for HF(SEI-I). The binding energy difference between the theoretical and the experimental values are also listed in the table. By examining the results of Table 6.1, it can be inferred that both the formalisms are equally capable to reproduce the experimental data.

Table 6.1 The ground state properties of projectile and target nuclei obtained from RMF(NL3) and HF(SEI-I) calculations are compared with experimental data wherever available. The difference between experimental and calculated binding energy $\Delta B.E._{.RMF}$ and $\Delta B.E._{.HF}$ for RMF and HF respectively are given. The binding energy (B.E.) is in MeV, r_{rms} and charge radius r_c are in fm.

	B.E.					r_{rms}		r_c			β_2
Nuclei	RMF	HF(SEI)	Expt. [11, 12]	$\Delta B.E.$ RMF	$\Delta B.E.$ HF(SEI)	RMF	HF(SEI)	RMF	HF(SEI)	Expt. [13]	RMF
^{12}C	89.761	88.422	92.160±1.7	2.399	3.738	2.554	2.413	2.696	2.436	2.47(00)	0.068
^{4}He	34.466	29.003	28.292±0.000	-6.174	-0.711	1.965	1.881	2.128	1.900	1.68(00)	0.011
^{5}He	33.692	31.314	27.560±0.02	-6.132	-3.754	2.618	2.139	2.513	1.917		0.250
^{6}He	34.332	33.144	29.270±0.042	-5.062	-3.874	2.411	2.296	2.100	1.926	2.07(01)	0.689
^{10}Li	52.663	51.107	45.130pm0.01	-7.533	-5.977	2.609	2.661	2.347	2.197		0.028
^{11}Li	54.585	52.737	45.709±0.001	-8.876	-7.028	2.700	2.661	2.356	2.226	2.48(04)	0.019
^{10}Be	65.403	62.561	64.970±0.08	2.409	2.587	2.600	2.379	2.588	2.286	2.36(02)	0.384
^{11}Be	67.954	69.380	65.472±0.000	-2.482	-3.908	2.541	2.510	2.449	2.330	2.46(02)	0.366
^{14}C	107.348	105.829	105.280±0.00	-2.068	-0.549	2.645	2.551	2.647	2.470	2.56(5)	0.025
^{15}C	108.719	108.846	106.500±0.000	-2.219	-2.346	2.627	2.643	2.536	2.480		0.217
^{18}C	116.928	116.707	115.280±0.306	-1.648	-1.427	2.909	2.859	2.616	2.509		0.437
^{19}C	119.655	119.015	116.242±0.098	-3.413	-2.773	2.983	2.920	2.631	2.521		-0.432
^{21}C	121.630	123.096	119.154±0.399	-2.476	-3.942	3.075	3.052	2.586	2.544		0.142
^{22}C	124.157	124.770	120.736±0.506	-3.421	-4.034	3.111	3.133	2.580	2.557		0.016
^{22}O	163.353	164.763	162.008±0.044	-1.345	-2.755	2.924	2.909	2.737	2.678		0.007
^{23}O	167.328	169.040	164.749±0.090	-2.579	-4.291	2.961	2.973	2.726	2.689		-0.015
^{30}Ne	216.040	214.160	211.260±0.270	-4.78	-2.900	3.260	3.236	2.996	2.933		0.004
^{31}Ne	216.145	214.569	211.544±1.619	-4.601	-3.025	3.336	3.289	3.026	2.944		0.236

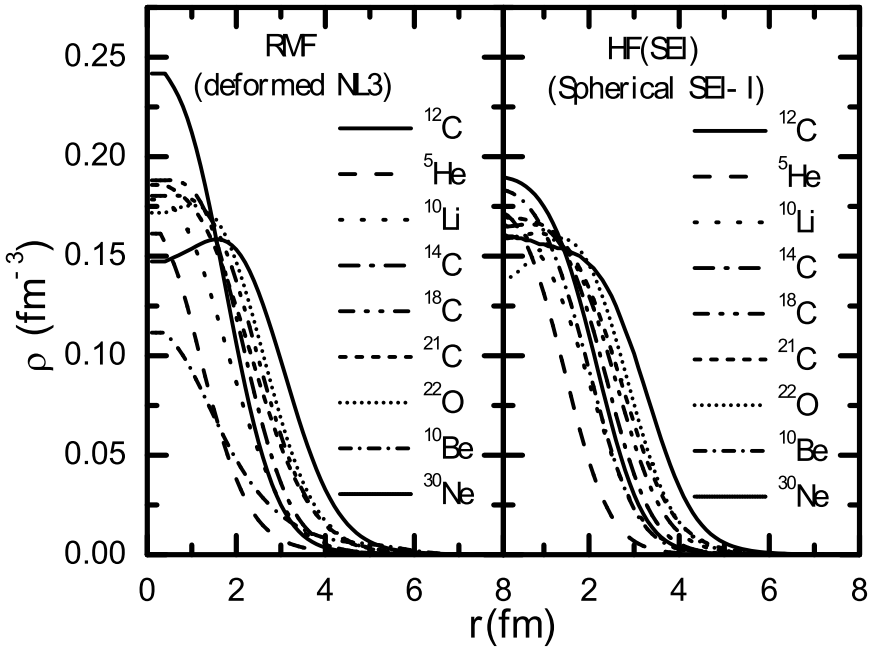

Figure 6.1 The plot of RMF(NL3) and HF(SEI-I) densities as a function of radial distance for various projectile (core) and target nuclei.

Nuclear radii and quadrupole deformation

The calculated root mean square (rms) matter radius (r_m) and charge radius (r_c) of projectile nuclei and core of the projectiles along with target nuclei using relativistic RMF(NL3) and non relativistic HF(SEI-I) mean field theories are presented in Table 6.1. The experimental data is also given for comparison wherever available [13]. The rms proton radius r_p is obtained from the distribution of point protons inside the nucleus. The charge radius r_c is obtained by taking the finite size 0.8 fm correction of the proton which is evaluated from the formula $r_c = \sqrt{r_p^2 + 0.06}$ as reported in [14]. The observation from this table signifies the relevance and an importance of these theories in terms of the successful addressal of various nuclear aspects by predicting the comparable results to the experimental data. Table 6.1 also represents the quadrupole deformation parameter β_2 for halo projectiles and core of the projectile systems obtained from relativistic mean field

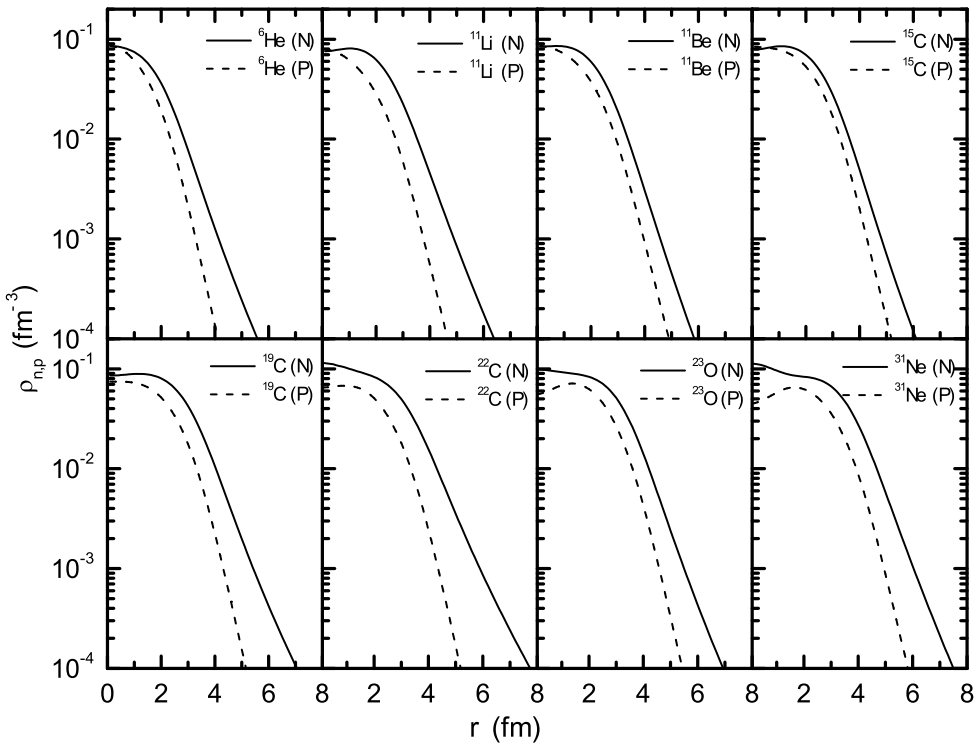

Figure 6.2 The radial densities plot of HF(SEI-I) for projectile nuclei in logarithmic scale.

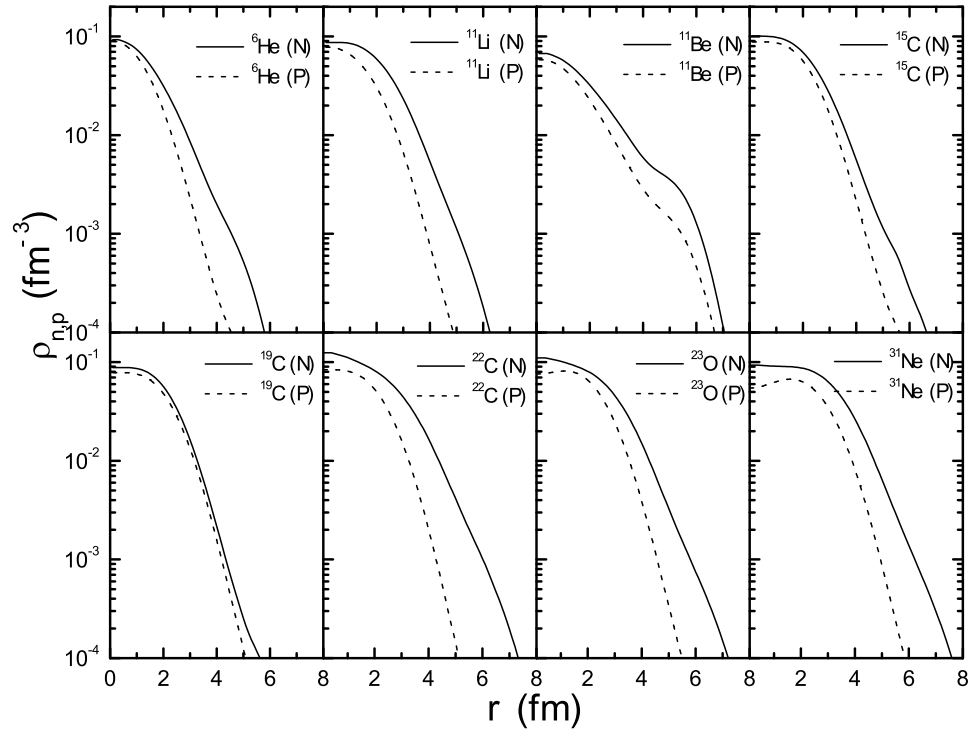

Figure 6.3 Same as figure 6.2, but for RMF(NL3).

Table 6.2 The one (S_n) and two (S_{2n}) neutron separation energies along with single particle (ε_n) energy values of halo nuclei by non relativistic HF(SEI-I) and RMF(NL3) formalisms. The values of S_n, S_{2n} and ε_n are in MeV.

	HF(SEI-I)			RMF(NL3)			Expt. [4]	
Nuclei	S_n	S_{2n}	ε_n	S_n	S_{2n}	ε_n	S_n	S_{2n}
^{6}He	1.830	4.141	4.685	0.64	-0.114	2.465	1.864±0.001	0.974±0.001
^{11}Li	1.630	1.096	3.882	1.922	4.217	3.732	0.330±0.030	0.300±0.030
^{11}Be	4.078	14.453	5.489	2.551	9.697	3.894	0.504±0.006	7.317±0.006
^{15}C	3.017	11.357	2.591	1.371	10.315	2.566	1.218±0.001	9.395±0.018
^{19}C	2.306	4.767	2.259	2.727	5.343	3.263	0.160±0.120	4.350±0.210
^{22}C	3.616	5.755	2.876	2.527	4.438	3.782	1.450±1.030	1.120±0.920
^{23}O	4.282	9.395	4.596	3.975	10.161	4.270	2.740±0.120	9.590±0.100
^{31}Ne	0.409	3.736	0.417	0.105	4.613	1.639		

model with NL3 parameter set. Most of the projectile nuclei in Table 6.1 are prolate in shape except for ^{19}C and ^{23}O (both having oblate deformations). The calculated values of separation energies S_n and S_{2n} for these halo nuclei obtained by both the formalisms HF(SEI-I) and RMF(NL3) are compared with the experimental values in Table 6.2. Relatively smaller magnitude appeared for S_n energy as compare to S_{2n} energy for ^{11}Be, ^{15}C, ^{19}C, ^{23}O and ^{31}Ne nuclei, which are the primary indications of their one neutron halo candidature. Table 6.2 also presents the single particle energy state of the last occupied neutron (ε_n) of the considered halo nuclei using both the formalisms.

Nuclear densities

The densities of ^{12}C, ^{5}He, ^{10}Li, ^{10}Be, ^{14}C, ^{18}C, ^{20}C, ^{22}O and ^{30}Ne nuclei are obtained from axially deformed RMF(NL3) and spherical HF(SEI-I) theories. These axially deformed densities are converted into their spherical equivalent and are presented in Fig. 6.1 along with the spherical non-relativistic HF(SEI-I) densities. Fig. 6.1 (left panel) shows the spherical equivalent of the deformed RMF(NL3) density. The right panel of this figure shows the spherical density obtained from the HF(SEI) formalism with SEI-I

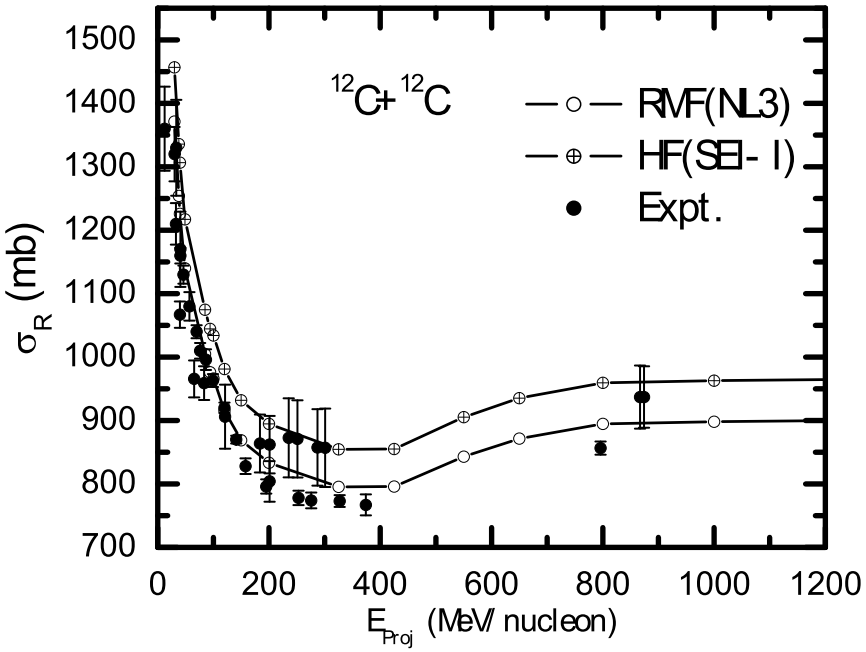

Figure 6.4 The total nuclear reaction cross section (σ_R) as a function of projectile energy. The results obtained from RMF(NL3) and HF(SEI-I) densities are compared with available experimental data [18, 19]

.

interaction parameters [15,16]. We find almost similar densities from both the relativistic mean field (RMF) and the non-relativistic mean field with a simple effective interaction. Some exceptions are also seen in the figure 6.1 for ^{12}C, ^{10}Be and ^{30}Ne nuclei. In case of RMF(NL3) the density of ^{12}C shows a stiff hike in the central portion and a sudden fall in the tail part. On the other hand the behavior of ^{10}Be is found to be opposite. The density distribution of ^{30}Ne shows a small depression at the center indicating the structure of a bubble nucleus. The same effect seems evident to a smaller extent for ^{22}O using both the system of densities, similar to our earlier calculations [17].

Fig. 6.2 and Fig. 6.3 show the protons and neutrons density distributions for the projectiles as a function of the radial distance of considered halo nuclei. A similar trend has been seen for the density distribution of these nuclei using both RMF(NL3) and HF(SEI-I) approaches as depicted in Figures 6.2 and 6.3. The neutron density profile

Table 6.3 The nucleon-nucleon cross section σ_{NN} and other parameters like α_{NN} and β_{NN} used to calculate the profile function.

E(MeV/nucleon)	σ_{NN} (fm^2)	α_{NN}	$\beta_{NN}(fm^2)$
240	3.266868	0.6800303	0.097843707
730	4.174130	-0.082869336	0.1896611
800	4.26000	-0.07000	0.210000
950	4.318554	-0.2078482	0.2142974
960	4.319103	-0.2213738	0.2134798
965	4.319310	-0.2281574	0.2130555

shows the extended distributions in comparison to the proton distributions. This may be because the neutron to proton ratio is greater than one. A longer tail appeared in the neutron density distribution as compared to the proton density distribution which may also relate to its neutron halo nature. The energy and isospin dependant parameters σ_{NN}, α_{NN} and β_{NN} are used for energy range 240-1000 MeV/nucleon and are listed in Table 6.3. A detail description of these parameters is already given in chapter 2^{nd} and 5^{th}. Another important ingredient of the Glauber formalism is the densities of the projectile/core and the target nuclei. The available computational facility can not address the mean field density distributions directly [18]. So, we have converted these mean field densities into 2 Gaussian form and calculated the Gaussian coefficients c_i and a_i. The Gaussian coefficients which are used as input in the Glauber model code are listed in Table 6.4 for both RMF(NL3) and HF(SEI-I) densities.

6.1.2 Total reaction cross sections

Fig. 6.4 represents the variation of the total nuclear reaction cross section for ^{12}C+^{12}C as a function of the projectile energy over the range 30-1200 MeV/nucleon. The σ_R obtained from RMF density upto the range of ($\sim$ 30-120) MeV/nucleon excellently reproduces the experimental data [18, 19]. Beyond this value of projectile energy, σ_R gives enhanced

Table 6.4 The Gaussian coefficients for the projectile (core) and target nuclei with RMF(NL3) and HF(SEI-I) densities.

	RMF(NL3)				HF(SEI-I)			
Nuclei	c_1	a_1	c_2	a_2	c_1	a_1	c_2	a_2
^{12}C	-0.15936	0.632931	0.415315	0.304586	-3.80028	0.361705	3.98436	0.345456
^{5}He	-1.20918	0.363434	1.40551	0.363380	-0.11728	0.689757	0.29453	0.414845
^{10}Li	-1.1064	0.329244	1.28238	0.303979	-1.69225	0.363722	1.86198	0.337186
^{10}Be	-1.23458	0.185387	1.37685	0.185291	-3.36576	0.379683	3.54775	0.363577
^{14}C	-0.433794	0.449739	0.623356	0.291956	-1.88675	0.342428	2.04596	0.308693
^{18}C	-1.21910	0.279772	1.37817	0.243514	-1.94206	0.291905	2.09875	0.263030
^{21}C	-1.18702	0.252476	1.41022	0.225988	-3.99317	0.249448	4.16038	0.238052
^{22}O	-4.06457	0.272853	4.23298	0.257118	-2.56838	0.269287	2.69932	0.244516
^{30}Ne	-3.6109	0.221938	3.74309	0.206388	-2.05083	0.198501	2.19428	0.180662

Table 6.5 Total nuclear reaction cross section for various halo projectiles with ^{12}C target along with experimental data [4, 20–24] for comparison.

	Energy	$\sigma_R(mb)$		
Projectile	(MeV/nucleon)	RMF(NL3)	SEI (SEI-I)	Expt.
^{6}He	800	721	740	722±6
^{11}Li	800	930	944	1060±10
^{11}Be	950	1038	932	942±8
^{15}C	730	995	1054	945±10
^{19}C	960	1187	1202	1231±28
^{23}O	960	1242	1308	1308±16
^{31}Ne	240	1361	1465	1435±22

magnitude. The calculated values of σ_R with HF(SEI-I) are little bit higher than the RMF(NL3) approach. The values of the reaction cross section σ_R obtained by both the densities have reasonable values, which are well comparable to the experimental observations. Some results of our calculations are listed in the Table 6.5 for different projectiles with ^{12}C target. The reaction cross section obtained by using NL3 and SEI-I densities are in good agreement with the experimental data [4, 20–24]. A further inspection of the comparison reveals overall an superiority of SEI-I density over the NL3. It may be noted that the microscopic density obtained from the relativistic mean field theory with NL3 set is quite successful for various applications including the nuclear reaction cross

section calculations [25,26] through out the periodic chart. In our earlier calculations (see chapter 5), it was found that σ_R obtained from RMF(NL3) is superior to the microscopic non-relativistic SHF(SkI4) [27]. However, it is relevant to mention here that the SEI-I density performs even better than NL3 for the estimation of reaction cross section for the chosen set of halo nuclei.

Figure 6.6, shows the total reaction cross section as a function of the projectile energy for ^{6}He, ^{11}Li, ^{11}Be, ^{19}C, ^{22}C and ^{31}Ne halo nuclei over a wide range of energy (30-1000) MeV/nucleon. The value of σ_R is observed to be larger at small incident energy and starts decreasing with the increase of E_{proj} up to $\sim$ 300 MeV/nucleon. A slight increase in σ_R is seen (Fig. 6.6) for $300 - 750$ MeV/nucleon and the σ_R becomes almost independent of E_{proj} beyond 750 MeV/nucelon. The values of σ_R with SEI-I are slightly greater than the NL3 results except from ^{11}Be channel, and an overall comparison with the experimental data is better for SEI-I as compared to NL3.

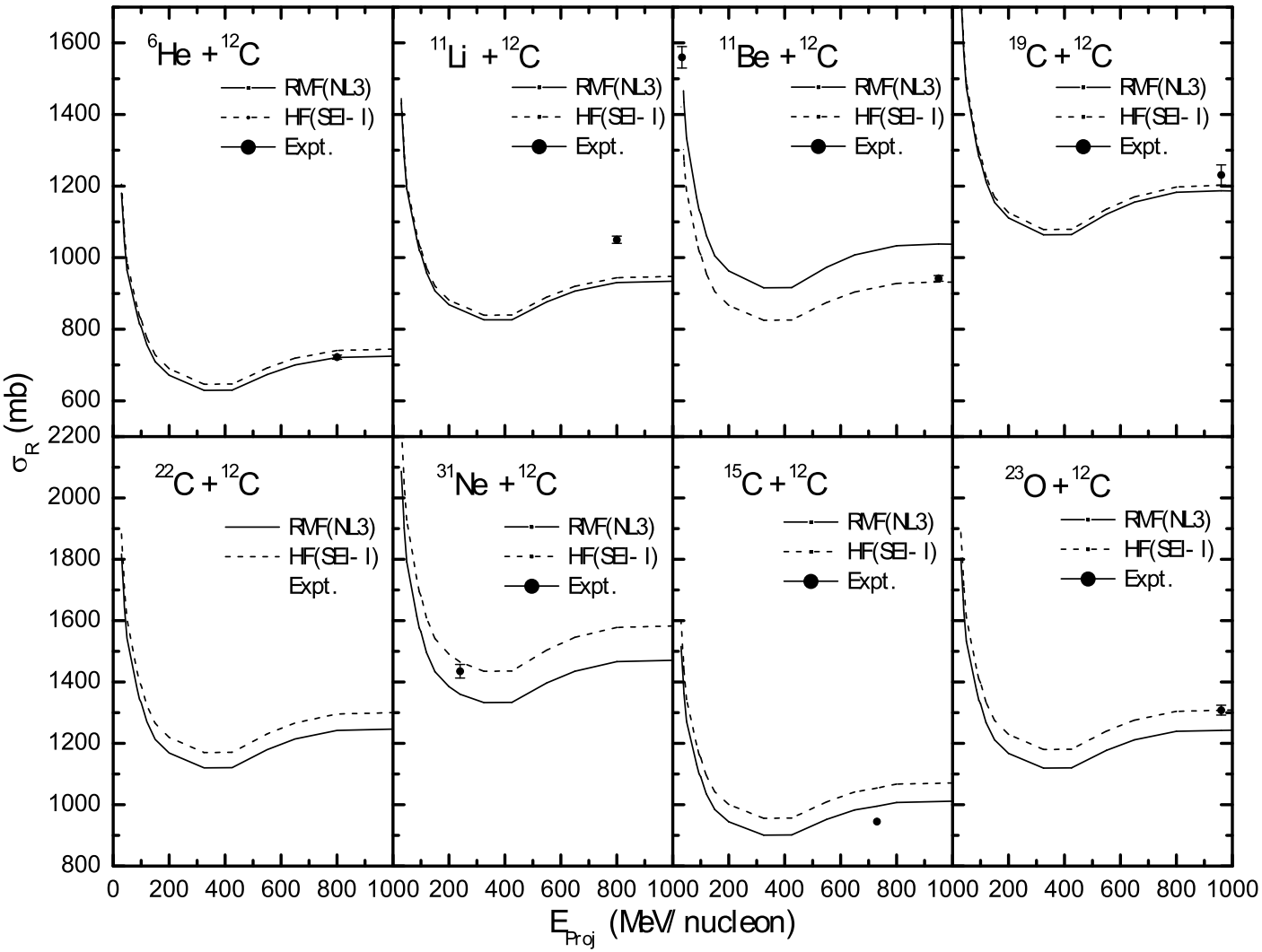

Figure 6.5 Reaction cross section with different projectile energy E_{proj} for ^{6}He, ^{11}Li, ^{11}Be, ^{19}C, ^{22}C and ^{31}Ne projectiles over ^{12}C target. The experimental data are given for comparison wherever available [4, 20–24].

6.2 Investigation of ^{31}Ne halo

The new candidate of ^{31}Ne was included in the family of neutron halo. The measurement of the interaction cross sections for Ne isotopes from the stability line to neutron drip line at 240 MeV/nucleon energy [28–30] shows the dependence of the mass number for $^{27-32}$Ne isotopes, which have been explained by nuclear deformations. The enhancement of the interaction cross sections particularly for ^{29}Ne and ^{31}Ne have been quoted by s-dominant halo structure of ^{29}Ne and s- or p-orbital halo in ^{31}Ne [31]. The recent theoretical investigation of the drip-line nuclei [28–30] predicts a deformed-halo structure of ^{31}Ne. Contrary to these speculations, the three-body model calculations [32] suggest that it is unlikely to find halos in deformed drip-line nuclei because of the correlations between the nucleons, and also due to the static or dynamic deformations of the core suppress the formation of the halo. To settle these deliberate issues, more theoretical and experimental works are needed. In the present study of σ_R, we first use the spherical density obtained from RMF (NL3*) [33]. The results are presented in Figure 6.6 (a) for ^{20}Ne and $^{28-32}$Ne isotopes with ^{12}C- target at 240 MeV/nucleon projectile energy. These results deviate considerably from the experimental data [1, 4, 31, 34, 35], which are quoted in this figure. For example, in case of ^{28}Ne+^{12}C, the observed value of σ_R is 1273 ± 11 MeV as compared to the estimated results of 1440 MeV with NL3* parametrization. In this context, it is interesting enough to see deformation effect on σ_R. We have repeated our calculations of σ_R with the deformed RMF densities as an input in the Glauber model [36, 37]. We have obtained spherical equivalent of the axially deformed densities following the prescription of Refs. [27, 36–39]. The NL3* parameter set [33] for this purpose is used and the results are presented in Figures 6.6 (b) and 6.6 (c). The parameter set NL3* is reasonably a good set for these neutron-rich nuclei. It shows that most of the σ_R match quite well with the experimental data of [24, 31] and still halo case does not agree in Figure 6.6 (b).

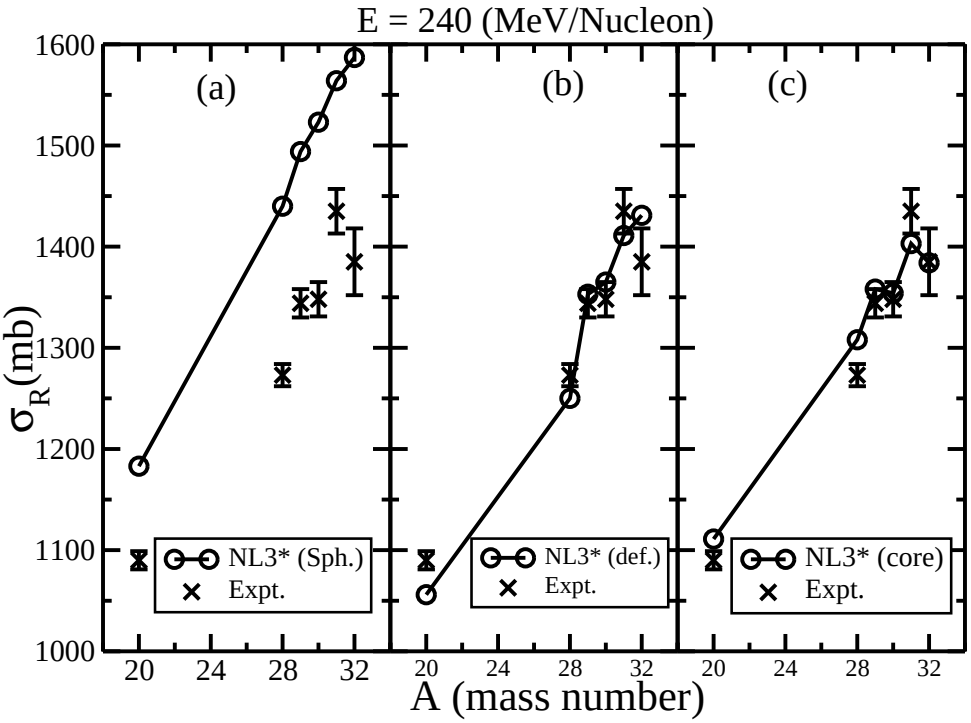

Figure 6.6 Calculated reaction cross sections for scattering of Ne-isotopes on ^{12}C target at 240 MeV/nucleon with experimental data.

In Figure 6.6 (c), we have used Glauber two body formalism (core + one neutron) and found a remarkable agreement with the data. It is observed that our results are little bit higher for relatively lower mass nuclei but there is a better fitting in the neutron rich region. Summarizing the whole discussion on reaction cross sections, in general, one can say that the spherical density used from RMF (NL3*) fails to reproduce the data. On the other side, when we have used the deformed densities to evaluate the total nuclear reaction cross section, the predicted σ_R matches reasonably well with the experimental measurements. Whereas the results are remarkably fit for halo case of ^{31}Ne by using the Glauber two body formalism.

As an extension of these calculations, one neutron removal reaction cross section σ_{-1n} for ^{31}Ne (using core+one neutron) at projectile energy 230 MeV/nucleon with ^{12}C target is 13 mb. (For detailed procedure see Ref. [39].) It has been shown by Panda *et al.* [39] that the calculation done by using this approach fails to reproduce σ_{-1n} for halo cases.

However, the prediction of σ_{-1n} using the difference of two neighboring isotopes with mass number A and A-1 in an isotopic chain reproduce the experimental data which are in good agreement.

$$\sigma_{-1n} = \sigma_R(^{31}Ne) - \sigma_R(^{30}Ne) \tag{6.1}$$

Using Eq. 6.1, we get σ_{-1n} = 82 mb with 2G RMF fitting for ^{31}Ne, which is nicely compared with the experimental value of 79±7 mb [40]. According to [39], the reaction cross section which follows Eq. 6.1 is a halo candidate. Thus, our calculation of σ_R and σ_{-1n} = 82 mb of ^{31}Ne show the presence of a deformed neutron halo in ^{31}Ne in agreement with the prediction of Nakamura *et al.* [40] and other prediction of Ref's. [41, 42].

6.3 Structure of ^{37}Mg halo nuclei

Recently, M. Takechi *et al.* [43, 44], have measured the data of reaction cross section for Mg isotopes at energy 240 MeV/nucleon at RIBF and RIKEN. They have observed large reaction cross section value for ^{37}Mg as compared to other isotopic chain and they consequently predict ^{37}Mg to have a halo structure. In another study S. Watanabe [45] concludes from his fully microscopic double folding frame work with the AMD densities as deformed halo structure of ^{37}Mg. One more study by Subhchintak *et al.* [46], on coulomb breakup of ^{37}Mg+Pb reaction at beam energy 244 MeV/nucleon with in the framework of a finite range distorted wave approximation theory, supports one neutron halo configuration of ground state ^{37}Mg isotope with a parallel momentum distribution of the core fragment and strong forward peaking of the valence neutron angular distribution. The measurements of the separation energy, 1n-removal reaction cross section and momentum distribution of ^{37}Mg by N. Kobayashi *et al.*, [47] also suggest it as p-wave neutron halo nucleus. They also confirm that ^{37}Mg lies in the island of inversion and has the heaviest

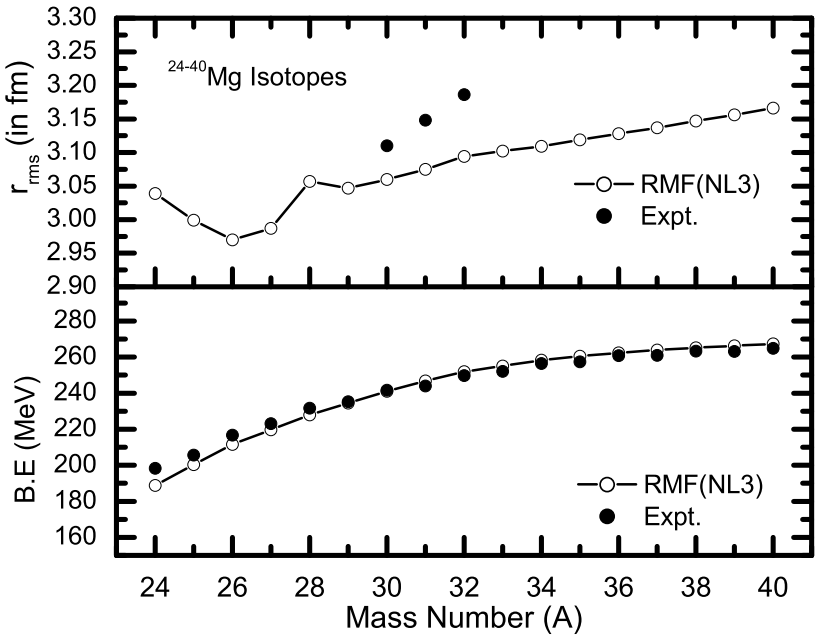

Figure 6.7 The values of binding energy (B.E.) in MeV and charge radius (r_c) of Mg-isotopes obtained from RMF(NL3) as a function of mass number 'A'. The experimental data are also given for comparison whichever be available.

deformed halo candidate. In our earlier work we explored the structure of some isotopes of Ne, Mg and Si [48]. Whereas the identification of this new halo candidate creates our interest to review our study for Mg-isotopes. Since these are the terms which motivate us to study the reaction dynamics of Mg isotopes at energy 240 MeV/nucleon, we have also tried to study the structural features of ^{37}Mg by our studies. First of all, the ground state properties of Mg-isotopes are calculated using microscopic relativistic mean field formalism. Fig. 6.7 shows the calculated values of binding energy (B.E.) and charge radius (r_c) of considered set of Mg-isotopes. The lower panel of the figure shows the calculated values of B.E. along with the experimental data which looks nice agreement with each other. A deep inspection of the figure suggests that the B.E.'s are slightly underestimate up to the ^{29}Mg and overestimate beyond ^{32}Mg isotopes as compared to data values. While the upper panel of the figure compares the calculated value of rms charge radius (r_c) of a

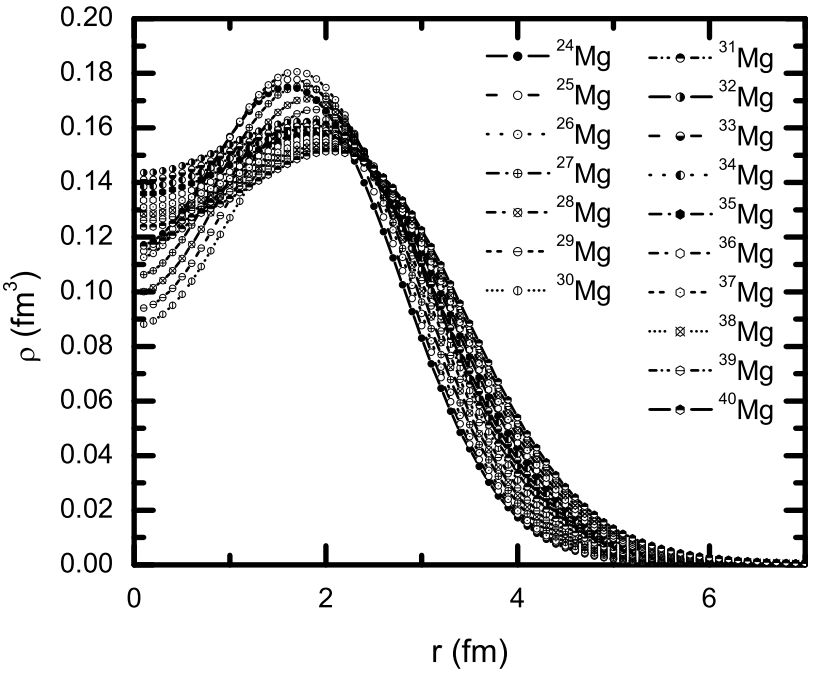

Figure 6.8 The density profile of Mg-isotopes from RMF(NL3) formalism as a function of radial distance.

considered set of isotopes with the experimental data. The calculated values of r_c are underestimates in comparison to the experimental data. Fig. 6.8 shows the trend of relativistic mean filed (RMF) densities of projectiles with NL3 parameter set, which shows the density profile as a function of the radial distance for $^{24-40}$Mg isotopes. Here the nucleonic density distribution is of larger magnitude at the center and goes on decreasing with an increase in radius, also the small depletion in densities appear at the center for these nuclei. One may also observe from the figure that the skin effect increases with an increase in isotopic mass number, similar to as discussed in chapter 3. The densities converted into Gaussian form and calculated values in terms of Gaussian coefficients c_i's and a_i's are listed in Table 6.6 for NL3 interaction. In order to check the sensitivity of our calculations, we have compared the RMF densities with the spherical equivalent densities from Gaussian coefficients in Figure 6.9. This figure clearly shows the similarity between

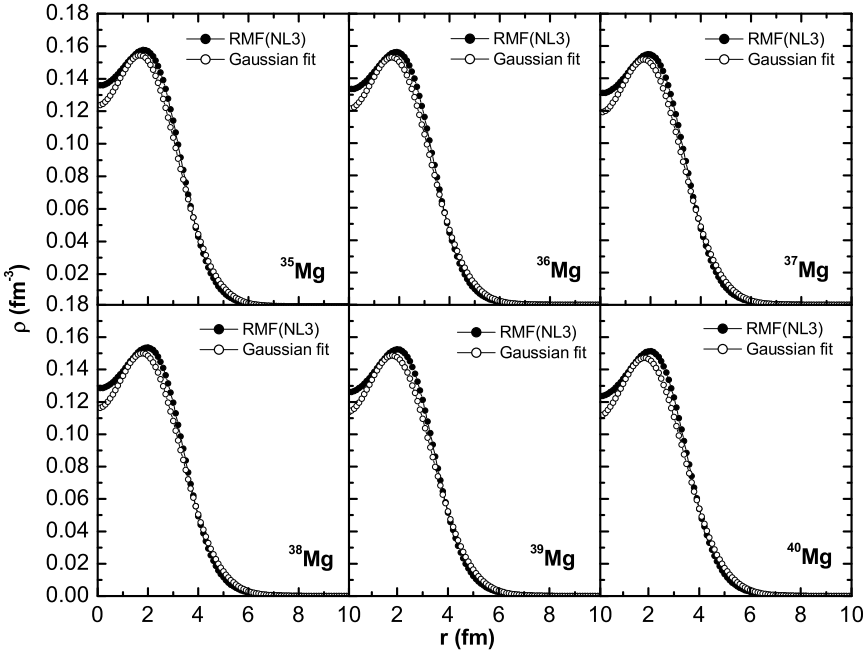

Figure 6.9 The comparison of RMF densities with spherical equivalent densities obtained from Gaussian coefficients for $^{35-40}$Mg isotopes as a function of radial distance.

Table 6.6 The Gaussian coefficients for the projectile and target nuclei after fitting RMF(NL3) densities.

	RMF(NL3)			
Nuclei	c_1	a_1	c_2	a_2
^{12}C	-0.232654	0.638687	0.517232	0.339911
^{24}Mg	-3.6936	0.286163	3.80452	0.261585
^{25}Mg	-3.89231	0.281947	4.00019	0.258213
^{26}Mg	-4.07533	0.277958	4.18027	0.25493
^{27}Mg	-4.065	0.266396	4.1637	0.244635
^{28}Mg	-3.93233	0.256062	4.02441	0.234787
^{29}Mg	-3.89795	0.246598	3.98355	0.226164
^{30}Mg	-3.87287	0.237936	3.95204	0.218274
^{31}Mg	-3.41668	0.224842	3.52235	0.206223
^{32}Mg	-2.96194	0.211646	3.09244	0.194095
^{33}Mg	-2.96276	0.206741	3.09102	0.189597
^{34}Mg	-2.96402	0.202127	3.08998	0.185357
^{35}Mg	-2.96363	0.197607	3.08718	0.18121
^{36}Mg	-2.96752	0.193359	3.08865	0.177322
^{37}Mg	-2.96752	0.189208	3.08637	0.173515
^{38}Mg	-2.97189	0.185226	3.08797	0.169881
^{39}Mg	-2.97547	0.181501	3.08903	0.166466
^{40}Mg	-2.98107	0.17785	3.09205	0.163137

both the density distributions. The densities obtained from the Gaussian coefficients have fair fitting at tail part, which plays a major role in the scattering phenomenon. Further for extension of the reaction dynamics, the single particle wave function is used in the Glauber many body system (Core+nucleon). The radial part of a single particle wave function has been obtained after solving Schrodinger equation using Wood-Saxon type potential between two body (core+nucleon) as in the form:

$$U(r) = -v_0 f(r) + V_{ls}(l.s) r_0^2 \frac{1}{r} \frac{df(r)}{dr} + V_{Coul}, \tag{6.2}$$

where $f(r) = [1 + \exp(\frac{r-R}{a})]^{-1}$ and $R = r_0 A^{(1/3)}$. The first term of equation 6.2 contains the central potential, second term contains the spin orbital part and the last term of the equation contains the Coulomb part of the potential. Here, we vary the diffuseness parameter 'a' to study the role of an extended density on the reaction cross sections for ^{37}Mg isotope. Because by increasing the value of 'a' the density distribution extended exponentially in the tail region of the nucleus, which may give rise to loosely bound structure. Fig. 6.10 represents the values of σ_R for $^{24-40}$Mg+^{12}C reactions at E_{Proj}=240 MeV/nucleon as a function of mass number (A) of the projectile nucleus. The calculated values of σ_R in the figure show a decent agreement with the experimental data except for the cases of ^{30}Mg and ^{37}Mg in the region of island of inversion, which supports the success of RMF densities in the context of the present study. The estimated value of σ_R of ^{24}Mg projectile slightly underestimates the experimental measurement. This may be due to near by the region of minimum proton-neutron correlation. On the other side the abrupt changes in σ_R for ^{27}Mg and ^{28}Mg or ^{30}Mg and ^{31}Mg are correlated with the spherical and the deformed structure by M. Takechi *et al.*, [43,44]. Further in their observations, change in σ_R between ^{36}Mg and ^{37}Mg is suggested either because of highly deformed structure or halo

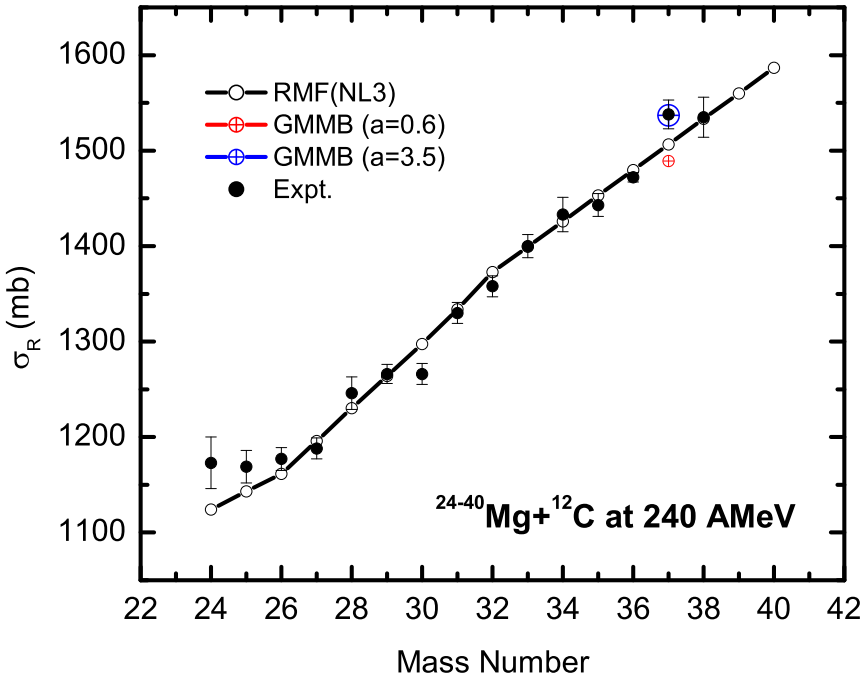

Figure 6.10 Reaction cross section for $^{24-40}$Mg as projectile with ^{12}C target nucleus at E_{proj}= 240 MeV/nucleon. The experimental data are also given for comparison [43, 44].

nature of ^{37}Mg isotopes. Since the isotopes of the nuclear system from $^{30-38}$Mg lies near or in the island of inversion [49, 50] and may require a special attention. A difference in the theoretical and the experimental data for ^{30}Mg and ^{37}Mg nuclei is significant, which seems to suggest that they exhibit unusual structure and hence need further investigation. But, in this problem, our interest is to investigate the possibility of halo behavior of ^{37}Mg isotope. For further study on ^{37}Mg projectile, we have used Glauber Model with Many body (core+nucleon) system. The details of the calculations can be seen in [18,51]. Fig. 6.11 represents the calculated values of σ_R (in mb) and r_{rms} (in fm) for the ^{37}Mg projectile. The upper panel of this figure shows the root mean square radius r_{rms} and the lower panel σ_R for ^{37}Mg as a projectile over ^{12}C target at energy 240 MeV/nucleon as a function of diffuseness parameter 'a' in fm. We have tried to fit the reaction cross section

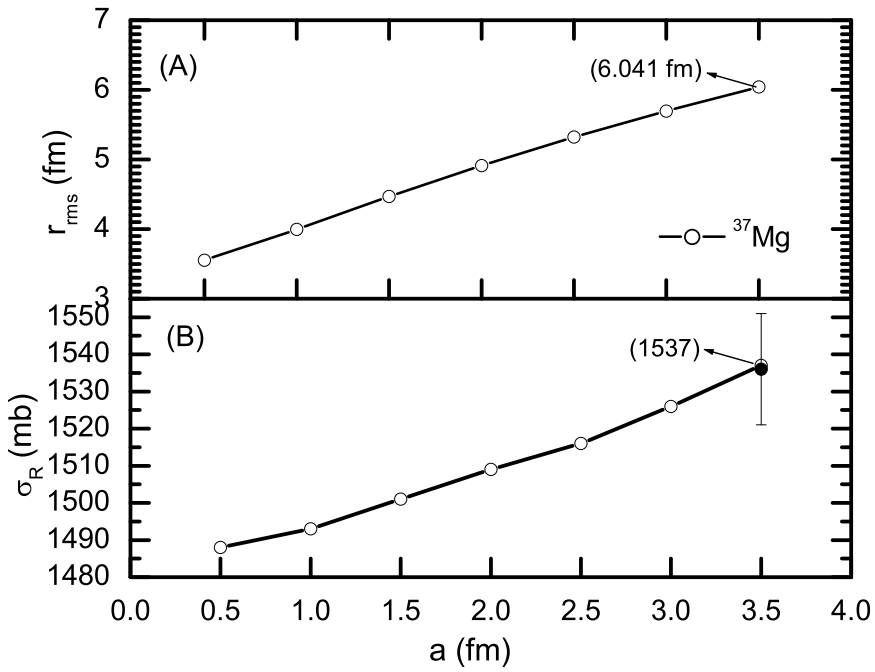

Figure 6.11 (A) Upper panel of the figure shows the rms radius (r_{rms}) in fm and (B) lower panel shows the values of reaction cross section σ_R in mb as a function diffuseness parameter 'a' in fm for ^{37}Mg.

for ^{37}Mg projectile at different values of diffuseness parameter. It is clear from the figure that the reaction cross section and diffuseness parameter are linearly dependant on each other. The value of σ_R obtained at diffuseness parameter = 3.5 fm is 1537 mb, which is well comparable to the experimental observation 1536±15 mb. Hence the lower panel of the figure shows that the value of reaction cross section fit with the experimental value at a = 3.5 fm. The upper panel of the figure shows the rms radius values of core+neutron system as a function of diffuseness parameter. We observed that the value of root mean square radius of the projectile (core + nucleon) at a = 3.5 fm is 6.041 fm. Thus the large value of the reaction cross section has a direct consequence to its large radius and halo nature of ^{37}Mg isotope. For comparison, we have plotted the results of σ_R for same value of the diffuseness parameter (a = 0.6 fm) by using Glauber Model (GM) with RMF(NL3) density and Glauber Model Many body system (core+nucelon) (GMMB) in Fig. 6.10. It

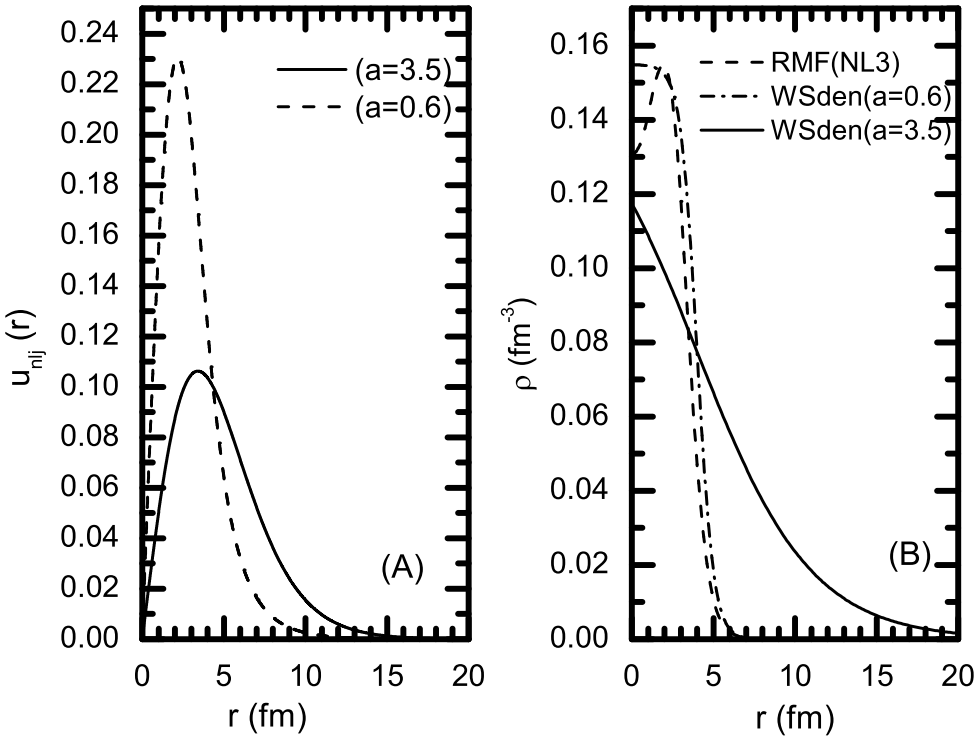

Figure 6.12 (A) Comparison of single particle wave function for different values of diffuseness parameter 'a' and (B) Comparison of the wood saxon densities with different diffusion parameter and RMF(NL3) density of ^{37}Mg as function of radial distance in fm.

is clear from the figure that σ_R underestimate the experimental data for both the formalism. Hence the fitted data with GMMB formalism at a=3.5 fm are also given in figures 6.10 and 6.11. The comparisons of wave function for different value of diffuseness parameters and RMF density for ^{37}Mg with Wood-Saxon density having diffuseness parameter 0.6 fm and 3.5 fm are shown in Fig. 6.12. Figure 6.12 (A) shows variation of single particle wave function with radial distance for different values of diffuseness parameter. This figure suggests that the wave function is more steeper at diffuseness value of 0.6 fm where it becomes broader at 3.5 fm. In order to investigate the effect of diffuseness parameter on the density profile, we have plotted the Wood-Saxon density on right side of this figure along with the RMF density of ^{37}Mg. Figure 6.12 (B) shows that the behavior

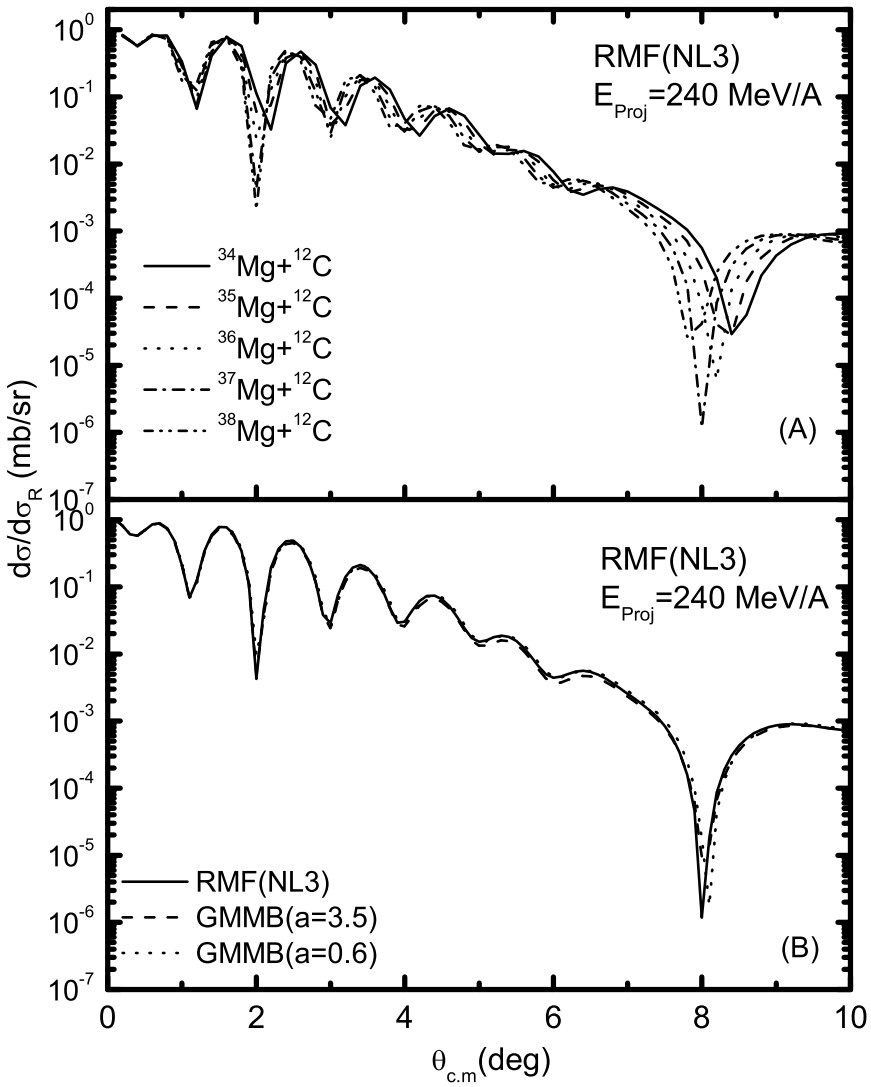

Figure 6.13 (A) The values of angular elastic differential cross section for $^{34-38}$Mg+^{12}C reactions at E_{proj}= 240 MeV/nucleon (B) The comparison of angular elastic differential cross section using RMF densities with GM and GMMB systems.

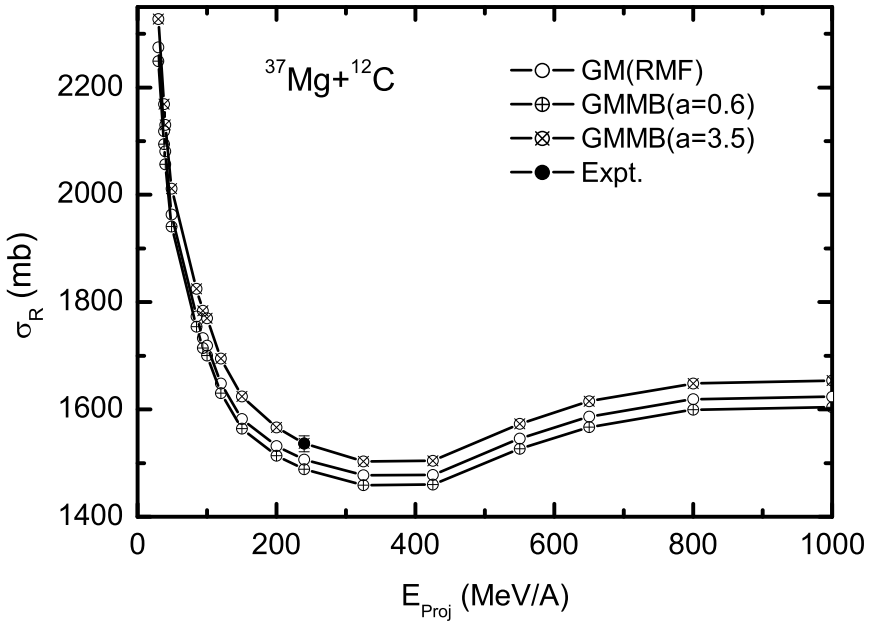

Figure 6.14 Variation of total reaction cross sections for ^{37}Mg projectiles as a function of E_{Proj}.

of Wood-Saxon density is similar to RMF at a=0.6 fm. At the value of 'a = 3.5 fm', we get a long extension of density even beyond $\sim$ 15 fm, further suggesting the possibility of a halo structure of ^{37}Mg nucleus. This behavior of an extension in the tail part is not possible to see in the relativistic mean field formalism. Because in RMF formalism the densities are automatically generated with a self consistency. Although this large value of a = 3.5 fm looks unusual, but still be relevant for exotic nuclei exhibiting halo structure. For further significance of higher diffuseness parameter 'a', one needs to have an extensive investigation by addressing reaction dynamics involving various halo nuclei. We have fitted density with a Wood-Saxon form taking variation in diffuseness parameter 'a'. The elastic differential cross sections as a function of an angular distribution for $^{34-38}$Mg projectiles on the carbon target at E_{Proj}=240 MeV/nucleon are shown in Fig. 6.13 (A). The inspection of the figure suggests that two dip positions are observed at an angles $\theta_{c.m} = 2^0$ and 8^0. One may also observe that the dip position varies with the isotopic

mass number from $8^0 - 8.5^0$ angle. It is also relevant to say that the dip position goes on decreasing with an increase in isotopic mass number. Fig. 6.13 (B) shows the comparison between the angular elastic differential cross section for ^{37}Mg+^{12}C reaction at E_{Proj}=240 MeV/nucleon using GM(RMF) and GMMB for a = 0.6 fm and a = 3.5 fm. It is clear from the figure, that all the distributions have similar dip positions, however the depth of the dip is slightly smaller for GMMB (a=0.6), where as depths are of same size for rest cases at an angle 2^0. Similarly, the dip position are almost similar with comparable size at 8^0 for both GM(RMF) and GMMB (a=3.5). But the dip position appears slightly at higher angle for GMMB (a=0.6). Both Fig's. 13 (A) and 13 (B) shows a clear oscillatory pattern in which magnitude of the oscillations are large at smaller angles and keeps on decreasing with an increase in angles at E_{Proj}=240 MeV/nucleon.

The variation of the reaction cross section for ^{37}Mg+^{12}C reaction by GM(RMF), GMMB(a=0.6) and GMMB(a=3.5) as a function of the projectile energy for 30-1000 MeV/nucleon are plotted in figure 6.14 along with the experimental data whichever available. It is clear from figure that the results obtained with GM(RMF) and GMMB(a=0.6) are slightly underestimate the experimental data. Fig. 6.15 shows the one neutron removal cross section for ^{37}Mg+^{12}C reaction as a function of E_{Proj} along with the experimental data. The upper panel of the figure shows that total one nucleon removal cross section (σ_{-N}^{Total}) obtained from GM(RMF), GMMB (a=0.6) and GMMB (a=3.5) formalisms. The value of σ_{-N} estimated in GM(RMF) by relation

$$\sigma_{-N} = \sigma_R(^{37}Mg) - \sigma_R(^{36}Mg), \tag{6.3}$$

for the projectile energy range (30 - 1000) MeV/nucleon. The estimated values of σ_{-N} by GM(RMF), GMMB (a=0.6), GMMB (a=3.5) are 27mb, 9 mb and 57 mb compared with

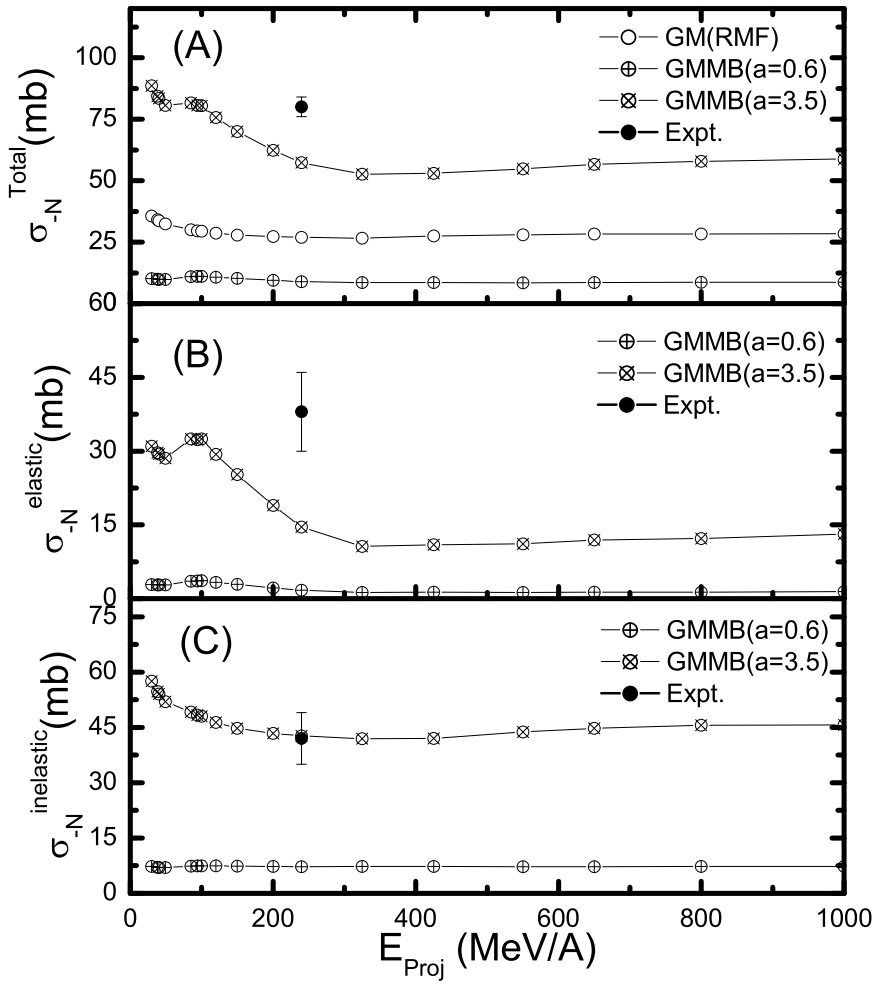

Figure 6.15 One neutron removal cross section for ^{37}Mg+^{12}C reaction including (A) total (B) elastic and (C) inelastic part as a function of E_{Proj} in MeV/nucleon. The experimental values are also given for comparison wherever be available [47].

the experimental results of Kobayashi *et al.*, [47] 80±4 mb for energy 240 MeV/nucleon. Whereas the lower and the middle panels of Fig. 9 show the estimated inelastic and elastic components with GMMB for a = 0.6 and a = 3.5 fm. Further the components of the elastic and inelastic contributions 2 mb, 7 mb with (a=0.6) and 14 mb, 43 mb with (a=3.5) are also compared with data 38±8 and 42±7 mb respectively. The calculated values of inelastic component matches nicely with the experimental value for (a=3.5), whereas the elastic component under estimate the data. From these calculations, the larger skin, support our earlier work of total reaction cross section. It is clear from the results and Fig. 6.15 that the inelastic component in neutron removal cross section dominates over their elastic component at E_{Proj}=240 MeV/nucleon. The trend of the reaction cross section in Fig. 6.14 and one neutron removal cross section in Fig. 6.15 are similar, but smaller hike is seen in one neutron removal cross section at E_{Proj}=100 MeV/nucleon, because of its elastic component.

The estimated longitudinal momentum distribution of ^{36}Mg core for the reaction ^{37}Mg+^{12}C at E_{Proj}=240 MeV/nucleon is represented in figure 6.16. The momentum distributions are estimated by both Glauber model and GMMB formalism at a = 0.6 fm. These distributions in both the formalisms are almost similar. The calculated values of momentum distributions are scaled to central experimental data points for comparing its distribution with the recent experimental observation. This figure also signifies that momentum distributions match remarkably with the experimental data for both formalisms. The momentum distribution is also measured with the Glauber model two body formalism for a = 3.5 fm. The width of this distribution appeared slightly narrower in comparison with our earlier measurements for GM(RMF) and GMMB (a=0.6) or experimental data due to thicker neutron skin.

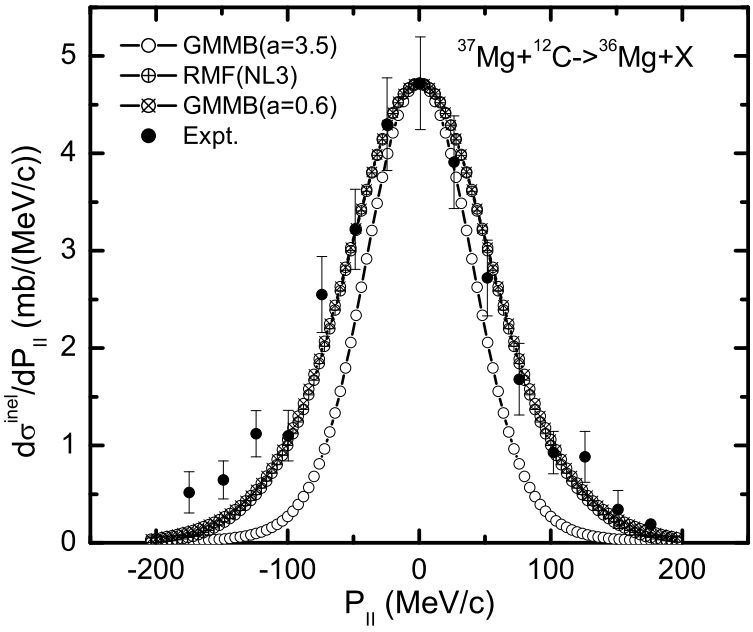

Figure 6.16 Longitudinal momentum distribution of ^{36}Mg from the ^{37}Mg+^{12}C at projectile energy 240 MeV/nucleon. The experimental data are also given for comparison [47].

6.4 Summary

We have calculated ground state properties and reaction cross section for some of the halo nuclei ^{6}He, ^{11}Li, ^{11}Be, ^{15}C, ^{19}C, ^{22}C, ^{23}O and ^{31}Ne as projectiles with ^{12}C target using relativistic and non-relativistic mean field formalisms. The estimated values of binding energy, rms radius, rms charge radius, quadrupole deformation and one/two neutron separation energies from both the formalisms have been compared with the available experimental data. Both the approaches have justified their results in comparison with the data similar to our earlier works. Hence densities obtained from completely different sources have been used in the extended Glauber model (GMMB) for evaluation of σ_R over the broad energy range. In conclusion, results obtained from both the RMF and Hartree-Fock formalisms are well compared with the experimental data with an edge of the SEI-I interaction.

In another work an effort has been made to analyze the structure of ^{31}Ne. In this regards

a systematic study of reaction cross sections has been done for $^{28-32}$Ne as projectile using densities from sph. RMF, def. RMF and GMMB (core+neutron) systems. We interpret from our results that the calculated values of the reaction cross sections overestimated with sph. RMF densities, where as remarkable fit with the def. RMF densities except for ^{31}Ne and ^{32}Ne cases. The errors are also rectified with the consideration of GMMB formalism. From an analysis of the reaction cross section and one neutron removal cross section also supports the halo status of ^{31}Ne isotopes.

Further we have extended above discussed formalism for the investigation of newly identified halo nuclei of ^{37}Mg. We have calculated the ground state properties of Mg isotopes with RMF formalism and also studied the reaction cross sections of these isotopes taken as projectile from the valley of stability to drip line region with stable ^{12}C target at E_{proj} 240 MeV/nucleon. We found a nice agreement of the ground state properties of Mg-isotopes with available data. The calculated values of the reaction cross section using RMF densities find a nice agreement with the experimental data. The excellent agreement of the estimated reaction cross section values except for a few isotope is an evidence of the predictive power of RMF densities. The skin effect variation with the mass number is studied in the context of density profile. The study of an angular elastic differential cross section for $^{34-38}$Mg projectile on C-target shows a clear oscillatory pattern. Further investigation with Glauber two body calculation also supports the halo status of ^{37}Mg. Subsequently we examined the halo status of ^{37}Mg and it seems justified from its higher magnitude of rms radius $\sim$6.041 fm, one neutron removal cross section and small longitudinal momentum distribution.

Bibliography

[1] I. Tanihata, H. Hamagaki, O. Hashimoto, Y. Shida, N. Yoshikawa, K. Sugimoto, O. Yamakawa, T. Kobayashi and N. Takahashi, Phys. Rev. Lett. **55**, 2676 (1985).

[2] I. Tanihata *et al.*, J. Phys. G **22**, 661 (1996).

[3] I. Tanihata *et al.*, Phys. Lett. B **287**, 307 (1992).

[4] A. Ozawa *et al.*, Nucl. Phys. A **691**, 599 (2001).

[5] B. Paes, J. Lubian, P. R. S. Gomes and V. Guimaraes, Nucl. Phys. A **890-891**, 1-10 (2012).

[6] D. Bazin, B. A. Brown *et al.*, Phys. Rev. Lett. **74**, 18 (1995).

[7] K. Tanaka *et al.*, Phys. Rev. Lett. **104**, 062701 (2010).

[8] N. Kobayshi *et al.*, arXiv: 1111.7196 v1 [Nucl. ex] (2011).

[9] A. Ozawa *et al.*, Phys. Rev. Lett. **84**, 24 (2000).

[10] I. Tanihata *et al.*, Nucl. Phys. A **682**, 114c (2001).

[11] G. Audi, A. H. Wapstra and C. Thibault, Nucl. Phys. A **729**, 337 (2003).

[12] http://amdc.in2p3.fr/masstable/Ame 2011int/mass....

[13] C. W. De Jager, H. De Vries and C. De Vries, At. Data and Nucl. Data Table **14**, 479 (1974).

[14] S. K. Patra and C. R. Praharaj, Phys. Rev C **44**, 2552 (1991).

[15] T. R. Routray, X. Vinas, S. K. Tripathy, M. Bhuyan, S. K. Patra, B. Behera, J. Phys. Conf. Ser. **420**, 012114 (2013).

[16] B. Behera, X. Vinas, M. Bhuyan, T. R. Routray, B. K. Sharma and S. K. Patra, J. Phys. G: Nucl. Part. Phys. **40**, 095105 (2013).

[17] A. Shukla, Sven Åberg and S. K. Patra, J. Phys. G **38**, 095103 (2011).

[18] B. Abu-ibrahim, Y. Ogawa, Y. Suzuki and I. Tanihata, Comput. Phys. Commun. **151**, 369 (2003).

[19] W. Horiuchi, Y. Suzuki, B. Abu Ibrahim and A. Kohama, Phys. Rev. C **75**, 044607 (2007).

[20] B. Abu-Ibrahim and Y. Suzuki, Phys. Rev C **61**, 051601 (2000).

[21] M. Fukuda *et al.*, Phys. Lett. B **208**, 339 (1991).

[22] T. Kobayashi *et al.*, Phys. Lett. B **232**, 51 (1989).

[23] I. Tanihata *et al.*, Phys. Lett. B **206**, 592 (1988).

[24] M. Takachi *et al.*, Nucl. Phys. A **834**, 412c (2010).

[25] A. Shukla, B. K. Sharma, R. Chandra, P. Arumugam and S. K. Patra, Phys. Rev. C **76**, 034601 (2007).

[26] S. K. Patra, R. N. Panda, P. Arumugam and R. K. Gupta, Phys. Rev. C **80**, 064602 (2009).

[27] M. K. Sharma, M. S. Mehta and S. K. Patra, Int. J. Mod. Phys. E **22**, 1350005 (2013).

[28] I. Hamamoto, Phys. Rev. C **81**, 021304(R) (2010).

[29] Y. Urata, K. Hagino and H. Sagawa, Phys. Rev. C **83**, 04130 (2011).

[30] K. Minomo, T. Sumi, M. Kimura, K. Ogata, Y. R. Shimizu and M. Yahiro, Phys. Rev. C **84**, 034602 (2011).

[31] M. Takechi *et al.*, Phys. Lett. B **707**, 357-361 (2012).

[32] F. M. Nunes, Nucl. Phys. A **757**, 349 (2005).

[33] G. A. Lalazissis, S. Karazikos, R. Fossion, D. Pena Arteage, A. V. Afanasjev and P. Ring, Phys. Lett. B **671**, 36 (2009).

[34] T. Sujuki *et al.*, Phys. Rev. Lett. **75**, 3241 (1995).

[35] M. Takechi *et al.*, Mod. Phys. Lett. A **25**, 1878 (2010).

[36] A. Shukla, B. K. Sharma, R. Chandra, P. Arumugam and S. K. Patra, Phys. Rev. C **76**, 034601 (2007).

[37] B. K. Sharma, S. K. Patra, Raj K. Gupta, A. Shukla, P. Arumugam, P. D. Stevenson and Greiner Walter, J. Phys. G **32**, 2089 (2006).

[38] S. K. Patra, R. N. Panda, P. Arumugam and Raj K. Gupta, Phys. Rev. C **80**, 064602 (2009).

[39] R. N. Panda and S. K. Patra, Int. J. Mod. Phys. E **20**, 2505 (2011).

[40] T. Nakamura *et al.*, Phys. Rev. Lett. **103**, 032501 (2009).

[41] W. Horiochi, Y. Suzuki, P. Capel and D. Baye, Phys. Rev. C **81**, 024606 (2010).

[42] K. Minomo *et al.*, Phys. Rev. Lett. **108**, 052503 (2012).

[43] M. Takechi *et al.*, EPJ Web of conference **66**, 02101 (2014).

[44] M. Takechi *et al.*, Phys. Rev. C **90**, 061305 (2014).

[45] S. Watanabe *et al.*, EPJ Web of conference **66**, 03095 (2014).

[46] Shubhchintak, Neelam, R. Chatterjee, R. Shyam and K. Tsushima, Nucl. Phys. A **939**, 101-120 (2015).

[47] N. Kobayashi *et al.*, Phys. Rev. Lett. **112**, 242501 (2014).

[48] R. N. Panda, Mahesh K. Sharma and S. K. patra, Mod. Phys. Lett. A **29**, 1450013 (2014).

[49] S. K. Patra and C. R. Praharaj, Phys. Lett. B **273**, 13 (1991).

[50] A. N. Deacon *et al.*, Phys. Rev. C **82**, 034305 (2010).

[51] Mahesh K. Sharma and S. K. Patra, Phys. Rev. C **87**, 044606 (2013).

Chapter 7

Summary of thesis

In the present thesis, we have studied the structural behavior and the reaction dynamics of numerous nuclei from beta stability line to drip line region. In this context, the structure effects of the light mass nuclei have been investigated using the well known microscopic mean field theories. The advantage of these mean field formalisms is to deduce the bulk properties of nuclei in a self consistent manner. The bulk properties like binding energy, root mean square matter and charge radius, quadrupole deformation, nucleon separation energy, single particle energy, nucleonic density distribution of light mass to medium mass nuclei *etc.* are studied with both relativistic and non-relativistic mean field formalisms. The reaction dynamics of such nuclear systems have been studied with the help of the Glauber formalism. The success of this formalism is based on the densities of the projectile and the target nuclei. Hence, we have used the densities of the mean field formalism to optimize the various reaction parameters. The study gets limited due to the non-availability of scattering data from heavy to super heavy mass nuclei at the intermediate energy.

chapter 1 consists of general introduction and a brief discussion of the background of the present work. In this chapter, a nuclear landscape is discussed with general reference to

beta-stable, neutron/proton rich and drip-line region *etc.* The Exotic behavior of neutron rich nuclei is discussed and the vanishing of the shell closure effect near at deformed nuclei, one/two neutron halo, bubble effect in densities *etc.* are also discussed in this chapter. A brief discussion of the nuclear structure models, nuclear scattering and nuclear reactions are also outlined and a brief description of the background of Glauber, relativistic mean field and non-relativistic mean field formalisms is given in this chapter.

Chapter 2 outlines both the non-relativistic and the relativistic mean field models in detail. The Skyrme Hartree-Fock (SHF) model within Hamiltonian density functional mechanism is discussed, whereas Lagrangian density functional is described for the relativistic mean field model. The field equations for nucleons and bosons are also described within the RMF approach. The calculation details leading to the solutions of the RMF equations have been given in this chapter. The BCS-pairing prescription and other pairing correlations are also presented in this chapter. The parameter sets used in the calculations for relativistic and non-relativistic mean field formalisms are analyzed. A detail of the Glauber approach is also discussed in the subsection of this chapter for both the stable and the unstable nuclei. The transparency function and the profile functions required for the cross section calculations are also elaborated in this chapter.

In **chapter 3**, we have discussed the ground state properties like binding energy (B.E.), rms charge radius (r_c), quadrupole deformation (β_2), nucleonic density distributions *etc.* of isotopes of Be-Ar nuclei using both relativistic and non-relativistic mean field formalisms. A choice of parameters used like NL3/NL3* in RMF and SkI4, SEI in HF approach for the evaluation of the bulk properties are also discussed at the beginning of this chapter. A choice of the bosonic and the fermionic model space is very much important for the estimation of bulk properties of exotic nuclei. The scrutinizing of the optimal limit has been tested through the variation of $N_F = N_B$ for the test cases of ^{36}Si

isotope. The rest calculations of selected mass regions are taken care by this choice of fermionic and bosonic model space. The predicted results are also compared with the experimental data. The comparison between the estimated and the data values suggests that both the formalisms are capable to reproduce bulk properties to a reasonable extent. Whereas a deeper look at this study concludes that the RMF shows superiority over the non-relativistic mean field approach. One can also conclude from this analysis that the accuracy of the predicting power of RMF gets enhanced with an increase of mass number of nuclei. The uncertainty in the estimation of results at a light mass range may be associated with its dependency on mass number (error$\sim 1/A$). The effect of BCS pairing is also studied for isotopes of Ne, Mg and Si nuclei.

In **chapter 4**, we have studied the density distributions of $^{9-12}$Be, $^{12-15}$B, $^{13-20}$C, $^{20-23}$N, $^{20-24}$O, $^{23-27}$F, $^{28-32}$Ne, $^{32-35}$Mg, $^{32-35}$Si, $^{34-37}$S and $^{34-48}$Ar isotopes in the frame-work of the non-relativistic Hartree-Fock mean field formalism with SkI4 parameter and the relativistic mean field formalism with NL3 parameter set. in light mass region. The bubble effect for ^{22}O, ^{23}F, ^{34}Si, ^{36}S, ^{36}Ar and ^{46}Ar nuclei in light mass region is studied and the prominent cases showing bubble effects are identified as ^{22}O, ^{23}F, ^{34}Si and ^{46}Ar. Such effect is of huge relevance for studying the nuclear structure in the drip-line and the superheavy region. In general, we observed that both the formalisms are capable of studying the nuclear structure for most of light mass nuclei, with slightly better accuracy for RMF formalism over the non-relativistic HF(SEI-I). Further investigations in medium and heavy mass regions may impart a better description regarding the comparative analysis of these formalisms

In **chapter 5**, we have discussed the reaction cross sections of light mass nuclei using Glauber model with densities from relativistic and non-relativistic mean field formalism. A list of various inputs of the Glauber model are given in this chapter. The major input

of the Glauber model are the densities of the projectile and the target nuclei, which are fed from the microscopic mean field formalisms. These densities are converted in the form of Gaussian coefficients using RMF and HF densities. The sensitivity of converted densities has been checked with the RMF and HF densities in terms of their density profiles. The fittings appear better with 2-Gaussian form for RMF as compared to the 4-Gaussian form, whereas a reverse trend is observed for the non-relativistic mean field densities. The comparative analysis suggests that both the formalisms are competent with a relative edge for RMF densities over non-relativistic mean field formalism. The deformation or deformed structure of nuclei is expected to affect the reaction dynamics, so an effort is made to address such effect in the context of dynamical evolution of the nuclear systems. In general, a comparative study of the reaction cross sections using densities from RMF and non-RMF formalism shows the superiority of RMF over non-relativistic case. The role of deformations is analyzed through deformed densities by carrying out a comparative analysis using spherical densities of same set of nuclei. Structure effect on the reaction cross sections are also analyzed by considering variable target projectile combinations.

In **Chapter 6**, we have estimated the ground state properties and reaction cross sections for some of the halo nuclei ^{6}He, ^{11}Li, ^{11}Be, ^{15}C, ^{19}C, ^{22}C, ^{23}O and ^{31}Ne as projectiles with ^{12}C target by using relativistic and non-relativistic mean field formalisms. The estimated values of binding energy, rms radius, rms charge radius, quadrupole deformation and one/two neutron separation energies from both the formalisms have been compared with the available experimental data. The densities obtained from two completely different sources have been used in the extended Glauber model (GMMB) for an evaluation of σ_R over the energy range. In conclusion, results obtained from both the RMF and Hartree-Fock formalisms are well compared with the experimental data with an edge for the SEI-I interaction. A systematic study of the Glauber formalism has been used for an

investigation of the structure of ^{31}Ne halo candidate. An analysis of the reaction cross section and one neutron removal cross section supports the halo status of ^{31}Ne nucleus. Further, in reference to a newly discovered halo nucleus ^{37}Mg, we have compared the ground state properties of Mg isotopes with RMF formalism and also studied the reaction cross sections of these isotopes taken as projectile from the valley of stability to drip line region with stable ^{12}C target at E_{proj}=240 MeV/nucleon. We observed a nice agreement of ground state properties of Mg-isotopes with the available data. The calculated values of the reaction cross section using RMF densities find a nice agreement with the experimental data. The skin effect variation is studied as a function of the mass number, in order to see the effect of the density profile. A study of an angular elastic differential cross section for $^{34-38}$Mg and further a investigation with Glauber two body calculation also supports the halo status of ^{37}Mg. The halo status of ^{37}Mg also seems justified from its higher magnitude of rms radius ∼6.041 fm, one neutron removal cross section and small value of longitudinal momentum distribution. As the diffuseness parameter gives narrow width in comparison with the available experimental data for this isotope, so further efforts are anticipated to have comprehensive addressal of these issues.

7.1 Future scope of the work

In the present work, systematic study of the nuclear structure has been carried out for light mass nuclei, from the valley of stability to the drip-line by using mean field formalisms (relativistic and non-relativistic), whereas the related reaction dynamics has been explored in the frame work of Glauber formalism. We find that these formalisms provide a very successful tool to investigate the bulk properties and are capable of investigating some emerging phenomena such as bubble effects and halo status of nuclei. In future, an

attempt shall be made to extend our findings to analyze the following points (i) to extend the structure analysis via mean field theories to the medium, heavy and super-heavy mass regions. ii) In present work we have converted the mean field densities to spherical equivalent in terms of the Gaussian coefficients, which may sometimes compromise with an accuracy of results. We intend to modify the used formalism in view of deformed mean filed densities *i.e.* The densities of the mean field formalisms be feeded directly in the calculations instead of using gaussian coefficients. iii) The single particle wave function is used to introduce dynamic approach in two body Glauber model, which may be modified in the context of the mean field criteria. iv) The systematic study of deformation is of extreme interest, as it plays a very important role in the analysis of reaction dynamics. The systematic variation of deformation parameter is beyond the scope of mean field calculations as the deformation parameter arrives self consistently. There is a definite scope of further exploration in this area.